UCRL-19175

c. 2

INITIAL STAGES OF ORDERING IN Ni_4Mo

RECEIVED
LAWRENCE
RADIATION LABORATORY
MAY 20 1970
LIBRARY AND
DOCUMENTS SECTION

Paul R. Okamoto
(Ph.D. Thesis)

March 1970

AEC Contract No. W-7405-eng-48

TWO-WEEK LOAN COPY

This is a Library Circulating Copy which may be borrowed for two weeks. For a personal retention copy, call Tech. Info. Division, Ext. 5545

UCRL-19175

LAWRENCE RADIATION LABORATORY
UNIVERSITY of CALIFORNIA BERKELEY

25

DISCLAIMER

This document was prepared as an account of work sponsored by the United States Government. While this document is believed to contain correct information, neither the United States Government nor any agency thereof, nor the Regents of the University of California, nor any of their employees, makes any warranty, express or implied, or assumes any legal responsibility for the accuracy, completeness, or usefulness of any information, apparatus, product, or process disclosed, or represents that its use would not infringe privately owned rights. Reference herein to any specific commercial product, process, or service by its trade name, trademark, manufacturer, or otherwise, does not necessarily constitute or imply its endorsement, recommendation, or favoring by the United States Government or any agency thereof, or the Regents of the University of California. The views and opinions of authors expressed herein do not necessarily state or reflect those of the United States Government or any agency thereof or the Regents of the University of California.

TABLE OF CONTENTS

ABSTRACT iv

1. INTRODUCTION 1

2. CRYSTALLOGRAPHY OF Ni_4Mo 8

3. EXPERIMENTAL PROCEDURE 16

   3.1 Alloy Preparation 16

   3.2 Heat Treatment 16

   3.3 Specimen Preparation 17

   3.4 Electron Microscope Techniques 18

   3.5 Field Ion Microscopy 19

4. EXPERIMENTAL RESULTS 21

   4.1 Transmission Electron Diffraction and Microscopy. 21

      4.1.1 As-Quenched Alloys 21

      4.1.2 Alloys Aged at 750°C 24

      4.1.3 Alloys Aged at 650°C 26

      4.1.4 Summary of TEM Results 29

   4.2 Field Ion Microscopy 31

      4.2.1 Alloys Aged at 750°C 31

      4.2.2 Alloys Aged at 650°C 34

      4.2.3 As-Quenched Alloys 36

      4.2.4 Fluctuations in Degree of Order of As-Quenched Alloys 37

      4.2.5 Summary of FIM Results 39

The electron diffraction patterns of the as-quenched alloy exhibits both sharp $1\frac{1}{2}0$ SRO spots and very weak satellites near superlattice positions. However, the latter are detectable only in microphotometer traces and then only in diffraction patterns of certain favorable orientations. These satellites were not observed on <002> diffraction patterns as they are obscured by neighboring $1\frac{1}{2}0$ SRO spots. As ordering proceeds, the satellites eventually sharpen into superlattice reflections at the expense of the $1\frac{1}{2}0$ SRO spots. During the very early stages the satellites are streaked in the <210> directions of the fcc lattice; however, satellites which eventually develop into superlattice reflections corresponding to domains of a particular orientational variant are not initially streaked in the same <210> direction.

An explanation for this is given in terms of a composition modulation normal to the {420} planes of the fcc lattice. A diffraction model based on this idea explains not only the $1\frac{1}{2}0$ SRO intensity maxima but also the presence of the weak satellites near superlattice positions. The model is also compatible with the FIM results and suggests that the bright well defined groups of atoms correspond to planes possessing a high Mo concentration. A physical basis for the diffraction

model is given in terms of a recent spinodal approach to order-disorder transformations. The physical connection between the present results and the theoretical prediction of the Clapp-Moss theory of SRO is also discussed.

1. INTRODUCTION

Many stoichiometric solid solutions exhibit long range order (LRO) below a critical temperature and short range order (SRO) above it. The conceptual meaning of LRO and its mathematical definition based on diffraction intensity measurements are well understood. The state of LRO in an alloy can be specified in terms of a system of interpenetrating sublattices and a complete set of occupational parameters describing the distribution of the atomic species on each sublattice. Moreover, all complete sets of LRO parameters are equivalent regardless of how they are defined or obtained. Hence, a state of LRO is uniquely defined.

On the other hand, there is no unique definition of SRO. SRO parameters based on diffraction phenomena are not always equivalent to those obtained by other methods. However, since they have the advantage of being directly related to the conditional pair probabilities used in statistical-thermodynamic theories of solid solution energetics, they are at the present time the most widely employed parameters.

While the conditional pair probabilities obtained from diffraction intensity measurements do describe the state of SRO, they do not provide a clear physical picture in terms of a unique structural model. At the present time one cannot on the basis of diffraction effects alone distinguish

between the following structural models of SRO:

(a) The statistical thermodynamic model which views SRO in terms of a liquid-like arrangement of unlike neighbors around each atom.[1-3] In terms of diffraction effects LRO and SRO are considered as distinct phenomena. During the transition to the ordered state the gradual sharpening of diffuse SRO maxima into superlattice reflections is viewed as a competitive process between SRO and LRO in which superlattice reflections appear superimposed on the diffuse SRO maxima.

(b) The microdomain model which views SRO in terms of a continguous distribution of tiny, highly ordered ~~antiphase~~ domains.[4-7] A somewhat different version of this view known as the discrete particle model considers SRO as consisting of a very high density of tiny, highly ordered regions ~~anti-phase to each other~~ embedded in a nearly random matrix. In terms of diffraction effects the two are similar in that both consider the diffuse SRO maxima as a broad superlattice reflection, the broadening being essentially a small particle effect. As the domain or particles grow in size the SRO maxima peaks up into a superlattice reflection.

The distinction between the two viewpoints is of critical importance since they lead to quite different predictions for the mechanism of the transformation itself. On the one hand, the microdomain concept implies that the transition

from SRO to the LRO state occurs by a single continuous process, namely domain growth; no distinct nucleation step appears necessary. On the other hand, the statistical-thermodynamic concept appears to require some form of a beginning in the transition to the ordered state. A distinction between the two viewpoints would also be of major importance in any attempt at correlating SRO with physical and mechanical properties.

The strongest experimental evidence in favor of the microdomain concept or its discrete particle version has been provided by electron rather than x-ray diffraction studies. In the case of disordered Cu_3Au, several investigators using electron diffraction[8,9] have observed diffuse satellite crosses about the positions of the superlattice reflections. Such observations can only be explained in terms of a distribution of antiphase domains. Moreover, the direct observation of an irregular antiphase domain structure in transmission electron dark field images in partially ordered Cu_3Au provide additional support.[10] The diffuse satellite crosses in disordered Cu_3Au have not yet been clearly resolved using x-ray diffraction techniques. The discrepancy can be explained if one admits the possibility of local fluctuations in the degree of SRO or LRO. X-rays which scatter over a much larger volume of sample would tend to average out the presence of large fluctuations.

The diffuse satellites reported by electron diffractionists could then be representative of regions where the degree of order happened to be very high.

Since the early work on Cu_3Au, considerable evidence has been accumulated in favor of the microdomain model, in particular for its discrete particle version in many alloy systems other than Cu_3Au. However, much of the evidence is still of an indirect nature based on diffraction effects or by coherency strain contrast images in transmission electron micrographs.[11-13, 36,37] Direct observation of a fine scale domain structure has not yet been observed in disordered alloys and only very rarely in alloys in the very initial stages of ordering. The only major exception to this has been the field ion microscope studies of Pt-Co alloys[14] in which the disordered state was found to consist of tiny, highly ordered domains embedded in a random matrix.

In this respect, the optical diffraction experiments of Taylor, et al.,[15] and more recently the computer simulation experiments of Gehlen and Cohen[16] are of some significance. Taylor studied the optical diffraction patterns from masks in which gold and copper atoms were represented by holes of different sizes. Initially the holes were distributed at random corresponding to (100) planes of disordered Cu_3Au. Order was then introduced in stages by interchanging pairs

of holes equivalent to reducing the number of gold atoms in contact. The resulting optical diffuse scattering pattern was very similar to x-ray results of Cowley[17] for Cu_3Au above the critical temperature. The final arrangement of the holes corresponded to a very high density of antiphase domains embedded in a random matrix.

Similar results were obtained by the recent computer simulation experiments of Gehlen and Cohen. In this type of experiment a three dimensional crystal of disordered Cu_3Au is simulated in a computer. The interchange between pairs of sites is guided by comparing calculated SRO parameters with those determined by experiments. The interchanging procedure is allowed to continue until the two agree. The computer print out of the final atomic arrangement shows very tiny, highly ordered regions in a nearly random matrix. The ordered regions are plate-like in shape lying on (100) planes with the smallest having dimensions of a single unit cell.

In spite of what may appear as overwhelming experimental and theoretical support for the microdomain model or for its discrete particle version, it possesses a major weakness. Since it interprets the diffuse SRO maxima as a broad superlattice reflection, their positions in reciprocal space should always coincide. This is actually observed in

diffraction patterns of the more common ordering systems examined in the past, but there are a number of others in which coincidence is not observed.

This anomaly cannot be explained by the microdomain model. It is however compatible with a recent statistical-thermodynamic theory of SRO developed by Clapp and Moss.[18-20] In fact, their theory predicts that certain alloy systems which have an fcc structure in the disordered state should exhibit SRO maxima only at the peculiar ($1\frac{1}{2}0$) positions in the fcc reciprocal space. This prediction has now been well documented experimentally in several alloy systems: Ni_4Mo,[21] Au_3Cr,[22] and Ni_4W.[23] All these alloys have the fcc structure in the disordered state and the $D1_a$ bct structure when ordered. It has therefore been claimed that the microdomain concept is not valid at least for these systems.[20,22]

However, Spruiell and Stansbury[21] have concluded that the results of their diffuse x-ray scattering of disordered Ni_4Mo favor the microdomain model. Moreover, Ruedl, et al.,[24] have recently reported direct transmission electron microscopy evidence of a domain structure in disordered Ni_4Mo, with a domain size on the order of 10Å. On the other hand, LeFevre, et al.,[25,26] were unable to obtain evidence for such domains in their field ion images of disordered Ni_4Mo. They therefore concluded that SRO in the alloy is best described by the statistical-thermodynamic model.

In view of the present controversy surrounding Ni_4Mo and its potential role as a deciding factor between the two opposing views of SRO, it was considered worthwhile to re-examine the disordered alloy and to follow the changes which occur during the very initial stages of ordering using both transmission electron microscopy (TEM) and field ion microscopy (FIM) techniques.

The ordered structure of Ni_4Mo is rather complex and there are several crystallographic features which are of critical importance in interpreting field ion images and electron diffraction patterns. Since some of the more critical experiments were planned with these features in mind the next section will describe in detail the structure of Ni_4Mo.

2. CRYSTALLOGRAPHY OF Ni_4Mo

The phase diagram of the Ni rich portion of the Ni-Mo system is shown in Fig. 1. The Ni_4Mo ordered phase β, does not have a true ordering temperature. Guthrie and Stansbury[27] have shown that a peritectoid reaction occurs before the critical temperature is reached involving the ordered β phase, the disordered α phase and the ordered γ phase. Upon slow cooling from the α phase the alloy with the composition Ni_4Mo passes through the $\alpha + \gamma$ region prior to transforming into the β phase. At the peritectoid temperature (865°C) the α and β phases have almost identical composition and the $\alpha + \gamma$ range is very narrow. The result is that the $\alpha \rightarrow \beta$ transformation occurs on slow cooling as though it were a classical order-disorder transformation. However, upon fast quenching the α phase is retained and on isothermal aging below the critical ordering temperature (860°C), the α phase transforms directly to the ordered β phase.

The lattice parameter of the disordered fcc (α phase) at the composition Ni 20 at %Mo is $a_{fcc} = 3.6086$Å. Upon ordering, a slight contraction occurs along one of the original <100> cube axis so the original fcc lattice becomes fct with $(c/a)_{fct} = 0.986$. The Bravais lattice changes from fcc to body-centered tetragonal (bct). A plan view of the

Ni_4Mo structure is shown in Figs. 2a and 2b. The most salient features of the structure can be summarized as follows:

(a) The bct unit cell contains 8 Ni and 2 Mo atoms. The structure may be viewed as a single bct lattice with 1 Mo and 4 Ni atoms per Bravais lattice point or in terms of 5 interpenetrating bct sublattices one with a single Mo atom per lattice point, the other 4 with a single Ni atom per lattice point.

(b) The c-axis of the bct unit coincides with one of the <100> cube axes of the fcc unit cell.

(c) For a given choice of c-axis, the Ni and Mo atoms can be arranged in two ways resulting in the bct unit cell rotated in either a clockwise (Fig. 2b) or a counter-clockwise (Fig. 2a) sense with respect to the fcc unit cell. Henceforth these two ordering schemes will be referred to as Type II and Type I, respectively.

(d) All superlattice planes are layered with every fifth plane containing only Mo atoms, the intervening 4 containing only Ni atoms. The most prominent superlattice planes, i. e., those of highest symmetry and largest d-spacing are the $(110)_{bct}$ and $(\bar{1}10)_{bct}$. In the Type I structure $(110)_{bct} \parallel (4\bar{2}0)_{fcc}$ and $(\bar{1}10)_{bct} \parallel (240)_{fcc}$. In the Type II structure $(110)_{bct} \parallel (420)_{fcc}$ and $(\bar{1}10)_{bct} \parallel (2\bar{4}0)_{fcc}$.

It is readily apparent from Figs. 2a and 2b, that the ordered Ni_4Mo phase can "nucleate" in 30 crystallographically equivalent ways giving rise to domains possessing 6 distinct orientation variants with respect to the parent fcc phase. The c-axis can align itself with any one of the 3 original ⟨100⟩ cube axes. For a given choice of c-axis we can have either a Type I or Type II structure. For each of the 6 orientation variants the Mo atoms can choose to occupy any one of 5 sublattices. The 6 orientational variants may be regarded as "transformation twins". The symmetry planes relating the twins are of the $\{110\}_{fcc}$ family.

The superposition of the reciprocal lattices of all 6 twins results in superlattice reflections arranged symmetrically in groups of 4 about all equivalent $1\frac{1}{2}0$ positions in the fcc reciprocal lattice (See Fig. 3). The $(002)^*_{fcc}$ $(121)^*_{fcc}$ sections of the fcc reciprocal lattice are shown in Figs. 4a and 4b, respectively. The structure factor for the fundamental and superlattice reflections are given by:

$$F_f^{D1a} = 2(f_{Mo} + 4f_{Ni}) \quad \begin{cases} \text{for } H + K + L = 2n \ (n = 0,1,2....) \\ \text{and } 2H + K = 5n \end{cases}$$

$$F_s^{D1a} = 2S(f_{Mo} - f_{Ni}) \quad \begin{cases} \text{for } H + K + L = 2n \ (n = 0,1,2....) \\ \text{and } 2H + K \neq 5n \end{cases}$$

where S is the Bragg-Williams LRO parameter and H, K and L refer to the bct unit cell. If h, k and l refer to the fcc

unit cell then for the Type I structure $h = \frac{1}{5}(3H - K)$, $k = \frac{1}{5}(H + 3K)$ and $l = L$.

Because the principal axis of the ordered and disordered phases are not aligned, the essential crystallographic features have been described in terms of the bct structure. For later purposes it will be more convenient to discuss structural features using the fcc lattice as the frame of reference.

The metastable domain structure consists of an assembly of domains or transformation twins having any one of 6 orientational variants. The symmetry planes relating to the transformation twins are of the form $\{110\}_{fcc}$. These twins may also be viewed as domains in which layering occurs along particular pairs of $\{4\bar{2}0\}_{fcc}$ type planes. Our particular frame of reference will be the Type I structure shown in Fig. 2a in which case the c-axis coincides with the z-axis of the fcc lattice.

Referring again to Fig. 2a, it is readily apparent that the Type I structure can be generated by periodic composition fluctuations normal to the $(240)_{fcc}$ or $(4\bar{2}0)_{fcc}$ planes in which every fifth plane contains only Mo atoms, the other 4 only Ni atoms. Now suppose within some small spherical region the composition fluctuations happened to be normal to the $(420)_{fcc}$ or $(2\bar{4}0)_{fcc}$. As shown in Fig. 5, the resulting

domain is equivalent to a Type II structure. In this case the two domains are simply mirror images across either the $(110)_{fcc}$ or $(\bar{1}10)_{fcc}$ planes. The orientational relationship between the principal axes of the matrix (Type I structure) and twin crystals are:

For Twinning on $(110)_{fcc}$	For Twinning on $(\bar{1}10)_{fcc}$
[100] twin ∥ [010] matrix	[100] twin ∥ $[0\bar{1}0]$ matrix
[010] twin ∥ [100] matrix	[010] twin ∥ $[\bar{1}00]$ matrix
[001] twin ∥ $[00\bar{1}]$ matrix	[001] twin ∥ $[00\bar{1}]$ matrix
$[4\bar{2}0]$ twin ∥ $[\bar{2}\bar{4}0]$ matrix	$[4\bar{2}0]$ twin ∥ $[\bar{2}\bar{4}0]$ matrix
[240] twin ∥ [420] matrix	[240] twin ∥ $[\bar{4}\bar{2}0]$ matrix

Therefore, the formation of a small spherical domain by chance fluctuations within the matrix can also be regarded as equivalent to a twinning process. For this particular case the two domains are in antiparallel twin orientation since their c-axes, though aligned along the reference z-axes, are pointing in opposite directions. It should also be noticed that, although the twin is a Type II structure with respect to the reference fcc lattice, relative to its own principal axes it will regard itself as a Type I structure. This is because although the composition fluctuation within the twin is normal to the (420) and $(\bar{2}40)$ matrix planes, relative to its own principal axes the fluctuations will be normal to the $(\bar{4}20)$ and (240) planes which by definition generates a Type I structure.

Similar fluctuations along appropriate matrix directions of the form $\langle 4\bar{2}0 \rangle$ will generate other domains or twins in which the twin c-axis is at 90° with respect to that of the matrix. The c-axes of the matrix and twin can meet head-to-head or head-to-tail depending on whether the twin regards itself as having Type I or II structures. For each domain this will depend on whether, relative to its own principal axes, the fluctuations occur normal to the $\{(4\bar{2}0),(240)\}_{twin}$ or $\{(420),(2\bar{4}0)\}_{twin}$ pairs of planes. Stated somewhat differently, ordered domains with the proper twin orientation relative to the matrix will have one of their 4 special planes lying parallel to one of the 12 matrix planes of the form $\{4\bar{2}0\}$.

These special pairs of planes will have particular significance in the analysis of FIM images. The physical significance of the planes is that they are parallel to the (110) and $(\bar{1}10)$ planes in the ordered bct structure. These are the superlattice planes with highest symmetry and largest d spacing. Moore and Ranganathan[28] have shown that the size and hence the prominence of a pole in a field ion image decreases with decreasing d spacing. Therefore, the (110) and $(\bar{1}10)$ bct superlattice planes will be the most prominent in FIM images of Ni_4Mo. This is readily apparent in the FIM images of Ni_4Mo reported by LeFevre.[29] However, these were

images essentially of single domains and hence readily indexed. In the case of a domain structure consisting of a random distribution of very tiny domains or transformation twins, the domains may be too small to be recognized as such.

The ability to identify domains on the order of 10Å is the critical problem for the present study. Since only the Mo atoms give rise to image points[30,31] the best chance to obtain evidence of domains is therefore to look for planes on which Mo atoms are most densely packed. For a particular domain, these planes are the special pairs $\{(4\bar{2}0), (240)\}$ and $\{(420), (2\bar{4}0)\}$. Moreover, we should focus our attention to those regions on the specimen tip where these planes will lie parallel to the surface. The preceding description of the domain structure in terms of composition fluctuations indicates that such regions will lie about the poles of the form <420> of the matrix. However, a domain lying in one of these regions will have only one chance in three of having the proper orientation for observing one of its 4 special planes.

Therefore, if tiny domains are present, then by focusing our attention to the <420> type poles we should while field evaporating, periodically observe tiny, well defined planes corresponding to one of the four special types. Of course, since there are other superlattice planes which are also

layered, well defined planes can also be expected in regions other than around the <420> matrix poles. However, these regions can also be predicted by an analysis similar to the one above. However, the overall effect should be strongest around the <420> matrix poles.

It is possible that well developed groups of atoms would be observed even if a domain structure were absent. However, in this case we would not expect their distribution to have any strong orientation dependence.

3. EXPERIMENTAL PROCEDURE

3.1 Alloy Preparation

Alloys of nominal composition Ni 29.1 wt% Mo (20 at% Mo) were prepared from 99.9% Ni and 99.9% Mo by arc melting in argon. In order to obtain a dense, gas-free alloy, the ingot was swaged into rod form then remelted four times in an electron beam zone refining furnace. The rod was inverted between each pass to ensure uniform mixing of the constituents. The final homogenization treatment consisted of holding in vacuum for an additional 90 hours at 1250°C. The composition of the homogenized rod was determined by wet chemical analysis to be Ni 29.3 wt% Mo (20.2 at% Mo). Sheets .005 in. thick were produced by cold-rolling the rods at room temperature using intermediate anneals at 1100°C.

3.2 Heat Treatment

Samples with dimensions 0.25 x 0.005 x 1.0 in. were sealed in evacuated quartz tubes and placed in a vertical tube furnace for 3 hours at 1100°C. Quenching was performed by releasing the quartz tube into iced brine.

Isothermal aging treatments were performed in a salt bath solution of $BaCl_2$, NaCl and $CaCl_2$. Heating rates were measured using .005 in. diam. Pt-10% Rh thermocouples spot welded to the sample with the output connected either to an

oscilloscope or a Honeywell Electronik 19 strip recorder. The minimum aging time used for any heat treatment was arbitrarily chosen to be twice the time required for the sample temperature to reach equilibrium. For example, for 650°C and 750°C the average time to reach equilibrium was 2 and 5 seconds, respectively. Hence for these aging treatments the shortest aging times involved were 4 and 10 seconds, respectively.

For aging times less than one minute, the maximum temperature fluctuation of the sample was ±5°C. For longer times, the fluctuations were generally maintained below ±2°C. The quenching rates during the transfer from the salt bath to an iced brine solution was also monitored and the time to reach zero output on the strip recorder was kept consistently below one second.

3.3 Specimen Preparation

Specimens for both TEM and FIM were prepared from the same heat treated sample. FIM specimens were prepared by cutting 10 to 15 strips 1 inch long and approximately .005 inch wide from each sample using a specially designed precision shearing device. In order to check whether spurious effects were introduced by the shearing process several strips were precut from an as-quenched sample. These together with another as-quenched sample were sealed

in quartz tubes and aged for 125 hours at 750°C to develop the fully ordered state. FIM images from the precut strips and those cut from the sample after aging were identical in that neither revealed any evidence of disorder. Any deformation which may have occurred during the shearing process was therefore confined to the surface and subsequently removed during electropolishing.

Thin foils suitable for TEM were prepared by electropolishing using standard window techniques. FIM tips were prepared by the double layer method in which the specimen is dipped into a thin layer of electrolyte floating on top of a bath of carbon tetrachloride. The same electrolyte was used for both techniques. The composition of the electrolyte as well as the polishing conditions are listed in Table I.

3.4 Electron Microscope Techniques

A Siemens 1A electron microscope operated at 100kv was used to make all TEM observations. Tilting and contrast experiments were performed with the aid of a Valdre type double tilting stage. Magnifications were calibrated by taking a series of micrographs of a calibrated replica grid at various settings of the objective lens. Errors in magnification were minimized by taking all micrographs at the same intermediate and projector lens settings and using the same specimen holder throughout the study.

3.5 Field Ion Microscopy

The principles and techniques of field ion microscopy have been extensively reviewed by Muller[32] and more recently by Hren and Ranganathan.[33] For the purpose of the present study it will suffice to point out that very little progress has been made in interpreting FIM images from disordered concentrated solid solutions. The difficulty is mainly due to the inability to distinguish between different atoms and hence their distribution in the highly irregular images that are obtained. However, such detailed information is not necessary for the purpose of the present study which is to seek evidence of ordered domains. Such evidence will be based mainly on observation of macroscopic features such as domain boundaries or clustering of well defined planes whose distribution and frequency of appearance have a particular orientational dependence. Confidence in the interpretation of such effects in disordered alloys will be based heavily on correlating FIM and TEM observations at various advanced stages of ordering where the structural features are within the resolution capabilities of the transmission electron microscope.

The basic field ion microscope used in this study was originally designed by P. Petroff.[34] Several modifications were made during the course of this study. The major changes

were: (a) the construction of a new variable temperature cryotip designed to operate with liquid helium or cooled helium gas. Temperature control was obtained by varying the rate of transfer of cooled helium gas. The minimum temperature obtainable being approximately 15°K; (b) the construction of a multiple high tension feed-through which enabled more than one specimen to be viewed during each experimental run; and (c) the construction of a stainless steel viewing port utilizing a 4½ inch diameter fiber optic plate for the output screen. This allowed FIM images to be obtained by direct contact photographic recording on 4 x 5 sheet film.

TABLE I

Electrolytic Solution for Ni_4Mo	
Perchloric Acid	16cc
Ethyl Glycol	132cc
Hydrofluoric Acid	16cc
Distilled Water	9cc
Polishing Conditions	
Temperature:	$-15^{\circ}C$
Voltage:	11 volts

4. EXPERIMENTAL RESULTS

4.1 Transmission Electron Diffraction and Microscopy

The preliminary aspects of the TEM portion of this study were concerned with establishing an overall view of the kinetics of the ordering reaction over a range of temperatures. The aging temperatures finally chosen for detailed study were 650°C and 750°C. The former was used by Spruiell and Stansbury[21] in their diffuse x-ray scattering studies of SRO in Ni_4Mo and the latter by LeFevre and Newman[26] in their FIM study of Ni_4Mo.

4.1.1 As-Quenched Alloys

Fig. 6a is the $[002]_{fcc}$ diffraction pattern obtained from an alloy which had been held at 1100°C for 3 hours prior to quenching into iced brine. In agreement with the x-ray results of Spruiell and Stansbury, SRO maxima are observed at all equivalent $1\frac{1}{2}0$ positions of the fcc reciprocal lattice. The asymmetry in the intensity distribution of the {200} fundamental reflections is also in agreement with their x-ray work. They attribute the higher intensity on the low angle side of the {200} reflections to a size effect, in this case indicating that Mo atoms have a larger diameter in solution than Ni atoms. Fig. 6a is also similar to the <002> electron diffraction patterns of Au_3Cr

reported by Tanner.[22] However, their patterns were obtained at 800°C almost 500°C above the critical ordering temperature for Au_3Cr, so that the $1\frac{1}{2}0$ SRO maxima were quite broad compared to those in Fig. 6a.

Fig. 6b is the $[121]_{fcc}$ diffraction pattern of the same alloy. Again SRO maxima are observed at $1\frac{1}{2}0$ positions. However, it also exhibits a quite unexpected feature of the presence of very weak intensity maxima near but not exactly at the equilibrium angular positions corresponding to superlattice reflections of the fully ordered Ni_4Mo. These intensity maxima are not directly observable on the fluorescent screen in the microscope viewing chamber. In fact, they are generally not discernible even on the original photographic plates and were discovered accidentally on microphotometer traces during attempts to measure the intensities of the SRO maxima.

In due course it was found that the optimum conditions for observing these weak maxima were to defocus the second condenser lens to the point where the diffraction pattern was just barely visible and then exposing for times between 1 and 2 minutes. Fig. 6b is a reproduction of the best of many original photographic plates obtained during this study. The microphotometer tracing obtained from the original plate is shown in Fig. 7. The weak intensity maxima near the

$2\bar{2}0$ and $3\bar{3}0$ bct superlattice positions are clearly detectable while those near the $1\bar{1}0$ and $4\bar{4}0$ positions are all but obscured by the neighboring $1\frac{1}{2}0$ SRO intensity peak. These weak intensity maxima were not observed on the <002> diffraction patterns. This is not surprising however, since in this particular orientation they would all lie very close to and hence obscured by one of the $1\frac{1}{2}0$ SRO maxima. As indicated in Fig. 7, the weak maxima are readily detectable only when their neighboring SRO maxima does not lie on the reflecting sphere. This will occur only for certain favorable orientations and the most favorable of all would be one where only superlattice reflections lie on the reflecting sphere. Fig. 4c shows that the $(\bar{1}30)^*_{fcc}$ is one of these and the actual $[\bar{1}30]_{fcc}$ diffraction pattern (Fig. 6c) shows quite clearly weak intensity maxima near all superlattice positions.

To the author's knowledge, the existence of weak intensity maxima near superlattice reflections in as-quenched Ni_4Mo has not been previously reported. This is obviously due in part to the weakness of these particular maxima but more likely due to the fact that past diffuse scattering studies for this alloy have been confined almost exclusively to the $(002)^*_{fcc}$ reciprocal lattice section. As just pointed out, this particular orientation is the least convenient one

of all for such purposes. The existence of weak intensity near superlattice positions is quite significant since their apparent absence in past studies have been one of the reasons for arguing against the microdomain model of SRO. The present observations however show that some form of domain structure exists in the as-quenched alloys.

This would appear to be in agreement with the conclusions of Ruedl[24] who, though apparently missed detecting these weak maxima, did report observing a fine "domain" structure in dark field images of $1\frac{1}{2}0$ SRO reflections. We were therefore surprised when after many repeated attempts we were unable to confirm his results. Figs. 8a and 8b are bright and dark field images obtained from a $[121]_{fcc}$ foil. The dark field image obtained with a $1\frac{1}{2}0$ SRO reflection does not reveal the sharp dotted structure reported by Ruedl. Moreover, the images remain unchanged if one uses the weak intensity maxima near the $(2\bar{2}0)$ bct superlattice position.

4.1.2 <u>Alloys Aged at 750°C</u>

The ordering reaction at 750°C is extremely fast. Alloys aged at this temperature reach a fairly advanced stage of order by at least 5 seconds, the shortest aging time used for this series of experiments. As shown in Fig. 9a, well defined superlattice reflections are observed though slightly elongated in $\langle 210 \rangle_{fcc}$ directions. Also,

relatively weak intensity peaks are still observed near the $1\frac{1}{2}0$ positions. The diffraction pattern is a composite of diffraction patterns from domains possessing two of the six possible orientational variants. In this case, the two domains have c-axes which are at 90° to one another. Fig. 9b is a dark field image showing one of the two sets of twins.

Figs. 9c-9f are bright field images using various fundamental reflections from a $[110]_{fcc}$ foil. The striated structure is similar to the type of diffraction contrast characteristic of alloys containing a large volume fraction of coherent precipitates.[35,36,37] Similar striations have recently been observed during the very early stages of decomposition in Cu-Ni-Fe alloys.[38,39] In the case of Ni_4Mo the number and direction of the striae depend on the operating reflection in a manner similar to those observed during the initial stages of decomposition in Cu-Be.[40] After 10 seconds of aging the diffraction pattern shown in Fig. 10a exhibits weak double diffraction spots arising from twin boundaries between domains. Hence, at this stage of the ordering reaction the domains are already touching. At more advanced stages of order where the domains are sufficiently large, the double diffraction spots can be used quite effectively to image the twin boundaries themselves.

Further isothermal treatment (Fig. 11) results in a uniform mosaic substructure comprised of prism-shaped 90°

domains bounded by interfaces lying parallel to matrix planes of the form $\{110\}_{fcc}$. Each of these 90° twins are themselves comprised of antiparallel twins. In turn, the latter exhibits translational antiphase boundaries. Hence, the domain structure consists of an assembly of transformation twins as described in Section 2. The dark field images b, c and d were obtained using superlattice reflections 2, 3 and 4 in Figs. 3 and 4.

4.1.3 Alloys Aged at $650^{\circ}C$

Upon aging at $650^{\circ}C$ the weak intensity maxima gradually sharpen and "move" into the equilibrium angular positions for the Ni_4Mo superlattice positions. Simultaneously the $1\frac{1}{2}0$ SRO spots weaken and eventually disappear, resulting after long aging times in diffraction patterns similar to Figs. 9a and 10a. The most unusual and interesting changes in diffraction effects however occurred during the first 10 minutes of aging. These changes are shown in Figs. 12a-12d.

After 5 minutes of aging the weak intensity maxima near the superlattice reflections are clearly detectable without the aid of a microphotometer. They appear in Fig. 12b as diffuse satellites about the $1\frac{1}{2}0$ position in an $[002]_{fcc}$ diffraction pattern and are streaked in directions parallel to $\langle 420 \rangle_{fcc}$ directions. In $[121]_{fcc}$ patterns (Fig. 12a) the satellites near a $1\frac{1}{2}0$ SRO maxima are broader and more

intense than those away from such position. The effect is even more pronounced after 10 minutes of aging (Fig. 12c). This asymmetry is not observed in $\langle 002 \rangle_{fcc}$ diffraction patterns. This rather unusual intensity distribution can be explained if the set of satellites about a $1\frac{1}{2}0$ SRO maxima have a paddle-like shape shown in Fig. 13. Each broad flat face is normal to a $\langle 002 \rangle_{fcc}$ direction and these are the sections observed in $\langle 002 \rangle_{fcc}$ diffraction patterns. Referring again to Fig. 3, it is apparent that in a $[121]_{fcc}$ orientation, the reflecting sphere will cut through the satellite at the sections A and B. Section A corresponds to satellites near $1\bar{1}0$ and $3\bar{3}0$ bct superlattice positions, i.e., to those which appear to emanate from a $1\frac{1}{2}0$ SRO spot. Section B corresponds to satellites near $2\bar{2}0$ and $4\bar{4}0$ bct positions whose neighboring $1\frac{1}{2}0$ spot lies off the reflecting sphere.

The elongation of the satellites in the $\langle 210 \rangle_{fcc}$ directions indicate ordered domains may have a plate or disc-like shape lying on $\{420\}_{fcc}$ planes. This would be compatible with the layered structure of the fully ordered Ni_4Mo structure discussed in Section 2. There we showed that ordered domains with the proper twin orientation relative to the matrix will have one of four special planes corresponding to the most prominent bct superlattice planes,

lying parallel to one of the 12 matrix planes of the form $\{4\bar{2}0\}_{fcc}$. This type of plate-like morphology has in fact been reported in Co-Pt[13] and Cu-Au[11] alloys at the 50-50 composition. In these alloys superlattice planes are also layered in which alternating planes contain atoms of one type only. The most prominent superlattice plane is the (002); this is also the observed habit planes for the plate-shaped domains.

However, the diffraction patterns of Ni_4Mo exhibit certain distinctive features during this stage of ordering which are not compatible with a simple plate-like morphology. The patterns show a definite asymmetry in that reflections which would normally arise from domains of a particular orientational variant are not elongated in the same $\langle 420 \rangle_{fcc}$ directions. This is most pronounced in [002] diffraction patterns. A discussion of this observation however will be postponed until Section 5. where its full implication will be explored in detail.

At the present time it will suffice to mention that evidence for plate-like domains cannot be obtained by direct observation in dark field images using either the $1\frac{1}{2}0$ SRO spots or its satellites. Fig. 14c is a dark field image using a fundamental reflection of an alloy aged 10 minutes. It exhibits the same type of striated structure observed at

higher aging temperatures. A dark field image using a $1\frac{1}{2}0$ SRO spot (Fig. 14d) reveals a fine dotted structure very similar to those reported by Ruedl. Fig. 12c shows that the satellites overlap at the $1\frac{1}{2}0$ positions, hence, those near the $1\bar{1}0$ bct superlattice positions contribute strongly to the diffraction contrast shown in Fig. 14d. In fact, the image remains essentially unchanged when isolated satellites near the $2\bar{2}0$ bct positions are used. From such micrographs alone it is not possible to determine the shape of the domain.

The situation is worse for shorter aging times. In fact, after 5 minutes of aging the domains are not directly observable in dark field images using either $1\frac{1}{2}0$ SRO spots or any of its satellites (Fig. 14b). However, the striated structure though comparatively weak is still observed especially near bend contours (Fig. 14a).

4.1.4 Summary of TEM Results

(a) The most significant result of this portion of the study is the detection of very weak diffuse satellites in as-quenched alloys near the superlattice positions of the Ni_4Mo structure. This alone is very strong evidence that some form of domain structure exists in the disordered alloy. These satellites are observable only in certain favorable orientations. The least favorable of all is the (002) which

explains why the satellites might not have been observed in earlier studies.

(b) At 750°C the ordering reaction is essentially complete within 5 to 10 seconds of aging. Dark field images using superlattice reflections reveal a very high density of tiny ordered domains. By 10 seconds double diffraction spots appear in all diffraction patterns indicating that at this stage of ordering the domains are in contact.

(c) At 650°C the growth of satellites into superlattice reflections occurs at the expense of the $1\frac{1}{2}0$ SRO spots. During the very early stages there is an asymmetry in the direction of streaking which is incompatible with a simple shape-transform effect of plate-shaped domains.

(d) In as-quenched alloys or in alloys aged 5 minutes at 650°C, tiny, highly ordered domains were not directly resolved in dark field images using a $1\frac{1}{2}0$ SRO spot or any of its satellites. A very high density of tiny bright dots were observed however in alloys aged for 10 minutes at 650°C. These dark field images are very similar in appearance to the "domains" reported by Ruedl in his as-quenched alloy.

4.2 Field Ion Microscopy

Since at 750°C the ordering reaction was essentially complete within 5 to 10 seconds, the critical stages in the transition from the disordered to the ordered state could not be studied. The samples studied by TEM were therefore used primarily for the purpose of correlating FIM images with TEM micrographs. The correlation was then used as the basis for interpreting FIM images during the critical stages of the 650°C aging treatment and those obtained from as-quenched alloys.

4.2.1 Alloys Aged at 750°C

Fig. 15 is an (002) stereographic projection showing the symmetry of a Type I bct structure and its orientation relative to the reference fcc lattice. The crosses are the locations of the fcc poles of the form <420>.

For reference purposes, an FIM image of a fully ordered alloy is shown in Fig. 16. The image consists essentially of a single domain. As discussed in Section 2, the most prominent plane in the image is the $(1\bar{1}0)_{bct}$ or $(4\bar{2}0)_{fcc}$. The second most prominent planes are the $\{10\bar{1}\}_{bct}$ and $\{011\}_{bct}$ which are located near the other <204> matrix poles.

In Section 2 we showed that if tiny domains are present, then by focusing attention on one of the <420> type matrix poles we should during a field evaporation sequence,

periodically observe well defined planes corresponding to one of the 4 most prominent superlattice planes: ($4\bar{2}0$ or 240) for a Type I structure or a (420 or $2\bar{4}0$) for a Type II structure. This was readily verified in all alloys aged at 750°C.

Figs. 17a-17d were obtained during a field evaporation sequence of an alloy aged 1 hour. (The specimen was prepared from the same sample as that shown in Fig. 11). Between Figs. 17a and 17c, some 67 (002) planes have been removed. Initially (Fig. 17a) no prominent plane is visible in the vicinity of the [204] pole lying in the $1\bar{1}1$-002-111 triangle. Upon field evaporating two domains emerge with large prominent planes whose rings are centered on the [204] pole (Fig. 17b). Finally, after further field evaporation only one of the domains remain and as shown in Fig. 17c, its prominent plane is being intersected by a translational antiphase boundary. During the total field evaporation sequence, in which some 300 (002) planes were removed, many prominent planes were also observed to appear and disappear near other <420> matrix poles. The domain boundaries themselves can be brought out with striking clarity by multiple exposing while slowly field evaporating 3 to 5 surface layers, (Fig. 17d). By use of these two imaging techniques during field evaporation sequences, it was found that domains have

very irregular shapes and that domains having the same orientation relative to the matrix tend to cluster in groups of two or three. This, however, is not surprising since Fig. 11 shows that at this stage of ordering the substructure consists of an assembly of 90° twins. Each twin in turn is comprised of a cluster of antiparallel twins and it is these which are being observed in the FIM image.

The same procedure was used to examine alloys aged for 10 seconds at 750°C. At this earlier stage of ordering the bct symmetry is totally disrupted by the tiny domains. The overall symmetry of the FIM image is fcc. However, as shown in Fig. 18, there is still a strong tendency for the most prominent plane to occur in the immediate vicinity of the <420> matrix poles.

The results of the present study of alloys aged at 750°C is not in agreement with the FIM results of LeFevre and Newman.[26] These workers concluded that alloys aged at 750°C remain disordered up to at least 5 minutes and that ordering is essentially complete only after 15 minutes. Our own results show that ordering is essentially complete within 5 to 10 seconds of aging. This is surprising since their FIM images of as-quenched alloys are very similar to our own. This discrepancy could arise for a number of different reasons. First of all, different quenching temperatures were

used and hence, the initial quenched-in degree of order could have been different. However, we do not believe that this is the major reason for the discrepancy since as pointed out earlier, the FIM images of their as-quenched alloy are very similar to our own.

We believe that the major source of the discrepancy lies in the method of aging. During the aging treatment, LeFevre's FIM specimens were wrapped in Ta foils and encapsulated in quartz tubings. In the present study specimens were placed in direct contact with the aging bath. Having tried both methods during the early phase of this study, we found that the heating rate was much faster with the salt bath method and was therefore the one finally chosen for this study.

4.2.2 Alloys Aged at 650°C

FIM images of alloys aged 10 minutes or less showed only fcc symmetry. The most prominent planes are the {111} and {200}. Figs. 19a-19c are typical examples of the microstructure of alloys aged for 10 and 5 minutes. After 10 minutes of aging the tendency for clustering of well defined planes about the <420> matrix poles is readily apparent (Fig. 19a).

Although individual domains in alloys aged only 5 minutes were not resolved in electron micrographs (Fig. 14b), the strong clustering tendency of bright, well defined planes

or groups of atoms about the <420> matrix poles (Figs. 19b and 19c) is direct evidence of domains or ordered particles having the unique distribution described in Section 2. In Figs. 19b and 19c, the local tip radius r, as determined by ring counts between the $(00\bar{2})$ and {024} poles is about 920Å. The diameter of the first (002) ring can then be estimated from the equation $D_{hkl} \sim \sqrt{8rd_{hkl}}$.[28] For r = 920Å, $D_{002} \sim 100$Å. Using this value as a standard of reference, the "diameter" of any well defined plane occurring in the region of the [204], $[02\bar{4}]$, [024] and $[\bar{2}04]$ poles can be estimated. For example, the well defined plane at the $[02\bar{4}]$ pole in Fig. 19b is about 30Å. From 50 such measurements the "diameter" was found to vary from a minimum of about 15Å to a maximum of 115Å with a mean lying around 20Å. No great faith, however, is placed in this mean value since it depended strongly on what one considers as a well defined plane.

The thickness of the well defined planes, however, was relatively constant. By use of pulse field evaporation techniques[34] the "thickness" was found to be only one or two layers. Generally, the planes came off as a group. For example, the entire group of atoms at the $[02\bar{4}]$ pole in Fig. 19b was removed as a whole by a single pulse and can no longer be observed in Fig. 19c. However, by suitable choice

of pulse height and width, the group of atoms can occasionally be field evaporated one atom at a time. Unfortunately, the "correct" pulse height and width varies with the initial size of the plane and for this reason only a few well defined planes were successfully analyzed in each specimen. When liquid helium is used as a specimen coolant, the bright planes are stable only for about 10 minutes or less. After this period of time they generally field evaporate as a whole. Since even for the fastest commercial films available typical exposure times required for each FIM image is about 5 to 10 minutes. Therefore, the photographic recording of the actual single-atom field evaporation process will eventually require some form of image intensification.

4.2.3 As-Quenched Alloys

In as-quenched alloys, the tendency for clustering of well defined groups of atoms about the <420> matrix poles is not as pronounced as in the aged alloys. Moreover, the effect was found to be temperature dependent. Figs. 20a and 20b show the microstructure of an as-quenched alloy observed during a field evaporation sequence when liquid helium was used as a specimen coolant. Field evaporation occurs relatively uniformly over the specimen surface and the apparent clustering tendency is very weak. However, when liquid nitrogen is used as a specimen coolant field

evaporation becomes very non-uniform. Certain clusters are found to be relatively stable in that surrounding regions field evaporate at slightly lower fields. These clusters therefore protrude locally and thus act as more effective emission centers than their surrounding material (Fig. 20c). Although there is still a tendency for these groups of atoms to lie in the vicinity of the <420> poles, the effect is not as pronounced as in aged alloys. However, as in the case of aged alloys these bright groups of atoms were also found by pulse field evaporation technique to be only one or two layers thick.

4.2.4 Fluctuations in Degree of Order of As-Quenched Alloys

The liquid helium cooled specimen exhibits quite another form of domain structure. During field evaporation sequences it was found that the degree of regularity of the fundamental planes themselves vary with depth. Examples of this are shown in Figs. 20a and 20b for the (002) plane. However, the change is quite gradual showing that the degree of order is fluctuating. The justification for using these fluctuations as evidence of a diffuse domain structure is that there is an apparent orientational juxtapositioning of these fluctuations. For example in Fig. 20a an interface occurs at region A across which the rings do not match. The interface is not a grain boundary since all the fundamental

poles are in their correct angular positions. Such boundaries are quite numerous though not easily detectable by the inexperienced eye.

Since the image in Figs. 20a and 20b corresponds to a single crystal, the boundaries must be associated with fluctuations in the degree of order, that is they are order-defined boundaries. Apparently the local degree of order at A in Fig. 20a is sufficiently large for a boundary to have meaning. Also, the mismatch of the rings across the boundary indicates that the orientation of the domains on either side of the interface are not quite the same. These rather diffuse boundaries are difficult to trace in three dimensions. They fade rapidly both laterally and with depth. At best, they can be followed for only 2 or 3 consecutive layers during field evaporation sequences. The fact that the boundary rapidly fades could be explained if the degree of order rapidly decreases in surrounding regions. In fact, if such fluctuations represent reality then it is possible for a boundary not only to fade but actually terminate itself if by chance it enters a region where the local degree of order happens to be zero.

Recently Okamoto and Tong[41] have used computer simulation techniques to show that all three types of boundaries observed in ordered Ni_4Mo can be made to disappear if the

degree of order varies from unity to zero along the boundaries; the rate of disappearance depends on the type of function specifying the degree of order as a function of distance. A variety of functions were used and it was found that the boundary disappears long before the degree of order reaches absolute zero. Consequently, when the degree of order is low initially as is the case in the as-quenched alloy, order-defined boundaries will be very difficult to observe when the amplitude of the fluctuation is small.

We believe the origin of the fluctuation in the degree of order lies in small fluctuations in composition since such fluctuations are very likely to occur on the scale of observation with which we are concerned.

4.2.5 Summary of FIM Results

(a) A strong tendency for clustering of well defined planes about the <420> fcc poles is observed in all aged alloys even for those in which ordered domains were not directly resolved using TEM techniques. This observation is direct evidence of the existence of small regions possessing some form of composition variation normal to the {420} planes. The orientational dependence of the distribution of these regions is in agreement with those predicted in Section 2.

(b) In as-quenched alloys the tendency for clustering

though still present is comparatively weak. Fluctuations in degree of order has been observed in the form of diffuse domain boundaries which can be interpreted as evidence for a kind of nebulous domain structure. The fluctuations in degree of order is believed to be associated with small fluctuations in composition.

5. DISCUSSION OF RESULTS

The major conclusion of the present study is that some form of domain structure exists in as-quenched Ni_4Mo. However, there is still the question as to whether it also exists in the equilibrium disordered state above the critical ordering temperature. The similarity between the results of Tanner[22] (high temperature <002> diffraction patterns) and our own shows that the quenching process used in the present study retained the more significant features of the equilibrium disordered state. Therefore, the detection of very weak satellites near superlattice positions in <121> and <130> diffraction patterns suggests very strongly that even above the critical temperature small regions exist which have atomic arrangements similar to the LRO structure of Ni_4Mo.

FIM images of the as-quenched alloy show that the ordered regions are not well defined and are more aptly described as fluctuations in the local degree of order. The fact that the fluctuations exhibit a kind of orientational juxtapositioning resulting in localized interfaces allows us to retain the concept of a domain structure. Moreover, it is not surprising that electron dark field images fail to resolve these fluctuations. If the form of composition variation is not exactly the same in all regions, then the observed satellite intensity distribution would be comprised of

contributions from each distinct type of region. A dark field image using a satellite or its neighboring $1\frac{1}{2}0$ SRO spot would therefore not resolve distinct sets of well defined ordered particles but all regions which have some "degree of order". When the "degree of order" is low as in as-quenched alloys the dark field image should exhibit weak intensity variations which may not be sufficiently large to be detectable above background. Sharp bright spots corresponding to well defined ordered domains or particles would not be expected until the degree of order attains a certain level within the particles.

Obviously, the "degree of order" must be related to the form of the composition fluctuation, therefore, variations in the latter during the very early stages also imply that the "ordered" structure within the different regions need not necessarily be exactly the same during this critical period. The fluctuations however must account for the $1\frac{1}{2}0$ SRO peaks and the peculiar asymmetrical streaking of the satellites intensity distribution which develop during the very early stages of ordering at 650°C. These questions will now be investigated in detail.

5.1 Asymmetry in Satellite Streaking

The FIM images of alloys aged at 650°C for 10 minutes or less suggest that the domains may have a plate-like shape

with habit planes of the form {420}. However, as pointed out in Section 4.1.3, this particular morphology is not compatible with the asymmetrical streaking of the diffuse satellites which appear near superlattice positions during this critical stage of ordering. This is readily apparent if one considers the [002] pattern in Fig. 4a. If the domains are large, then domains with a Type I structure would give rise to sharp superlattice reflections represented by the white circles, while domains with a Type II structure would give rise to those represented by the black circles.

If all the domains were plate-shaped, then the habit plane for Type I domains would be $(4\bar{2}0)$ or (240). Each plate-like domain should produce shape-factor streaking normal to its own habit plane. Moreover, since layering on $(4\bar{2}0)$ and (240) results in the same Type I structure, the central maxima of the streaks should coincide at all the white circles. Therefore, each white circle should be "spiked" in the <420> and <240> directions. Similarly, each black circle should be "spiked" in the <420> and $<2\bar{4}0>$ directions as shown in Fig. 21a. The important point is that all superlattice reflections associated with a particular orientational variant should exhibit the same symmetry as far as streaking is concerned.

This is not what is observed in actual <002> patterns. As shown schematically in Fig. 21b, the expected symmetry is

absent. The actual <002> diffraction patterns can no longer be considered as a mere superposition of reflections from only two types of structures but rather from four distinct structures, each giving rise to an <002> pattern of the type shown in Fig. 21c.

This peculiar asymmetry can only be explained if the layering operation normal to the $(4\bar{2}0)$ and (240) planes are not physically equivalent. According to Fig. 2a, this means the layering sequence cannot be the same as that for a perfectly ordered Ni_4Mo structure. The same argument applies for layering normal to the (420) and $(2\bar{4}0)$ planes. In fact, during this critical stage of ordering, the non-equivalency of these pairs of planes with respect to layering will require new LRO parameters.

5.2 The Meaning of the LRO Parameter S

The Bragg-Williams long range order parameter S used in the structure factor calculation on page 10 of Section 2 must be defined relative to a particular structure. In the case of fully ordered Ni_4Mo, the structure is usually regarded in terms of 2 interpenetrating bct sublattices, one with a single Mo atom per lattice point, the other consisting of four equivalent bct sublattices each containing a single Ni atom per lattice point. If we designate the two sublattices as α and β, respectively, then

$$S = (P_{Mo\alpha} - P_{Mo\beta}) = (P_{Ni\beta} - P_{Ni\alpha})$$

where $P_{Mo\alpha}$ = fraction of α sites occupied by Mo atoms

$P_{Mo\beta}$ = fraction of β sites occupied by Mo atoms

$P_{Ni\beta}$ = fraction of β sites occupied by Ni atoms

$P_{Ni\alpha}$ = fraction of α sites occupied by Ni atoms

Since the occupational parameters are directly related to the Mo concentration of each sublattice, S can also be interpreted in terms of composition fluctuations normal to the $(4\bar{2}0)$ or (240) planes. Referring again to Fig. 2a, it is apparent that in order to generate a Type I structure, every fifth plane must contain α sites only, the intervening four must contain only β sites. This is shown schematically in Fig. 22a. To obtain the perfectly ordered structure, the composition fluctuation must have the form shown in Fig. 22b. For a partially long range ordered alloy, it must have the form shown in Fig. 22c. The composition fluctuations in these figures simply represent the distribution of Mo atoms on the two sublattices. The important point is that in order to use S as defined above, the composition of Mo atoms on the "β-planes" must be constant otherwise the four β sublattices can no longer be regarded

as equivalent. For a sinusoidal composition fluctuation such as that shown in Fig. 22d, where the period is 5 $(4\bar{2}0)$ atomic planes, there will be two non-equivalent sublattices: β_1 and β_2. Each will require its own occupation parameter $P_{Mo\,\beta 1}$ and $P_{Mo\,\beta 2}$ and hence, two LRO parameters will be required to specify the degree of order.

Although the new order parameters will still be defined relative to the bct lattice, the equivalency of the $(4\bar{2}0)$ and (240) planes with respect to the fluctuations like that shown in Fig. 22d will be lost. Within a single domain, fluctuations normal to the $(4\bar{2}0)$ planes will no longer automatically result in an identical fluctuation normal to the (240) or vice-versa. However, such fluctuations can occur normal to the (420) planes in one domain and normal to the (240) planes in another domain, but the structures are not equivalent and must be classified as Type IA and Type IB. Similarly, fluctuations normal to (420) and $(2\bar{4}0)$ planes result in Type IIA and Type IIB structures respectively.

If, for example, the period of the sinusoidal composition fluctuations is less than the 5 $(4\bar{2}0)$

atomic planes then such fluctuations occurring normal to the $(4\bar{2}0)$ plane will result in a structure which is no longer based on the bct lattice. The small rectangular unit cells shown in Fig. 21c show however, that if the period happens to be exactly 4 (420) atomic planes the resulting structure is such that within a single domain the (420) and $(4\bar{2}0)$ become equivalent with respect to such fluctuations. Similar arguments apply to the (240) and $(2\bar{4}0)$.

5.3 The Mechanism of Ordering in Ni_4Mo

By this time it will not have escaped the reader that in our attempt to develop a physical model of the ordering mechanism in terms of layering or more aptly composition fluctuations on a microscopic scale, we lose in the process the concept of a well defined LRO structure. In order to restore some perspective we will now summarize the key results. In so doing, we will give up entirely the concept of an ordered structure and state the results in terms of composition fluctuations occurring normal to {420} planes of the reference fcc lattice.

Above the so-called critical ordering temperature we believe composition fluctuations exist everywhere on a microscopic scale. In a particular region the fluctuations

occur normal to one of the 12 {420} planes. The composition fluctuation is composed of two kinds of composition waves which we will refer to as the SRO and LRO components. The SRO component has a wavelength of 4d and the LRO component a wavelength of 5d, where d is the interplanar spacing of the {420} planes.

As far as diffraction effects are concerned, the SRO component gives rise to satellites at the $1\frac{1}{2}0$ positions in reciprocal space, while the LRO components give rise to the diffuse satellites near superlattice positions. The relative intensities of the two kinds of satellites will depend on the relative amplitude of SRO and LRO components of the composition fluctuation. The ordering reaction can then be described in terms of the change in relative amplitudes of the two components with aging time. Initially the SRO component dominates giving rise to strong satellites at the $1\frac{1}{2}0$ position. The weaker LRO component gives rise to the diffuse satellites near superlattice positions. Towards the end of the reaction the LRO component dominates giving rise to sharp superlattice reflections. Somewhere in between the two components will be of equal strength and will give rise to an asymmetrical streaking of the diffuse satellites. The concept of ordered domains or particles is retained only through the result of interference between the SRO and LRO components.

The relationship between composition fluctuations and the various satellite reflections is analogous to the "side band" formation which appear during the initial stages of spinodal decomposition. In fact, the $1\frac{1}{2}0$ SRO spots and diffuse superlattice reflections in Fig. 21c may be interpreted during the initial stages as side bands which eventually develop into superlattice reflections. A diffraction model based on these ideas is completely developed in Appendix I.

5.4 Qualitative Discussion of Satellite Amplitude Spectrum

In the diffraction model derived in Appendix I, there are two adjustable parameters which may be used to specify the state of order in terms of composition waves. They are (a) the amplitudes $(1-\epsilon)$ and ϵ of the SRO and LRO components respectively and (b) the wavelengths of the two components. The effect of these parameters on the satellite scattering amplitude spectrum is shown in Fig. 24 and Fig. 25. Changes in the relative amplitudes of the two components produce a change in the relative scattering amplitudes of the satellites. The transition from the SRO to the LRO state can be represented by letting ϵ vary from zero to unity. A change in the wavelengths of the two components results in a shift in the position of the peak amplitude of the satellites. A slight increase in the wavelength of the SRO component will cause

all satellites to shift inward towards their associated matrix reflection. On the other hand, a slight decrease in the wavelength of the LRO component will cause all satellites to shift outward away from their associated matrix reflection. The two components interfere and result in the familiar beat phenomena.

In all cases the resultant composition fluctuation is represented by a sinusoidal wave modulated with respect to amplitude. The period of the modulation is proportional to the difference $\left(\frac{1}{\lambda_{SRO}} - \frac{1}{\lambda_{LRO}} \right)$ where λ_{SRO} and λ_{LRO} are the wavelengths of the SRO and LRO components, respectively. The "size" of the domain is taken as the distance between nodal points which is always one-half the period of the modulation. As shown in Figs. 24 and 25, the propagation of composition waves within a small region of the alloy would produce an array of domains. Within each domain the Mo concentration fluctuates rapidly, being highest on one or two planes near the middle of the domain and decreasing rapidly towards the domain boundary. However, the domain boundary is not very distinct especially during the very initial stages of ordering (Fig. 24a). This type of domain structure is compatible with our FIM results. The bright well defined planes clustering around the <420> poles would correspond to the planes with high Mo concentration. It is also consistent with the

observation that the planes appear to be only one or two layers "thick". The diffraction model indicates however that this may not be a good measure of domain size since planes with higher than average Mo concentrations will be preferentially imaged over other planes. The actual thickness as represented by the diffraction model would be about 20 (420) atomic planes (Figs. 24 and 25) which corresponds to about 16Å for disordered Ni_4Mo.

The model is, of course, a drastic oversimplification. We are assuming the composition fluctuation consists of only two components. In reality, a whole spectrum of wavelengths between λ_{SRO} and λ_{LRO} will be excited, leading to interference effects and hence to domains. Each wavelength would give rise to its own set of satellites resulting in a smearing out of the satellite scattered amplitude spectrum as shown in actual diffraction patterns (Fig. 12). If Δk is a measure of the width of this spectrum in wave vector space, then the domain size will be given by $\frac{2\pi}{\Delta k}$. Hence, the usual method of estimating the size of small particles by the breadth of the diffraction spots they produce will still be valid for our diffraction model. However, the effect is not the same as shape-factor streaking since a plate-like shape is not necessary for the type of broadening predicted by the model. The sharpening of the satellites

into superlattice reflections would correspond to a sharpening of the Fourier spectrum of the composition fluctuation, (i.e., $\Delta k \rightarrow 0$). This simply corresponds to domain growth. When this happens the asymmetrical streaking of the satellites disappears and we can go back to the original description of the domain structure developed in Section 2.

5.5 Summary of Discussion

The diffraction model developed in this thesis relates the intensity distribution in reciprocal space to the Fourier spectrum of composition fluctuations in disordered (SRO) alloys. It therefore provides us with a physical description of the SRO state in terms of domains which form in small regions of the alloy. The change in the intensity distribution which occurs during the initial stages of ordering provides us with a physical description of the structural changes which occur during this critical period. The question we now ask is whether the interpretation can be applied to systems other than Ni_4Mo. More specifically, we would like to know whether it can be applied to the results of the Clapp-Moss statistical-thermodynamical theory of SRO which specifically denies the existence of domains at least in disordered Ni_4Mo.[20] This will be of critical importance since the beauty of their theory is its ability to predict the intensity distribution from disordered alloys for a great many alloy systems.

In the next section we shall reexamine the physical significance of the present results in the light of the very recent theoretical work of Hilliard's group at Northwestern.[44] We will then show how the latter theory, which is essentially a "spinodal" approach to order-disorder transformation, can be related to the Clapp-Moss statistical-thermodynamic theory of SRO. This will allow us to reinterpret the predictions of the Clapp-Moss theory in terms of the diffraction model developed in this thesis.

6. RELATION BETWEEN THE SPINODAL APPROACH AND THE CLAPP-MOSS THEORY

The diffraction model derived in Appendix I was originally developed for the purpose of explaining the presence of the $1\frac{1}{2}0$ SRO maxima and the asymmetrical streaking of the diffuse satellites which appear during the early stages of ordering in Ni_4Mo. However, like similar models used to explain side band formation during spinodal decomposition[42,43] it does not provide any information as to why transformations give rise to a particular kind of scattering.

The answer has now been provided in part by the discrete counterpart of Cahn's continuum theory of spinodal decomposition recently developed by Cook, deFontaine and Hilliard.[44]

6.1 Spinodal Approach to O-D Transformations

The basis of Cahn's[45] theory of spinodal decomposition is the diffusion equation:

$$\dot{C} = \left(\frac{M}{Nv}\right) \left[(f'' + 2\eta^2 Y)\nabla^2 C - 2K\nabla^4 C \right] \tag{1}$$

in which $\left.\begin{aligned} f'' &= (\partial^2 f/\partial c^2) \\ &= (d\ln a/dc) \end{aligned}\right\}$ evaluated at $C = Co$

where f is the Helmhotz free energy per unit volume, C the atomic fraction of component B, Co the average composition, Y a function of the elastic constants, N_v the number of atoms per unit volume, a the lattice

parameter, K the gradient energy coefficient and M an atomic mobility.

Cahn's continuum formulation is restricted to composition variations with wavelengths long compared to atomic spacings and is therefore restricted to systems for which K is positive. If K is negative as in ordering systems, Eq. (1) predicts the growth of composition fluctuations with infinitely short wavelengths.

This restriction was removed in the treatment by Cook, deFontaine and Hilliard. They derived a finite difference equation that is the analog of Eq. (1) for the special case when $\eta = 0$. For the general three dimensional case the diffusion equation is:

$$\dot{C}_p = \left(\frac{M}{2a^2 N_v}\right) \sum_r \left[f'' \Delta_r^2 C_p - \left(\frac{K}{2a^2}\right) \sum_{r'} \Delta_{r'}^2 \left(\Delta_r^2 C_p \right) \right] \tag{2}$$

where C_p is defined as the probability, with respect to the initial distribution, of finding a B atom at site p after time interval Δt. The other parameters have the same meaning as in Cahn's treatment. The summation is taken over all nearest neighbor sites about site p and $\Delta_r^2 C_p$ is the second difference defined by:

$$\Delta_r^2 C_p = C_{p+r} - 2C_p + C_{p-r}$$

During the very early stages of spinodal decomposition or ordering the amplitude of the composition variations will be small. By assuming that under these conditions the compositional dependence of f", K and M can be neglected, Cook showed that the general solution to Eq. (2) is given by:

$$C_p(t) = \sum_h \left\{ A^\circ(h)\, e^{\alpha(h)t} \right\} e^{i\bar{k}(h)\cdot\bar{x}_p} \tag{3}$$

where $\bar{x}_p$ is the vector joining the origin to site p, $\bar{k}(h)$ is a wave vector from the origin to point (h) in reciprocal space, $A^\circ(h)$ is the amplitude of the Fourier component of wave vector k(h) at time zero and $\alpha(h)$ is an amplification factor given by:

$$\alpha(h) = -\left(\frac{M}{N_v}\right) B^2(h)\left[f'' + 2KB^2(h)\right] \tag{4}$$

in which

$$B^2(h) = \frac{1}{a^2}\sum_r \left[1 - \cos \bar{k}(h)\cdot\bar{x}_r\right] \tag{5}$$

where $\bar{x}(r)$ is a vector joining site p to a nearest neighbor site and the summation is over all nearest neighbor sites.

The amplification factor determines the rate of growth or decay of a particular Fourier component. For a given point (h) in reciprocal space the sign and magnitude of $\alpha(h)$ depends on the signs and relative magnitudes of f" and K.

In ordering systems where the free energy versus composition is everywhere concave upward f" is positive. K is proportional to an interaction energy[46] which for ordering systems is always negative.

The relationship between the amplification factor $\alpha(h)$ and the intensity distribution associated with ordering effects can be examined by assuming that the atomic scattering factor for site p varies in phase with the composition C_p (See Eq. (A.3) in Appendix I).

then

$$f_p = fo + (f_B - f_A) \quad C_p - Co \tag{6}$$

where f_A and f_B are the scattering factors for A and B atoms and fo is the average scattering factor for the system. Substitution of Eq. (6) into the usual expression for the scattered amplitude, F(k) we obtain

$$\begin{aligned} F(k) &= \sum_p f_p e^{-i\bar{k}\cdot\bar{x}_p} \\ &= f_o \sum_p e^{-i\bar{k}\cdot\bar{x}_p} + (f_B - f_A) \sum_p [c_p - c_o] e^{-i\bar{k}\cdot\bar{x}_p} \end{aligned} \tag{7}$$

The first term gives rise to the matrix reflections while the second term contains all the information on the modulation of the diffuse scattering caused by ordering effects. The sum is simply the Fourier transform of Eq. (3). Hence, the

order part of the scattered amplitude can be written

$$F(k,t)_{\text{order}} = (f_B - f_A)\{A^{o}(h)e^{\alpha(h)t}\} \tag{8}$$

where N is the number of points (h) in the first Brillouin zone. Therefore, the intensity is given by

$$F^{2}(k,t)_{\text{order}} = F^{2}(k,0)\, e^{2\alpha(h)t} \tag{9}$$

The intensity associated with ordering effects will therefore be a maximum at those points (h) in reciprocal space where the amplification factor takes on its absolute maximum value. But according to Eq. (4) this occurs when $f'' + 2KB^2(h)$ is an absolute minimum (i.e., largest negative value). Since $f'' > 0$ and $K < 0$ for ordering systems the latter occurs when $B^2(h)$ attains its absolute maximum value.

For fcc systems Eq. (5) is given by

$$B^2(h) = \frac{12}{a^2}\left[1 - \frac{1}{3}(\cos\pi h_1 \cos\pi h_2 + \cos\pi h_1 \cos\pi h_3 + \cos\pi h_2 \cos\pi h_3\right] \tag{10}$$

Therefore, the diffuse intensity associated with ordering effects will attain its maximum value at the points $(h) = (h_1, h_2, h_3)$ in reciprocal space where the function

$$C(h_1 h_2 h_3) = \frac{1}{3}\left[\cos\pi h_1 \cos\pi h_2 + \cos\pi h_1 \cos\pi h_3 + \cos\pi h_2 \cos\pi h_3\right] \tag{11}$$

attains its absolute minimum value. $C(h_1,h_2,h_3)$ is plotted in the $h_3 = 0$ plane in Fig. 26. The plot corresponds to one quadrant of the [002] diffraction pattern (Fig. 6a). The contour lines are the locus of points for which $C(h_1,h_2,0)$ is a constant. The minimum value of $C(h_1,h_2,0)$ is (-1/3) at all points of the line between the (100) and $1\frac{1}{2}0$ and all crystallographically equivalent points.

Fig. 24 shows that any composition wave whose wave vector ends on the line joining (100) and $(1\frac{1}{2}0)$ will be selected for growth, all others will decay with time. The wave vectors ending on the $1\frac{1}{2}0$ points correspond to composition waves normal to the {420} planes with wavelengths equal to $(2\pi/k_{1\frac{1}{2}0})$ or 4d where d is the interplanar spacing of the {420} planes. This is precisely the composition wave used as the SRO component in our own diffraction model. Fig. 24, however, shows that any other composition fluctuation whose wave vector also ends on the (100) - $(1\frac{1}{2}0)$ line can also be selected for growth. The reason why they are not in Ni_4Mo will be seen after discussion of the Clapp-Moss theory.

6.2 The Clapp-Moss Theory of SRO

According to the classical statistical-thermodynamic treatment of SRO,[3] the diffuse intensity due to SRO is given by

$$I(k)_{\text{order}} = N m_A m_B (f_B - f_A)^2 \sum_{lmn} \alpha_{lmn} e^{-i\bar{k}\cdot\bar{x}_{lmn}} \tag{12}$$

where N is the total number of atoms in the crystal, m_A and m_B are the atomic fraction of A and B components, respectively, f_A and f_B are the atomic scattering factors for A and B atoms, $\bar{k}$ is a wave vector in reciprocal space, α_{lmn} is the Warren SRO parameter defined by

$$\alpha_{lmn} = 1 - \frac{P^{BA}_{o,lmn}}{m_B} \tag{13}$$

in which $P^{BA}_{o,lmn}$ is the probability of finding an A atom at site lmn given that a B atom is at the origin. According to the classical treatment, the conditional pair probability depends only on the sites lmn and the origin. Clapp and Moss in effect claim that the correlation between the two sites is not direct but depends on the atomic configuration between the two sites. Placing an A atom at site lmn will in effect polarize a particular kind of atomic configuration around the site chosen as origin. The probability that a B atom will occupy the origin will be determined by this polarized atomic configuration. Stated somewhat differently, the information that an A atom is at site lmn will be transmitted to the atom at the origin through its neighboring atoms at sites f. The "strength" of the signal received at the origin from a particular site f is proportional to the interaction energy V_{of} between that site and the origin. If $\alpha_{f,lmn}$ is the Warren SRO parameter for the sites f and lmn, then the Warren SRO

parameter for site lmn and the origin is

$$\alpha_{lmn} = -2m_A m_B \sum_f V_{of}\, \alpha_{f,lmn} \tag{14}$$

The interaction energy between two sites i and j is given by

$$V_{ij} = \frac{1}{2}\left(V_{ij}^{AA} + V_{ij}^{BB} - 2V_{ij}^{AB}\right) \tag{15}$$

for ordering systems V_{ij} is negative. It is assumed to have the form

$$V_{of} = \frac{1}{v_k}\int V(k)\, e^{-i\bar{k}\cdot\bar{x}_f}\, d^3\bar{k} \tag{16}$$

where $\bar{x}_f$ is the vector joining the origin to site f and the integration is taken over one unit cell of the reciprocal lattice, the volume of which is v_k. Eq. (14) is the basis of the Clapp and Moss theory of SRO. It was derived from an infinite set of nonlinear equations in the α_{lmn}'s which in general must be solved in some approximate way to separate the α_{lmn}'s. The approximations used by Clapp and Moss was to neglect certain higher order terms in the infinite set of nonlinear equations which in effect limits the validity of Eq. (14) to temperatures much higher than the critical ordering temperature.

The set of equations given by Eq. (14) can be diagnolized by introducing V_{of} and the Fourier transforms

of α_{lmn} from Eq. (12). This yields equations in terms of $I_{order}(k)$ and $V(k)$ which give for any value of k

$$I_{order}(k) = \frac{\text{constant}}{1+2m_A m_B \beta V(k)} \tag{17}$$

where $\beta = \frac{1}{kt}$, k is the Boltzman constant.

Therefore, according to the Clapp-Moss theory, the diffuse intensity associated with ordering effects will have its maximum value at those points in reciprocal space where the denominator in Eq. (17) attains its absolute minimum value, i.e., where the Fourier coefficients V(k) attains its absolute minimum value. From Eq. (16) V(k) is given by

$$V(k) = \sum_f V_{of}\, e^{i\,\bar{k}\cdot\bar{x}_f} \tag{18}$$

For cubic crystals there is for each site f another site at -f which has the same value V_{of} hence the sine terms cancel leaving

$$V(k) = \sum_f V_{of} \cos \bar{k}\cdot\bar{x}_f$$

For fcc crystals the explicit expression for V(k) for nearest neighbor interactions only is

$$\begin{aligned} V(k) &= 12V_1\left[\tfrac{1}{3}(\cos\pi h_1 \cos\pi h_2 + \cos\pi h_1 \cos\pi h_3 \right. \\ &\qquad \left. + \cos\pi h_2 \cos\pi h_3\right] \\ &= 12V_1\, C(h_1 h_2 h_3) \end{aligned} \tag{19}$$

Hence, the diffuse intensity associated with ordering effects will attain its maximum value when $C(h_1 h_2 h_3)$ attains its absolute minimum value. This is precisely the same condition required by the spinodal theory (Eq. (11)). Therefore to this degree, they are mathematically equivalent.

However, the equivalence is more than a mathematical coincidence. Both theories in effect predict that the probability of a site being occupied by a B atom will depend primarily on the atomic configuration of near neighbor sites. In the case of the spinodal theory this effect is introduced through the concept of a free energy term arising from composition variations between sites. The free energy contribution from a particular site p will be proportional to the square of the concentration gradient between site p and its nearest neighbor sites p + r, i.e., proportional to $\sum_r [C_p - C_o]^2$. The proportionality factor is K the gradient energy coefficient and plays the same role as V_{of}, the interaction energy in the Clapp-Moss theory. In both theories the "polarized" atomic configuration about a site p will be such as to minimize the total free energy of the alloy. When only first nearest neighbor interactions only are considered both theories predict intensity maxima at the same places in reciprocal space. However, the spinodal theory retains the concept of domains in the same way as the

simple diffraction model developed in this thesis. If K, the gradient energy coefficient is retained under the summation sign in Eq. (2) the spinodal theory could in principle be extended to include interactions beyond first nearest neighbors.

If we therefore assume that the mathematical and physical equivalence between the two theories holds also up to second nearest neighbors, then the predictions of the Clapp-Moss theory which includes higher neighbor interactions could be interpreted in terms of a propagation of composition waves at least during the very initial stages of ordering.

If the second nearest neighbor interactions are also included V(k), the interaction energy in the Clapp-Moss theory becomes for fcc crystals,

$$V(k) = 12V_1C(h_1h_2h_3) + 6V_2C'(h_1h_2h_3) \tag{20}$$

where $C'(h_1h_2h_3) = 1/3(\cos 2\pi h_1 + \cos 2\pi h_2 + \cos 2\pi h_3)$. According to this theory V(k) is a minimum at all $1\frac{1}{2}0$ positions in the fcc reciprocal lattice of disordered Ni_4Mo. For suitable choices of T in Eq. (17) and V_2 and V_1 in Eq. (20), Clapp and Moss were able to match the experimentally determined x-ray intensity contour maps for the [002] reciprocal lattice section obtained by Spruiell and Stansbury from as-quenched Ni_4Mo. The best match was obtained for the values $T = 1.05T_c$

and $V_2 = 0.300V_1$. The agreement was quite good and as a result, Clapp and Moss concluded that the concept of small ordered domains is not valid in disordered Ni_4Mo.

The results of the present study based on both electron diffraction and field ion microscopy observations provide very strong evidence of some form of ordered domains in as-quenched alloys which have atomic arrangements similar to but not exactly that of the long range ordered structure of Ni_4Mo. In fact, since the physical basis of the Clapp-Moss theory and the spinodal theory are very similar, at least during the very initial stages of ordering, we can interpret the results of the Clapp-Moss theory in terms of domains. In Ni_4Mo, V(k) is a minimum at all $1\frac{1}{2}0$ positions, according to the spinodal interpretation, this means the composition fluctuations receiving maximum amplification will be those occurring normal to the {420} planes having wavelengths equal to $(2\pi/k_{1\frac{1}{2}0})$ or $4d_{420}$. This is the same composition wave that was termed the SRO component in the simple diffraction model developed in this thesis.

Actual diffraction patterns of as-quenched Ni_4Mo and the high temperature diffraction patterns of Au_3Cr exhibit quite diffuse spots indicating that in real alloys many composition waves are excited having a range of k-vectors close to, but not exactly equal to $k_{1\frac{1}{2}0}$ in reciprocal space.

Moreover, the presence of very weak diffuse satellites in as-quenched Ni_4Mo indicates the distribution of k-vectors about $k_{1\frac{1}{2}0}$ is not symmetrical but extends preferentially towards shorter k values near $2\pi/5d_{420}$. Consequently, in the disordered alloy the various excited composition waves should interfere resulting in "domains" whose size normal to the {420} planes is inversely proportional to the breadth Δk of the k-spectrum. Since this concept is also in agreement with the present FIM observations we end this section by concluding that the concept of ordered domains is valid in disordered Ni_4Mo.

7. SUMMARY AND CONCLUSIONS

A parallel transmission electron and field ion microscopy study of disordered Ni_4Mo and of alloys aged for very short times at 750°C and 650°C have shown the following:

(a) In as-quenched alloys very weak satellites exist near superlattice positions corresponding to the LRO structure of Ni_4Mo. These satellites are detectable only in electron diffraction patterns of certain favorable orientations and are completely obscured by neighboring $1\frac{1}{2}0$ SRO spots in <002> diffraction patterns.

(b) During the initial stages of ordering at 650°C the satellites develop a peculiar asymmetry in their direction of streaking in various <210> directions. Satellites which upon aging eventually develop into superlattice reflections corresponding to ordered domains of a particular orientation variant are not initially streaked in the same <210> direction.

(c) At 650°C, tiny ordered domains are directly resolved in dark field images using either $1\frac{1}{2}0$ SRO spots or its neighboring satellites only after 10 minutes of aging. At 750°C the ordering reaction is essentially complete within 5 to 10 seconds of aging.

(d) Field ion images of as-quenched and aged alloys exhibit clustering of well defined groups of atoms about the <420> poles of the fcc lattice. The effect is most pronounced in aged alloys in which ordered regions are directly resolved by transmission electron microscopy techniques. The unique orientational dependence of the distribution of the well defined groups of atoms is direct evidence of tiny ordered regions possessing an atomic arrangement in which the Mo concentration is varying on the {420} planes. The variation is similar to, but not exactly the same as the LRO structure of Ni_4Mo.

(e) An explanation for the above observations is given in terms of composition modulations occurring normal to the {420} planes in small regions of the crystal. A diffraction model based on this idea explains not only the presence of intensity maxima at the $1\frac{1}{2}0$ positions but also the presence of the weak satellites near superlattice positions. The model is also compatible with the FIM observations and suggests that the bright well defined groups of atoms represent planes within domains which have the highest Mo concentration. The physical basis for the diffraction model is given in terms of the recently developed spinodal approach to order-disorder transformation. The model is also compatible with the Clapp-Moss theory of SRO.

The overall results suggest that disordered Ni_4Mo consists of tiny regions possessing some form of ordering, at least in the as-quenched disordered alloys and possibly in the equilibrium disordered state above the critical ordering temperature. However, at very high temperatures where diffusion can take place easily, such regions may have only a temporary existence both in space and in time. In this sense, the statistical-thermodynamic view of SRO would be correct but there will probably be an equilibrium distribution of such regions both in number, size and degree of order when all instantaneous distributions are averaged over a finite time interval. This must be the case since the diffraction patterns taken above and below the critical ordering temperature are very similar. In this sense, the microdomain or discrete particle concept of SRO would have some validity even above the critical ordering temperature.

Upon quenching however a particular distribution will be frozen in. In this case the microdomain or discrete particle view of SRO must be a more accurate physical description than the liquid-like arrangement presented by the statistical-thermodynamic viewpoint.

However, the present study also indicates that the form of ordering within the domains or particles is best described in terms of composition fluctuations rather than a specific

ordered structure. It has been shown that the latter can change during the very initial stages of ordering. On the other hand, knowledge of the amplitudes and wavelengths of the various components producing the composition fluctuation contain all the information regarding "structure", domain size and the degree of order. Since the average composition on the various planes within a typical domain will be known, equivalent sublattices can be specified and hence the Bragg-Williams LRO parameter, or for that matter the Warren SRO parameters, can be calculated.

ACKNOWLEDGEMENTS

The author is deeply indebted to his research advisor, Prof. Gareth Thomas for his encouragement and very stimulating discussions during critical periods of this investigation. He would also like to express his appreciation to Dr. H. Tong for numerous interesting discussions on the field ion work. Thanks are also due to my wife, Shirley for typing numerous drafts and the final version of this thesis.

This work was carried out under the auspices of the United States Atomic Energy Commission through the Inorganic Materials Research Division of the Lawrence Radiation Laboratory.

REFERENCES

1. Z. W. Wilchinsky, J. Appl. Phys. 15, 806 (1944).
2. B. E. Warren and B. L. Averbach, "The Diffuse Scattering of X-rays" in Modern Research Techniques in Physical Metallurgy, ASM, Cleveland, 1953.
3. C. J. Sparks and B. Borie, "Methods of Analysis for Diffuse X-ray Scattering Modulations by Local Order and Atomic Displacements", in Local Atomic Arrangements Studied by X-ray Diffraction, AIME, New York, 1966.
4. H. Lipson, Prog. Metal Phys. 2, 1 (1950).
5. A. J. Wilson, X-ray Optics, Methuen, London, (1949).
6. B. Batterman, Ph.D. Thesis, MIT, Cambridge, Mass. (1956).
7. I. G. Edmunds and R. M. Hinde, Proc. Phys. Soc. 65, 716 (1952).
8. J. K. Raether, Angewandte Physik, 4, 53 (1952).
9. S. Yamaguchi, D. Watanabe and S. Ogawa, J. Phys. Soc. Japan, 17, 1030 (1961).
10. M. J. Marcinkowski, in Electron Microscopy and Strength of Crystals, Ed. G. Thomas and J. Washburn, Interscience, New York, (1963).
11. B. W. Roberts, Acta. Met., 2, 597 (1954).
12. M. Hirabayashi and S. Ogawa, J. Phys. Soc. Japan, 11, 907 (1956).

13. Y. D. Tyapkin and K. M. Yamaleev, Soviet Phys-Dokl, 9, 322 (1964).

14. H. N. Southworth and B. Ralph, Phil. Mag., 14, 383 (1966).

15. C. A. Taylor, R. M. Hinde and H. Lipson, Acta. Cryst. 4, 261 (1951).

16. P. C. Gehlen and J. B. Cohen, Phys. Rev. A844 (1965).

17. J. M. Cowley, J. Appl. Phys. 21, 24 (1950).

18. P. C. Clapp and S. C. Moss, Phys. Rev. 142, 418 (1966).

19. P. C. Clapp and S. C. Moss, Phys. Rev. 171, 754 (1968).

20. S. C. Moss and P. C. Clapp, Phys. Rev. 171, 764 (1968).

21. J. E. Spruiell and E. E. Stansbury, J. Phys. Chem. Solids, 26, 811 (1965).

22. L. E. Tanner, P. C. Clapp and S. Toth, Mat. Res. Bull., 3, 855 (1968).

23. H. G. Baer, Z. Metallk., 57, 318 (1966).

24. E. Ruedl, P. Delavignette and S. Amelincx, Phys. Stat. Sol., 28, 305 (1968).

25. B. G. LeFevre, A. G. Guy and R. W. Gould, Trans. AIME, 242, 788 (1968).

26. B. G. LeFevre and R. W. Newman, Proc. Symposium on Field Ion Microscopy in Physical Metallurgy, Georgia Inst. Technology, Atlanta, Georgia, 1968.

27. P. V. Guthrie and E. E. Stansbury, USAEC Report ORNL-3078 (1961).

28. A. W. Moore and S. Ranganathan, Phil. Mag., 16, 723 (1967).

29. B. G. LeFevre, H. Greng and B. Ralph, Phil.Mag.(In Press).

30. R. W. Newman and J. J. Hren, Phil. Mag. 16, 211 (1967).

31. S. Ranganathan, H. B. Lyon and G. Thomas, J. Appl. Phys. 38, 4957 (1967).

32. E. W. Muller, Advan. Electron and Electron Physics, 13, 83 (1960).

33. J. J. Hren and S. Ranganathan, Field Ion Microscopy, Plenum, New York, 1968.

34. P. Petroff, Ph.D. Thesis, Univ. of Calif., Berk., Calif. 1968.

35. R. B. Nicholson and J. Nutting, Acta. Met. 9, 332 (1961).

36. H. Warlimont and G. Thomas, Met. Sci. (In Press).

37. W. Gaudig, P. Okamoto, G. Shanz, G. Thomas and H. Warlimont, Proc. Third Bolton Landing Conference on Ordered Alloys, Lake George, New York, 1969.

38. E. P. Butler and G. Thomas, USAEC Report UCRL-18840, 1969.

39. R. Livak and G. Thomas (to be published).

40. L. E. Tanner, Phil. Mag., 14, 111 (1966).

41. P. R. Okamoto and H. Tong (Submitted to Acta. Met.).

42. V. Daniels and H. Lipson, Proc. Roy. Soc. A181, 378 (1943).

43. M. E. Hargreaves, Acta. Cryst. 4, 301 (1951).

44. H. E. Cook, D. deFontaine and J. E. Hilliard, Acta. Met. 17, 765 (1969).

45. J. W. Cahn, Acta. Met. 9, 795 (1961).

46. J. W. Cahn and J. E. Hilliard, J. Chem. Phys. 28, 258 (1958).

APPENDIX I

A Diffraction Model of Scattering by Composition Fluctuations in Ni_4Mo

In this appendix a kinematical diffraction model is developed for scattering from a binary alloy comprised of regions or domains which are modulated by composition fluctuations. The treatment is based on one developed by V. Daniels and H. Lipson[42] to explain side-band formation during the initial stages of spinodal decomposition. We shall consider only the one dimensional modulated structure as it brings out all the essential features of the general three dimensional case while greatly simplifying the mathematics.

Amplitude Scattered by Composition Fluctuations

Consider a local region of our one dimensional binary alloy. Let the region consist of N atomic planes of spacing d perpendicular to the direction of the one dimensional composition fluctuation. Let C_p be the atomic fraction of B atoms of the pth atomic plane whose position is x_p and C_o be the average composition of the alloy. We assume that the composition fluctuation within this local region can be described by

$$C_p - C_o = (1 - \epsilon)\cos k_{SRO}x_p + \epsilon \cos k_{LRO}x_p \qquad (A.1)$$

where k is a wave vector equal to $2\pi/\lambda$. In exponential form Eq. (A.1) can be written:

$$C_p - C_o = \frac{1}{2}(1-\epsilon)e^{ik_{SRO}x_p} + \frac{1}{2}(1-\epsilon)e^{-ik_{SRO}x_p} + \frac{1}{2}\epsilon e^{-ik_{LRO}x_p} + \frac{1}{2}\epsilon e^{ik_{LRO}x_p} \tag{A.2}$$

The planar scattering power f_p of the pth atomic plane is then

$$f_p = C_p f_B + (1-C_p)f_A$$

where f_B and f_A are the atomic scattering factors for B and A atoms, respectively. Similarly the planar scattering power f_o for the whole alloy of average composition C_o is

$$f_o = C_o f_B + (1-C_o)f_A$$

thus

$$f_p - f_o = (f_B - f_A)\,[C_p - C_o] \tag{A.3}$$

The scattered amplitude from the domain is

$$F(s) = \sum_p f_p\, e^{-2\pi i s x_p}$$

Introducing Eq. (A.3) and Eq. (A.2) we obtain

$$F(s) = f_o \sum_p e^{-2\pi i s x_p} + \frac{\gamma}{2}(1-\epsilon)\sum_p e^{-2\pi i (s + k_{SRO}/2\pi)x_p} + \frac{\gamma}{2}(1-\epsilon)\sum_p e^{-2\pi i (s - k_{SRO}/2\pi)x_p} + \frac{\gamma}{2}\epsilon\sum_p e^{-2\pi i (s + k_{LRO}/2\pi)x_p} + \frac{\gamma}{2}\epsilon\sum_p e^{-2\pi i (s - k_{LRO}/2\pi)x_p}$$

where $\gamma = (f_B - f_A)$ (A.4)

Introducing $X_p = pd$, and summing over all N planes we get

$$F(s) = f_o \frac{\sin \pi N s d}{\sin \pi s d} e^{-\pi i (N-1) s d}$$

$$+ \frac{\gamma}{2}(1-\epsilon) \frac{\sin \pi N (s - k_{SRO}/2\pi) d}{\sin \pi (s - k_{SRO}/2\pi) d} e^{-\pi i (N-1)(s - k_{SRO}/2\pi) d}$$

$$+ \frac{\gamma}{2}(1-\epsilon) \frac{\sin \pi N (s + k_{SRO}/2\pi) d}{\sin \pi (s + k_{SRO}/2\pi) d} e^{-\pi i (N-1)(s + k_{SRO}/2\pi) d}$$

$$+ \frac{\gamma}{2}\epsilon \frac{\sin \pi N (s + k_{LRO}/2\pi) d}{\sin \pi (s + k_{LRO}/2\pi) d} e^{-\pi i (N-1)(s + k_{LRO}/2\pi) d}$$

$$+ \frac{\gamma}{2}\epsilon \frac{\sin \pi N (s - k_{LRO}/2\pi) d}{\sin \pi (s - k_{LRO}/2\pi) d} e^{-\pi i (N-1)(s - k_{LRO}/2\pi) d} \qquad (A.5)$$

The first term has a maximum value Nf_o at values of S where the denominator vanishes hence simply contributes to the matrix reflections at

$$S = \frac{n}{d} = ng, \quad (n = 0, \pm 1, \pm 2, \ldots.)$$

The remaining terms give rise to two sets of satellites.

Type I satellites occur at

$$S = ng \pm \frac{k_{SRO}}{2\pi}, \quad (n = 0, \pm 1, \pm 2, \ldots.)$$

$$\text{Maximum Amplitude} = \frac{\gamma}{2} N(1 - \epsilon)$$

Type II satellites occur at

$$S = ng \pm \frac{k_{LRO}}{2\pi}, \quad (n = 0, \pm 1, \pm 2, \ldots.)$$

$$\text{Maximum Amplitude} = \frac{\gamma}{2} N\epsilon$$

For the case when the two components of the composition fluctuation in Eq. (A.1) have the wavelengths $\lambda_{SRO} = 4d$ and $\lambda_{LRO} = 5d$, then $k_{SRO}/2\pi = (1/4)g$ and $k_{LRO}/2\pi = (1/5)g$ where g is the reciprocal lattice vector for the planes. Hence, each matrix reflection at ng, (n = 0, ±1,....) will be flanked by two sets of satellites located at distances 1/4g and 1/5g on either side of it.

The relative magnitudes of the Type I and II satellites will depend on ϵ. Fig. 24 shows the composition profiles and corresponding amplitude spectrum for various values of ϵ. In each case the composition profile is described by a sinusoidal wave modulated with respect to amplitude, the period of the modulation being proportional to the difference $(1/\lambda_{SRO} - 1/\lambda_{LRO})$. These modulations in composition can be interpreted as domains. Within each domain the composition fluctuates rapidly, being highest near the middle of each domain and decreasing rapidly towards the domain boundary in the case where the two components are of equal strength. When one of the components dominates, the boundary is quite diffuse.

When the SRO component dominates, the period of the composition fluctuation within each domain is very nearly equal to λ_{SRO}. This would correspond to the situation discussed in Section 5.2 when the domains have a structure which no longer can be considered as ordered Ni_4Mo.

When the LRO component dominates the period of the fluctuation is very close to λ_{LRO}. This corresponds to the case where the crystal structure of the domain is still based on that of ordered Ni_4Mo but where new LRO parameters must be used.

The effect of changing the wavelengths of the two components is shown in Fig. 25 for the case where $\epsilon = 1/2$. In this case, Eq. (1) may be approximated by

$$C_p - C_o \approx \cos(\tfrac{1}{2}\Delta k)x_p \cos kx_p$$

where $\Delta k = k_{SRO} - k_{LRO}$ and $k = k_{SRO} \approx k_{LRO}$.

Introducing the exponential form of Eq. (A.6) into Eq. (A.3) the scattered amplitude becomes (ignoring phase factors)

$$\begin{aligned} F(s) = f_o & \frac{\sin \pi N s d}{\sin \pi s d} \\ & + \frac{\gamma}{4} \frac{\sin \pi N [s - \frac{1}{2\pi}(k + \frac{\Delta k}{2})] d}{\sin \pi [s - \frac{1}{2\pi}(k + \frac{\Delta k}{2})] d} \\ & + \frac{\gamma}{4} \frac{\sin \pi N [s - \frac{1}{2\pi}(k - \frac{\Delta k}{2})] d}{\sin \pi [s - \frac{1}{2\pi}(k - \frac{\Delta k}{2})] d} \\ & + \frac{\gamma}{4} \frac{\sin \pi N [s + \frac{1}{2\pi}(k + \frac{\Delta k}{2})] d}{\sin \pi [s + \frac{1}{2\pi}(k + \frac{\Delta k}{2})] d} \\ & + \frac{\gamma}{4} \frac{\sin \pi N [s + \frac{1}{2\pi}(k - \frac{\Delta k}{2})] d}{\sin \pi [s + \frac{1}{2\pi}(k - \frac{\Delta k}{2})] d} \end{aligned} \qquad (A.7)$$

We again obtain matrix reflections at

$$S = ng \qquad (n = 0, \pm 1, \pm 2, \ldots\ldots)$$

and Type I satellites at

$$S = ng \pm \frac{1}{2\pi}\left(k + \frac{\Delta k}{2}\right), \quad (n = 0, \pm 1, \pm 2, \ldots\ldots)$$

and Type II satellites at

$$S = ng \pm \frac{1}{2\pi}\left(k - \frac{\Delta k}{2}\right), \quad (n = 0, \pm 1, \pm 2, \ldots\ldots)$$

Figs. 25a and 25b show the composition profile and corresponding amplitude spectrum for the case when k_{SRO} is fixed and k_{LRO} is reduced by an amount Δk. All the satellites are shifted outward from each matrix reflection by an $\Delta k/2\pi$. The satellites are now centered about former positions of the Type I satellites.

Figs. 25c and 25d show the results of fixing k_{LRO} and allowing k_{SRO} to increase by an amount Δk. All satellites are now shifted inward towards each matrix reflection again by the amount $\Delta k/2\pi$ from their former positions.

In the case where a range of k_{SRO} and k_{LRO} are excited in a local region each component will contribute to the amplitude spectrum resulting in a smearing out of the satellite intensity distribution into streaks. The same effect, however, can occur in the case where different local regions in the crystal having slightly different values of

k_{SRO} and k_{LRO} are scattering independently. Each region will contribute its own reciprocal lattice, hence resulting in streaked satellites. In either case, however an array of domains would result in each such region.

In three dimensions each matrix reflection will be flanked by two sets of satellites all lying in a line parallel to the direction of the composition fluctuation. For the case where fluctuations occur in all ⟨420⟩ directions in various points of the crystal, each matrix reflection will be flanked by 12 pairs of satellites. All the Type II satellites will result in the reciprocal lattice shown in Fig. 3. All the Type I satellites will result in SRO peaks at all equivalent $1\frac{1}{2}0$ positions in the fcc reciprocal lattice. During the early stages of ordering when the satellites are streaked, the resulting [002] pattern will be that shown schematically in Fig. 21b.

Referring again to Fig. 3, each $1\frac{1}{2}0$ position is surrounded by 4 superlattice spots. During the initial stages of ordering each superlattice spot will be a Type II satellite each contributing a Type I satellite to the $1\frac{1}{2}0$ position. Hence, the resulting intensity of the $1\frac{1}{2}0$ SRO maxima will be 4 times as great as the value one would predict from our one dimensional model.

FIGURE CAPTIONS

Fig. 1 Ni-Mo phase diagram.

Fig. 2 Plan view of atomic packing in the (002) planes of the ordered Ni_4Mo structure.

a. Type I ordering scheme results in the bct unit cell rotated counter-clockwise relative to the fcc unit cell.

b. Type II ordering scheme showing the clockwise rotation of the bct unit cell.

Fig. 3 The intensity distribution in reciprocal space for the ordered Ni_4Mo structure ($D1_a$). The large circles represent matrix reflections. The small circles represent superlattice reflections from the 6 $D1_a$ orientational variants.

Fig. 4 a. [002] diffraction pattern; superlattice reflections are from two ordered domains in antiparallel twin orientation. (c-axes at 180°)

b. [121] diffraction pattern showing reflections from two domains perpendicular twin orientation. (c-axes at 90°).

c. Schematic view showing that in a $[1\bar{3}0]$ foil orientation only superlattice reflections of a single orientational variant will lie on the reflecting sphere.

Fig. 5 A schematic representation of a small Type II domain "nucleated" within a Type I domain by chance composition fluctuation normal to the (420) or (240) planes of the fcc lattice.

Fig. 6 Diffraction patterns of an alloy held at 1100°C for 3 hours prior to quenching into iced brine.

a. [002],)
b. [121],) reciprocal lattice sections
c. [$\bar{1}$30].)

Note the weak satellites near superlattice reflections indcated by arrows in b. and c. are not detectable in a.

Fig. 7 Microphotometer trace along [4$\bar{2}$0] directions obtained from the original plate of the [121] diffraction pattern shown in Fig. 6b. Note peaks near $2\bar{2}0_{bct}$ and $3\bar{3}0_{bct}$ superlattice positions are easily detectable while those near $1\bar{1}0_{bct}$ and $4\bar{4}0_{bct}$ are obscured by neighboring $1\frac{1}{2}0$ SRO spots.

Fig. 8 Typical microstructure of as-quenched alloys the $1\bar{1}1$ obtained from a $[121]_{fcc}$ foil.

a. Bright field using fundamental reflection.
b. Dark field using the $1\frac{1}{2}0$ SRO spot.

Fig. 9 Typical microstructure in alloys aged 5 mintes at 750°C.

a. [121] diffraction pattern

b. Dark field image of a $1\bar{1}0_{bct}$ superlattice reflection showing ordered domains of a single orientational variant.

Bright field images using fundamental reflections showing strain contrast due to finely dispersed strain centers.

c. $g = (002)_{fcc}$

d. $g = (1\bar{1}1)_{fcc}$

e. $g = (\bar{1}11)_{fcc}$

f. $g = (\bar{2}20)_{fcc}$

Foil orientation is near $[110]_{fcc}$.

Fig. 10 a. [121] diffraction pattern from an alloy aged 10 seconds at 750°C. The weak regularly spaced spots aligned along the $[1\bar{1}1]$ and $[20\bar{2}]$ directions are double diffraction spots originating from domain boundaries. Their presence indicate domains are in contact.

b. Dark field image using a $1\bar{1}0_{bct}$ superlattice reflection showing only one set of domains.

Fig. 11 Typical microstructure of an alloy aged 1 hour at 750°C. The domain structure consists of an

assembly of transformation twins. Foil orientation is near $[121]_{fcc}$.

a. Bright field image using the $(1\bar{1}1)_{fcc}$ fundamental reflection. b., c. and d. are dark field images using superlattice reflections indicated by 2, 4 and 3, respectively in Fig. 3 and Fig. 4.

Fig. 12 Electron diffraction patterns from alloys aged at 650°C, showing diffuse satellite intensity distribution.

a. $[121]_{fcc}$ pattern)
b. $[002]_{fcc}$ pattern) after 5 minutes of aging

c. $[121]_{fcc}$ pattern)
d. $[002]_{fcc}$ pattern) after 10 minutes of aging

Fig. 13 A schematic representation of the satellite intensity distribution about each $1\frac{1}{2}0$ SRO spot, which form during the first 10 minutes of aging at 650°C.

Fig. 14 Typical microstructure of alloys aged at 650°C. Foil orientation is $[121]_{fcc}$.

a. Bright field $g = (1\bar{1}1)_{fcc}$)
b. Dark field using $1\frac{1}{2}0$ SRO spot) 5 minutes

c. Bright field $g = (1\bar{1}1)_{fcc}$)
d. Dark field using $1\frac{1}{2}0$ SRO spot) 10 minutes

Fig. 15 The (002) stereogram showing the symmetry of the Type I structure and its orientational relationship relative to the fcc lattice. The crosses indicate fcc poles of the form 420 .

Fig. 16 A field ion micrograph of fully ordered Ni_4Mo after aging for 125 hours at 750°C. Note the prominence of the $(1\bar{1}0)_{bct}$ plane.

Fig. 17 Field evaporation sequence of an alloy aged 1 hour at 750°C. a. - b. shows the emergence of a domain with a large prominent plane centered on the [204] fcc pole. c. shows the domain boundaries themselves.

Fig. 18 A field ion micrograph of an alloy aged 10 seconds at 250°C showing large prominent planes at the [204] and [$\bar{2}$04] fcc poles.

Fig. 19 Field ion micrographs showing preferential clustering of well defined planes about fcc poles of the form <420> in alloys aged at 650°C.

a. An alloy aged for 10 minutes.

b. An alloy aged for 5 minutes. Arrows indicate well defined planes at <420> fcc poles.

c. Same as b. after application of a single pulse of height 1.5 kv and width of 20μs. Note that the well defined plane in the [02$\bar{4}$] region in b. has been removed.

Fig. 20 Field ion micrographs of as-quenched alloys. a.-b. shows microstructure when liquid helium is used as specimen coolant. Notice that the perfection of the ring pattern of the [002] pole is much higher in 20a. than in 20b. Note also the interfaces marked by arrows. c. Field ion micrograph of as-quenched alloy when liquid nitrogen is used as specimen coolant. Clustering of well-defined planes about the $\langle 420 \rangle_{fcc}$ poles is again observed.

Fig. 21 Schematic view of <002> diffraction patterns. a. Illustrates the type of streaking expected from domains having a plate-like shape. b. Schematic representation of the type of streaking observed in actual patterns in alloys aged at 650°C. c. Schematic representation of the [002] diffraction patterns from 4 distinct structures. Fig. 21b. is a composite of all 4 diffraction patterns. The dashed unit cell corresponds to a structure generated by composition waves with a wavelength equal to $4d_{420}$.

Fig. 22 A schematic representation of various states of LRO in terms of composition waves. b. $S = 1$, c. $S < 1$ and d. represents a state of order

requiring two LRO parameters.

Fig. 23 Deleted.

Fig. 24 Shows the effect of changing the amplitude of the SRO and LRO components on the composition profile and on their corresponding satellite scattered amplitude spectrum.

a. $\epsilon = 1/3$

b. $\epsilon = 1/2$

c. $\epsilon = 2/3$

Fig. 25 Shows the effect of changing the wavelengths of the SRO and LRO components on the composition profile and on the satellite scattered amplitude spectrum for the case $\epsilon = 0.5$.

a. $\lambda_{SRO} = 4d$, $\lambda_{LRO} = 4.5d$

b. $\lambda_{SRO} = 4.5d$, $\lambda_{LRO} = 5d$.

Fig. 26 A contour plot in the $h_3 = 0$ plane of the function $C(h_1 h_2 h_3)$ for the fcc lattice.

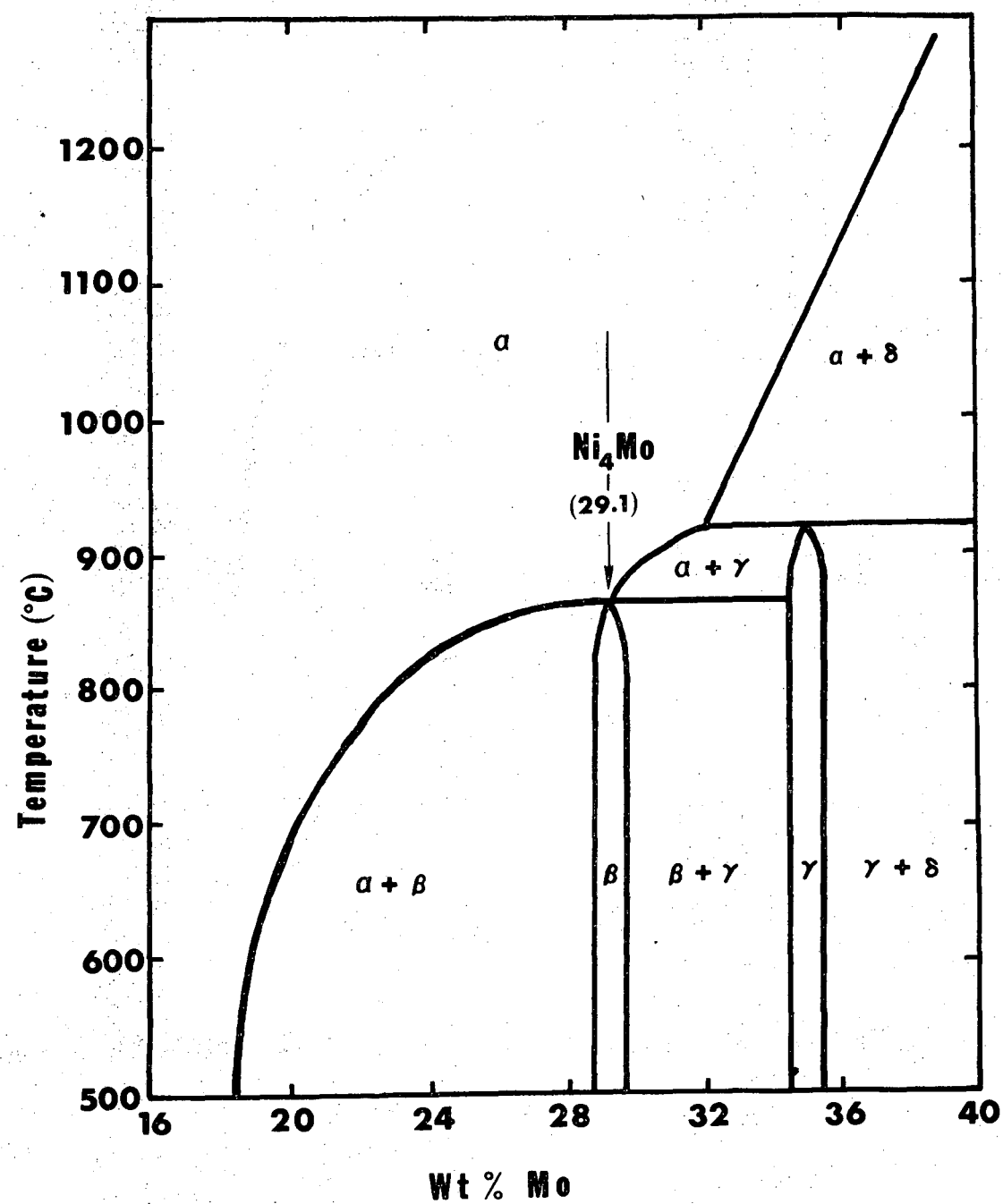

XBL 6911-6608

Figure 1

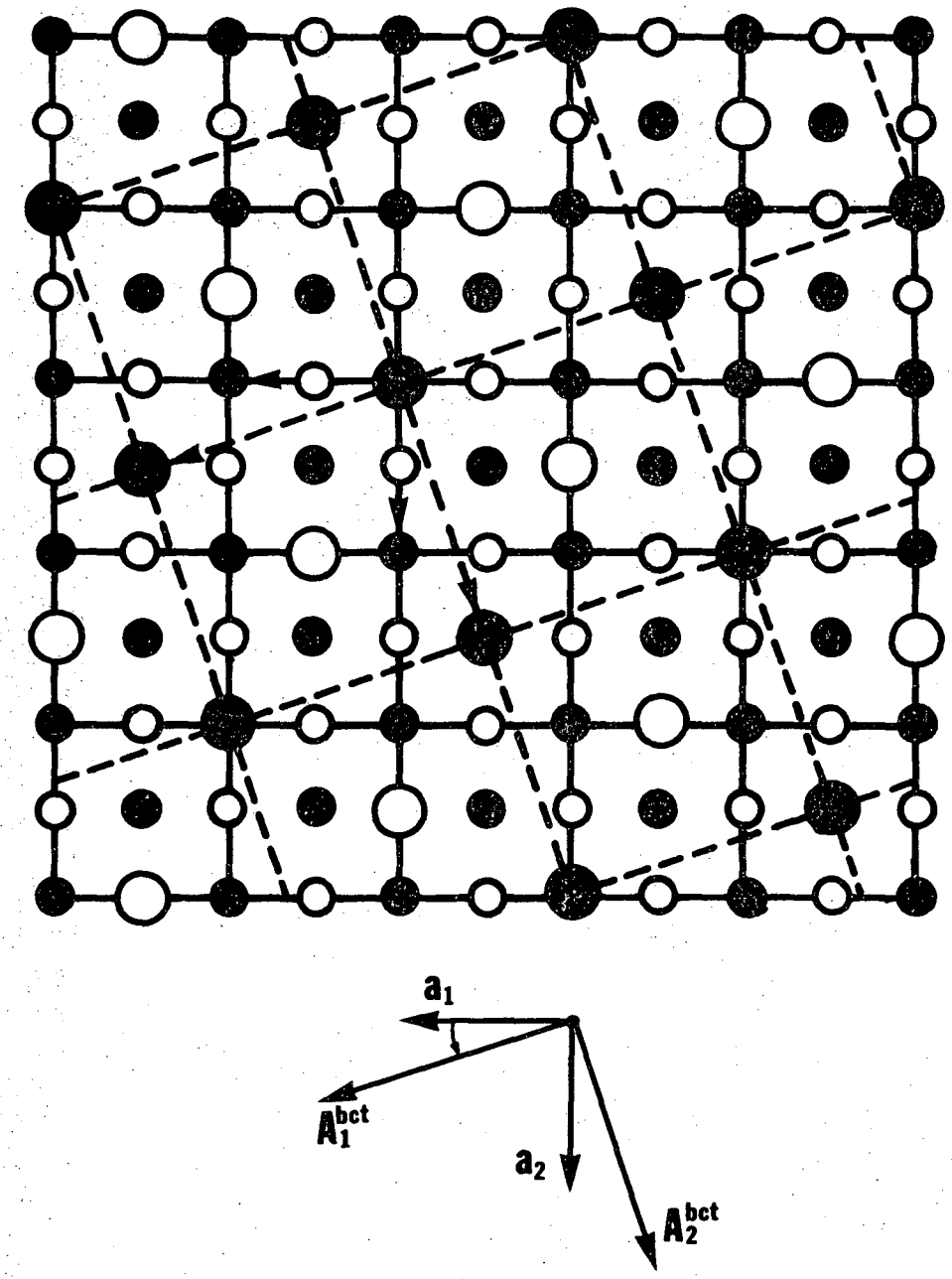

XBL 6911-6607

Figure 2a

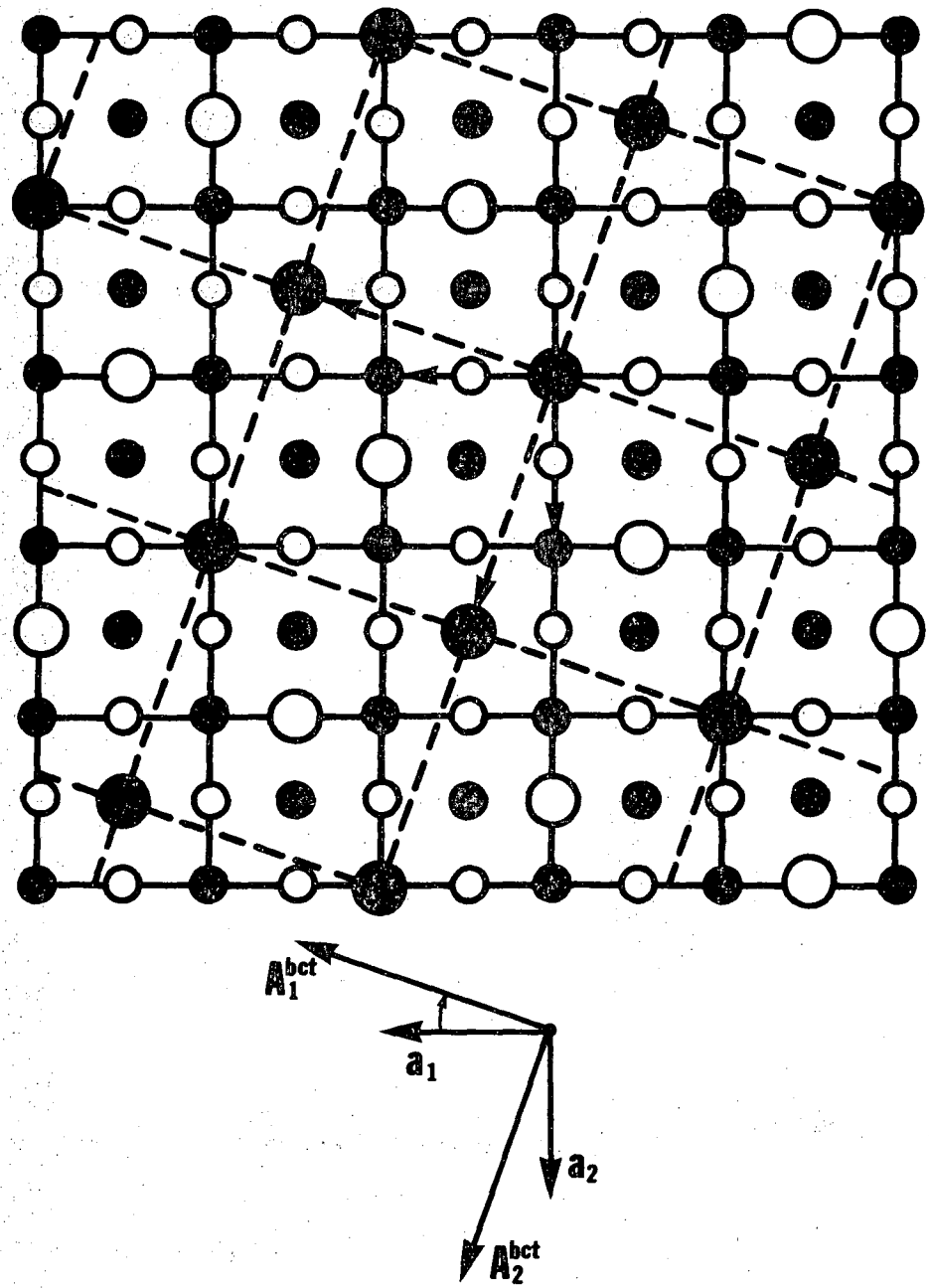

XBL 6911-6609

Figure 2b

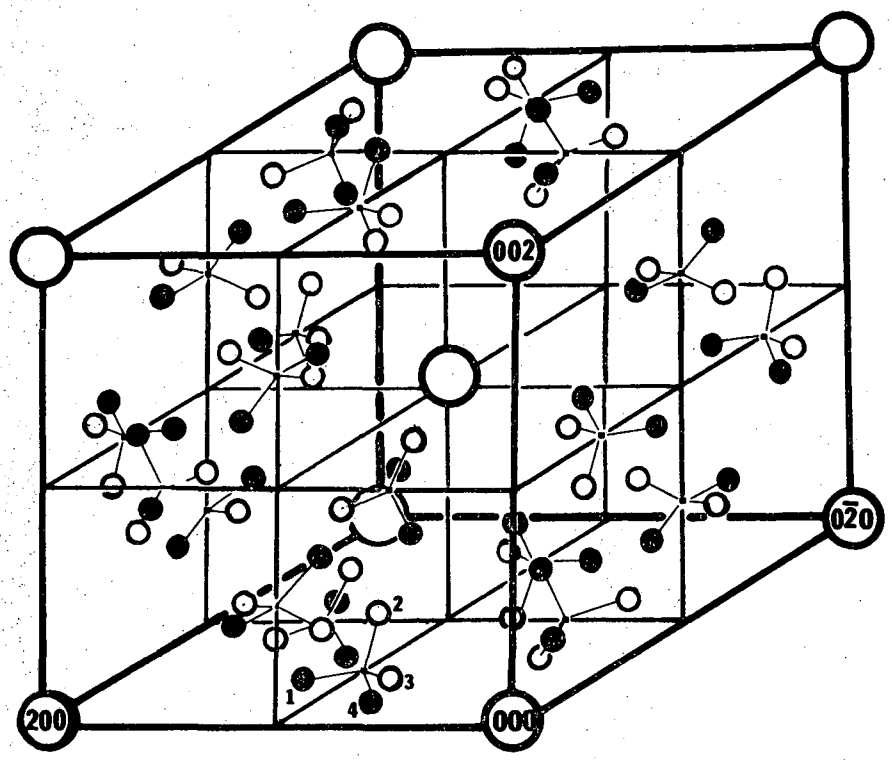

XBL 6911-6610

Figure 3

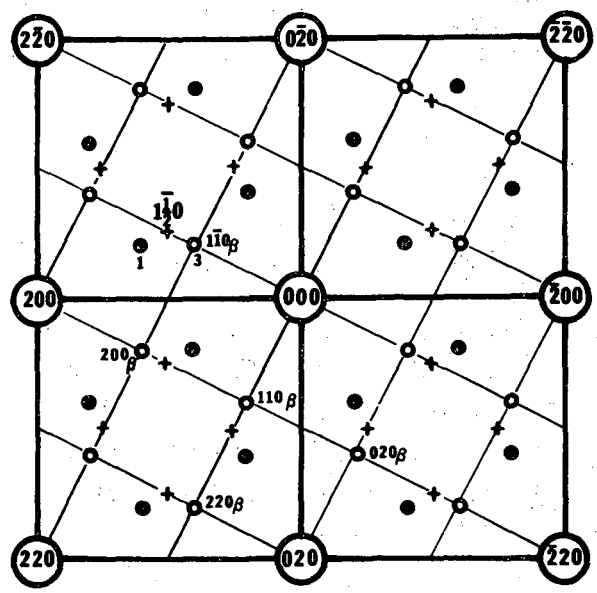

Figure 4a

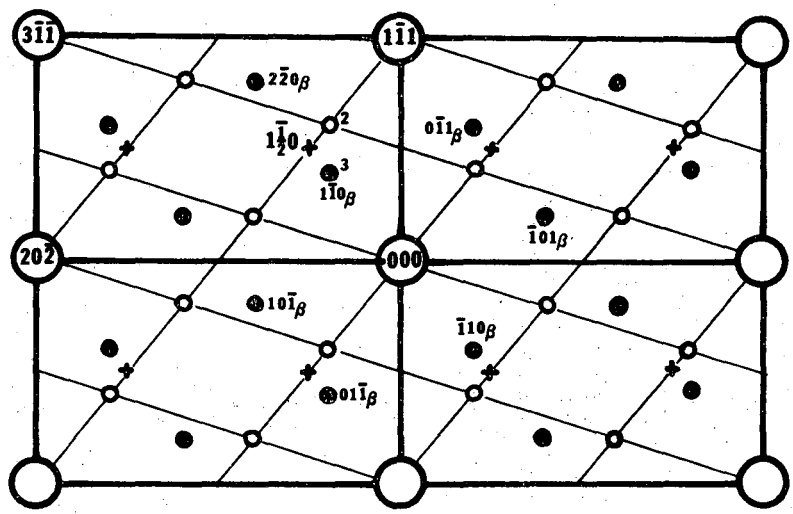

XBL 6911-6606

Figure 4b

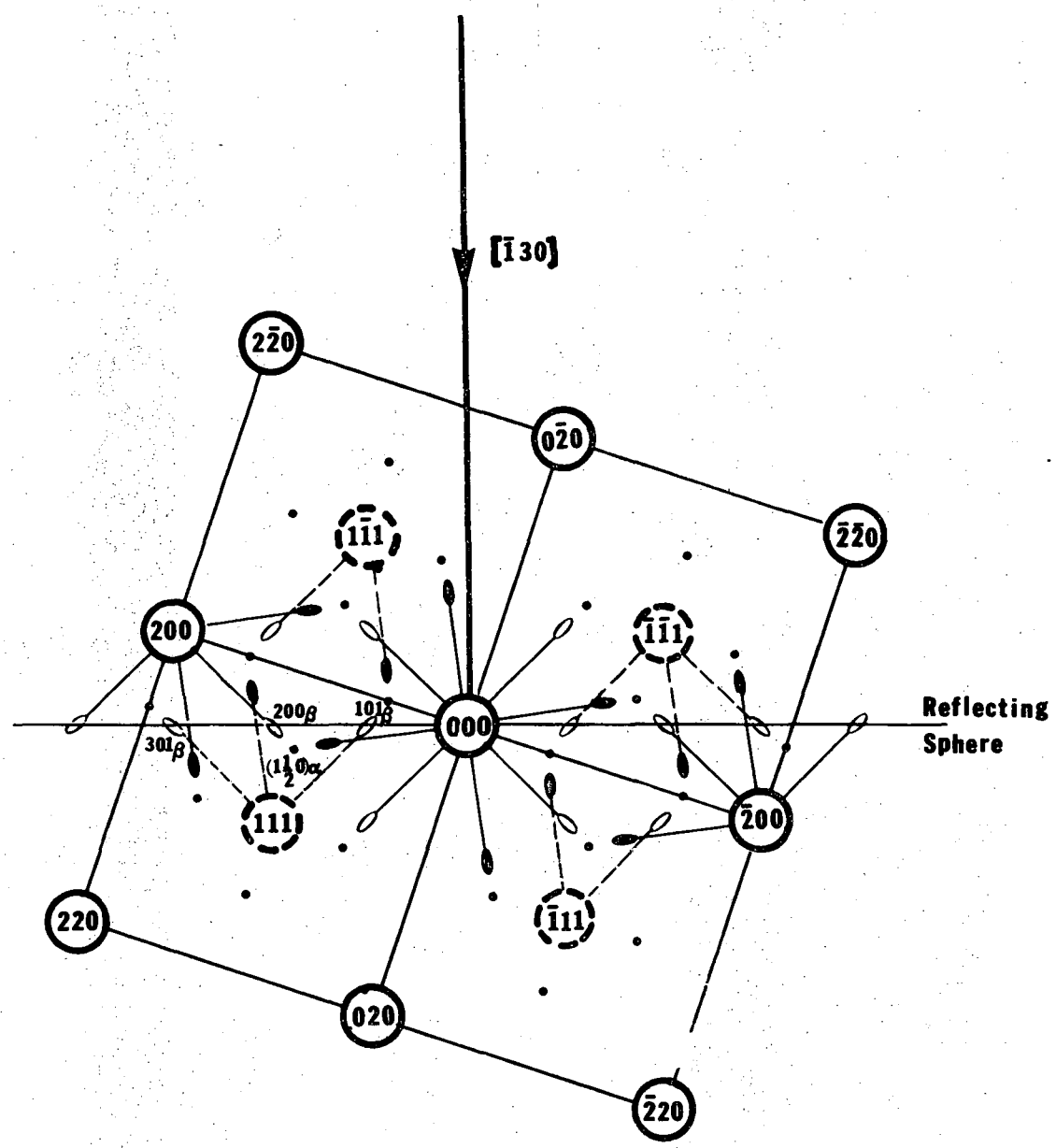

XBL 6911-6605

Figure 4c

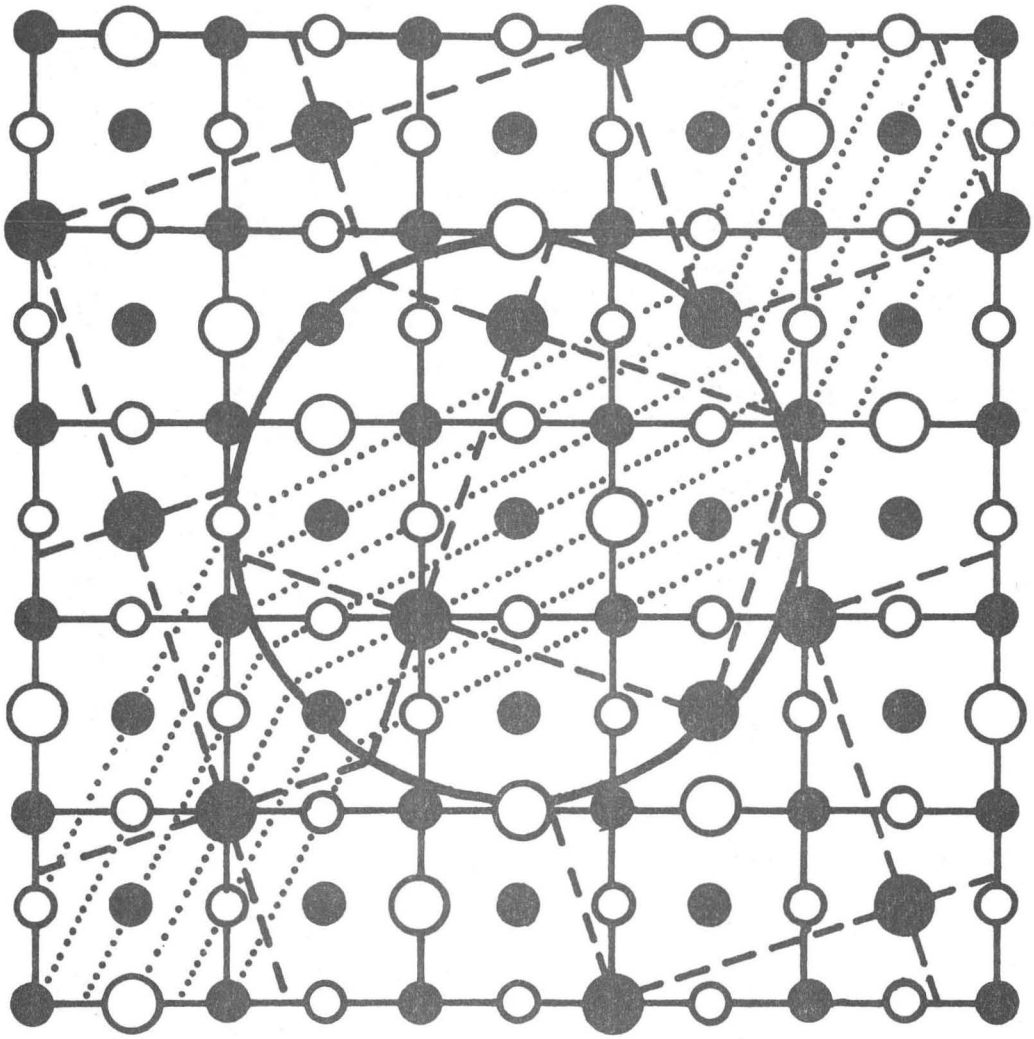

XBL 6911-6604

Figure 5

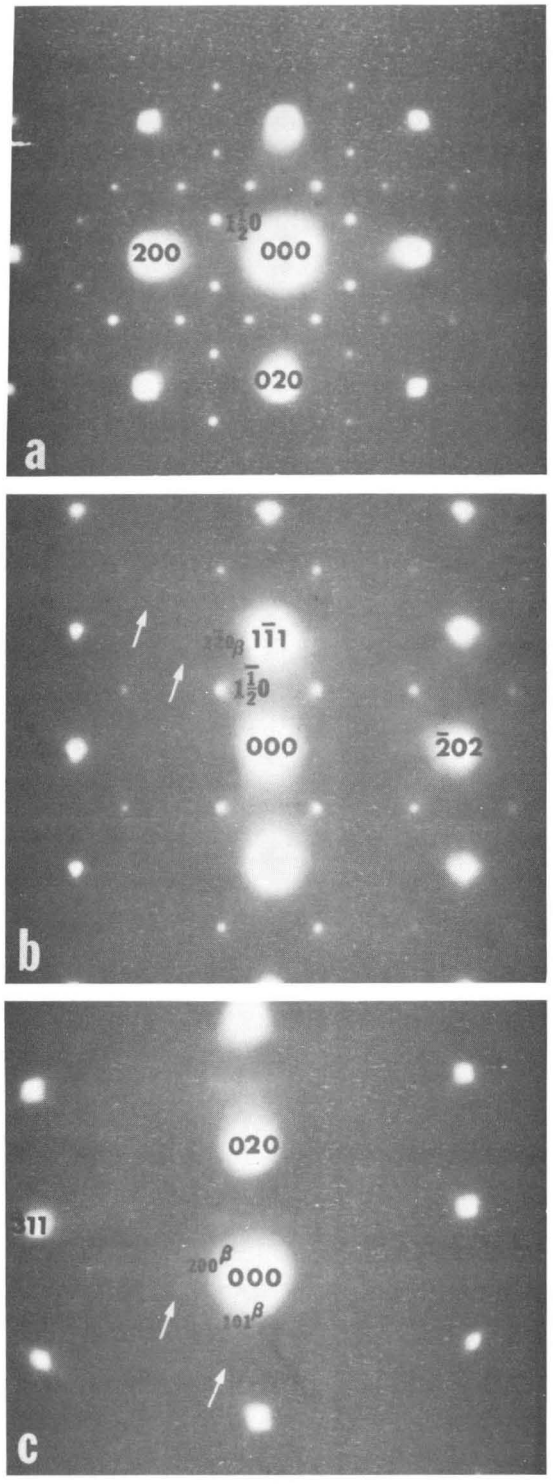

XBB 6911-7492

Figure 6

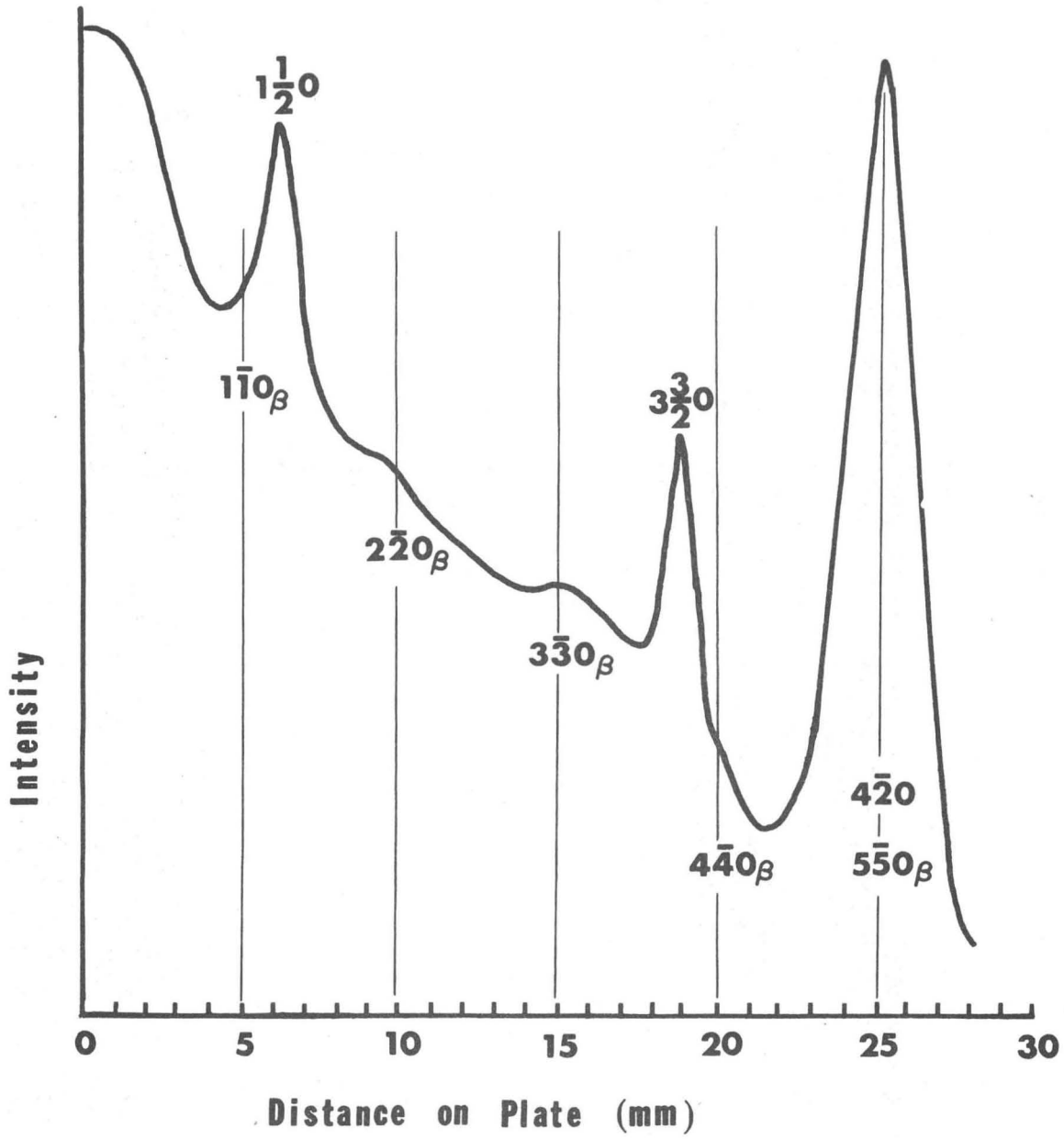

XBL 6911-6602

Figure 7

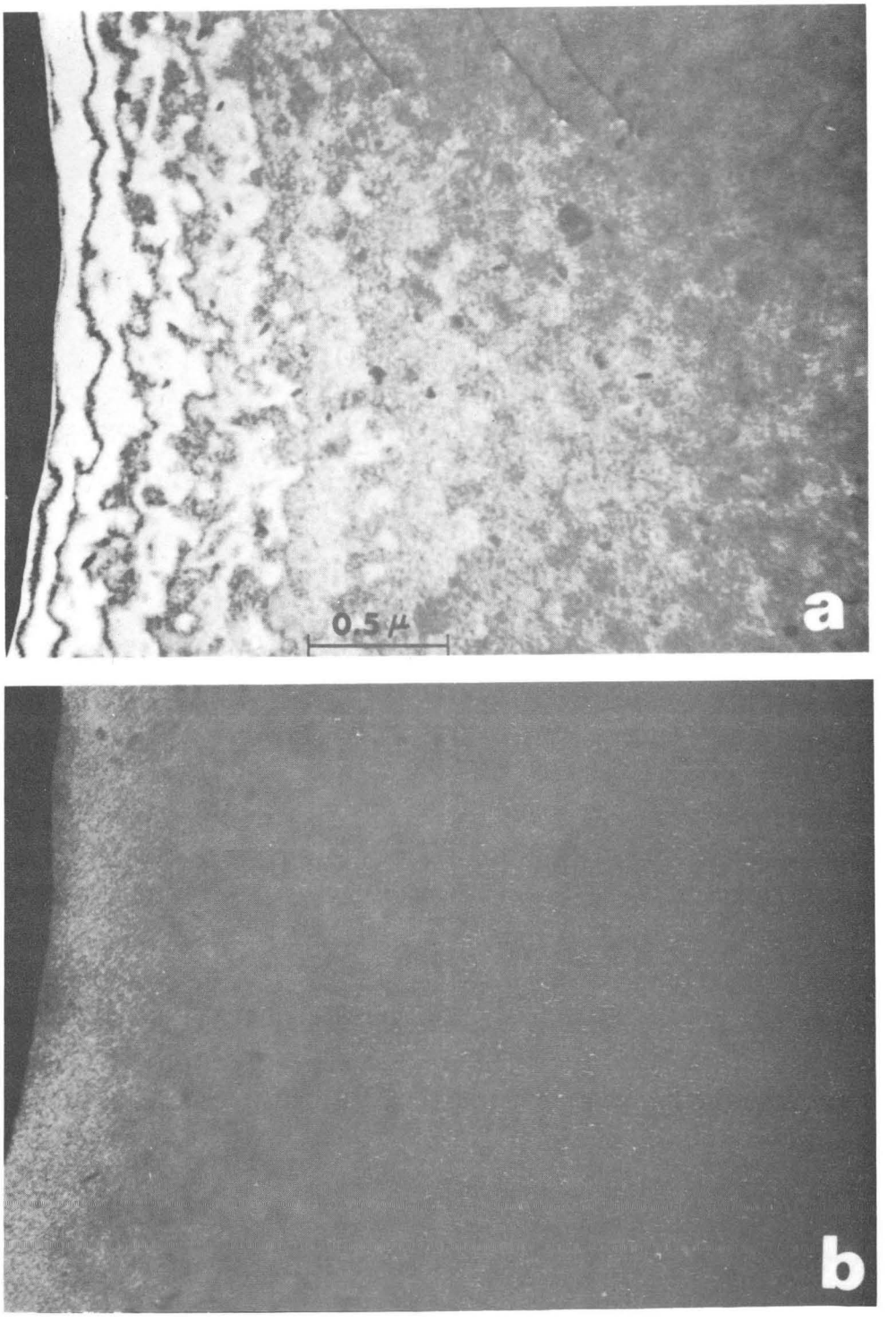

XBB 6911-7494

Figure 8

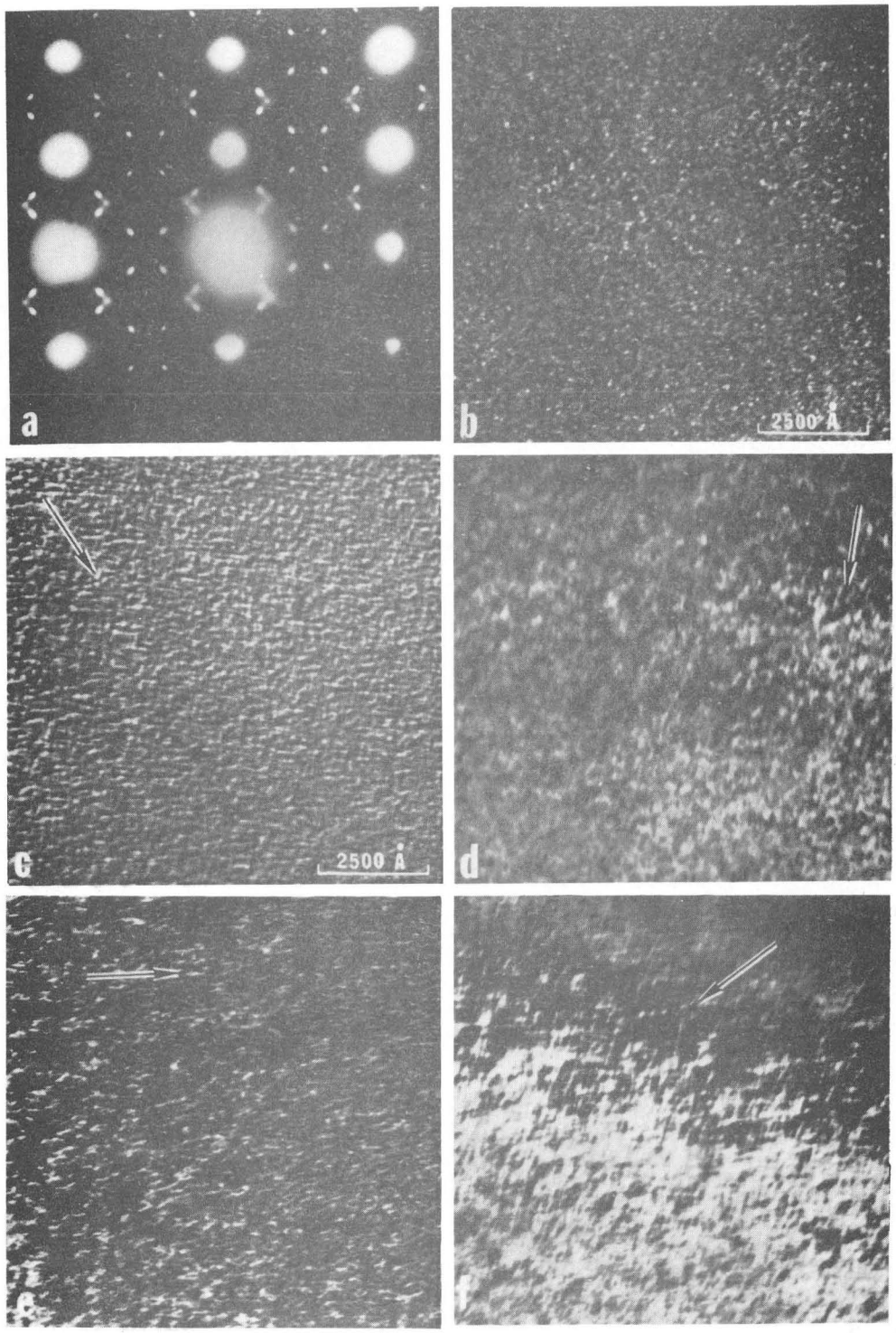

XBB 6911-7496

Figure 9

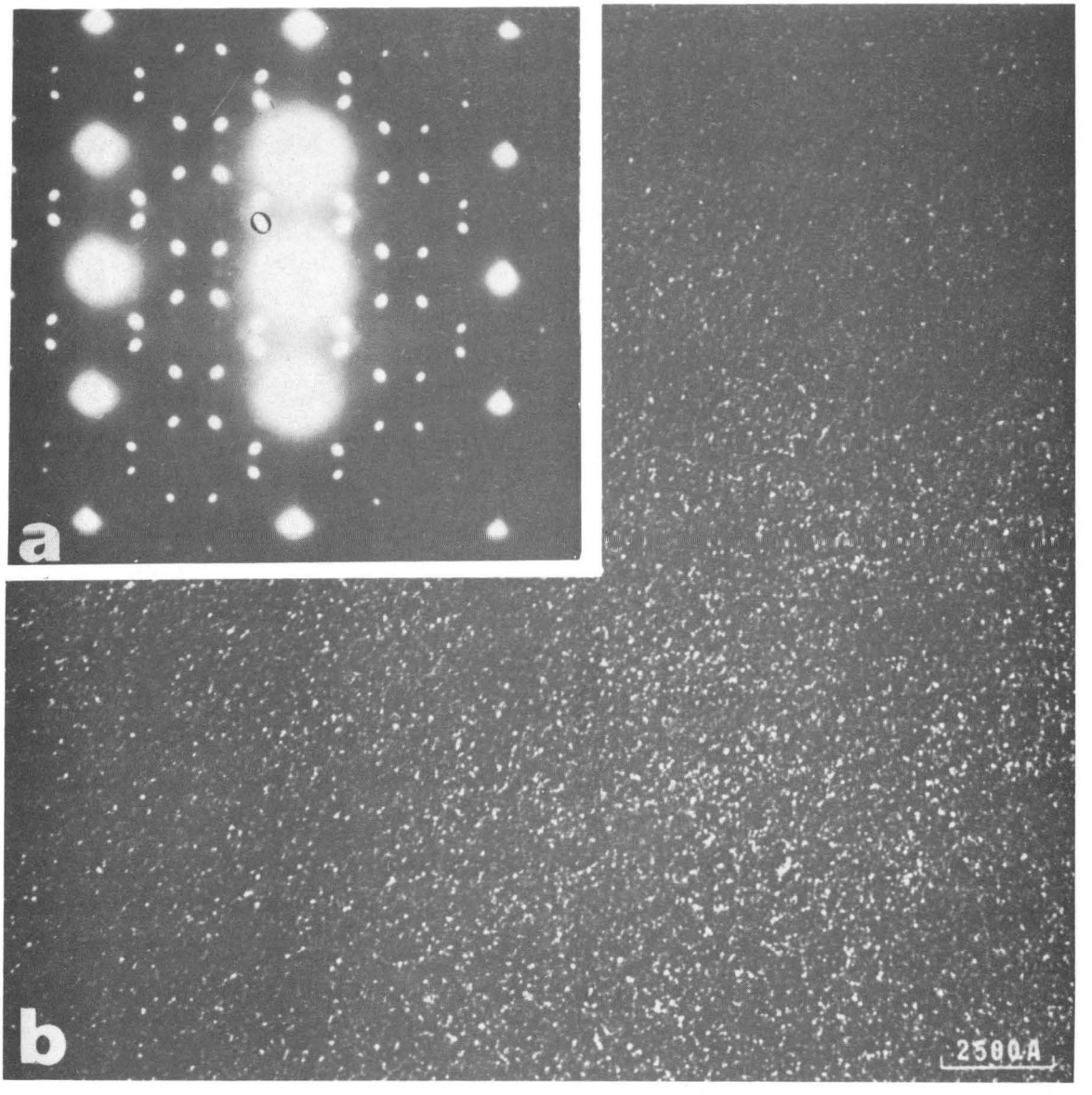

XBB 6911-7490

Figure 10

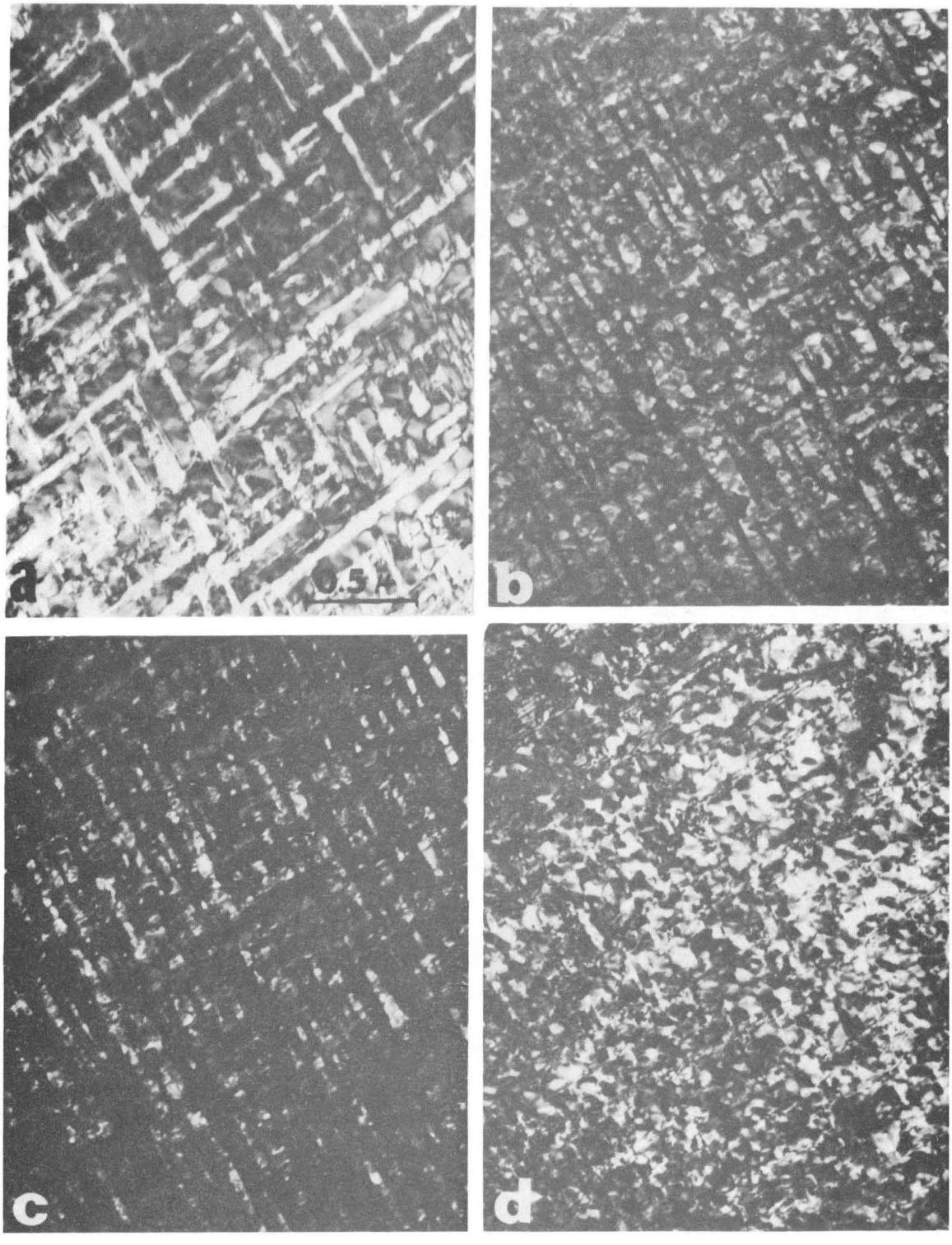

XBB 6911-7491

Figure 11

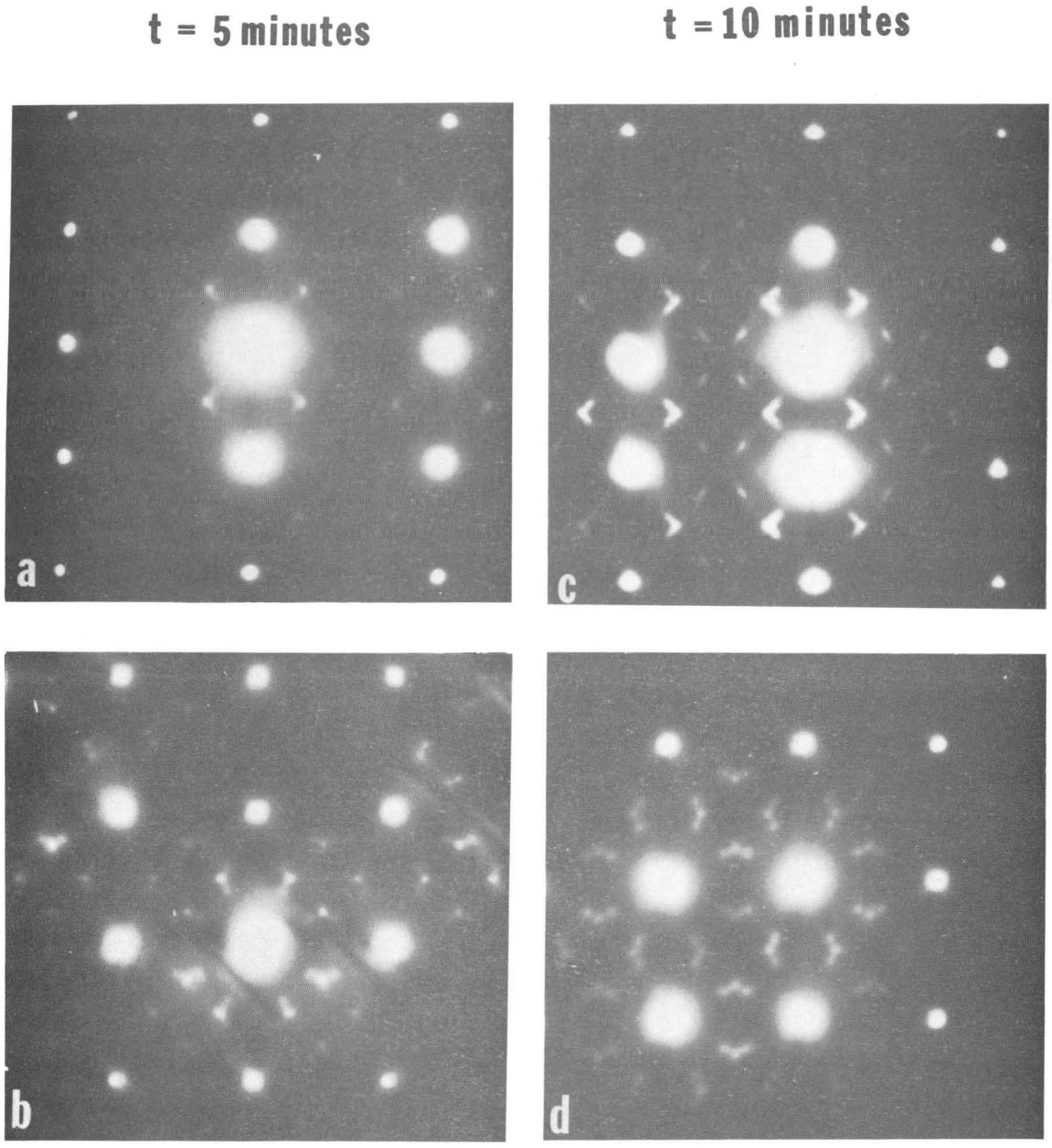

XBB 6911-7493

Figure 12

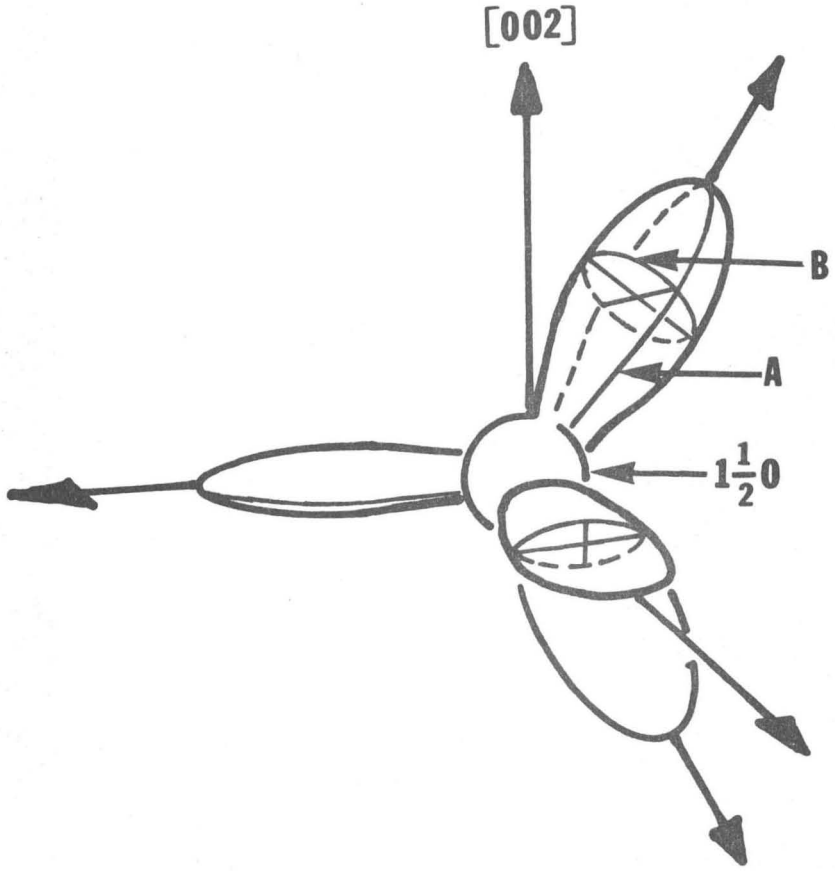

XBL 6911-6603

Figure 13

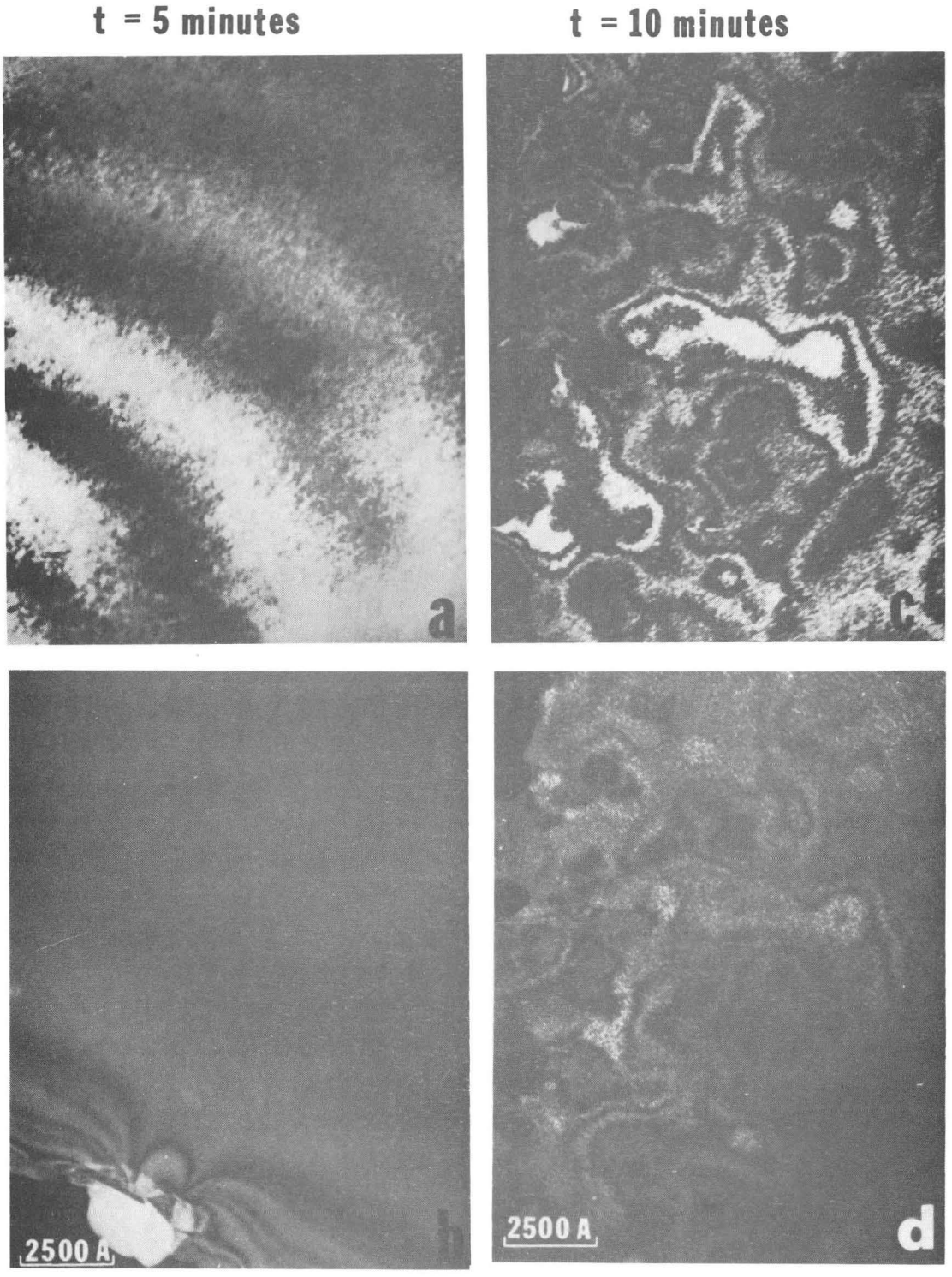

XBB 6911-7495

Figure 14

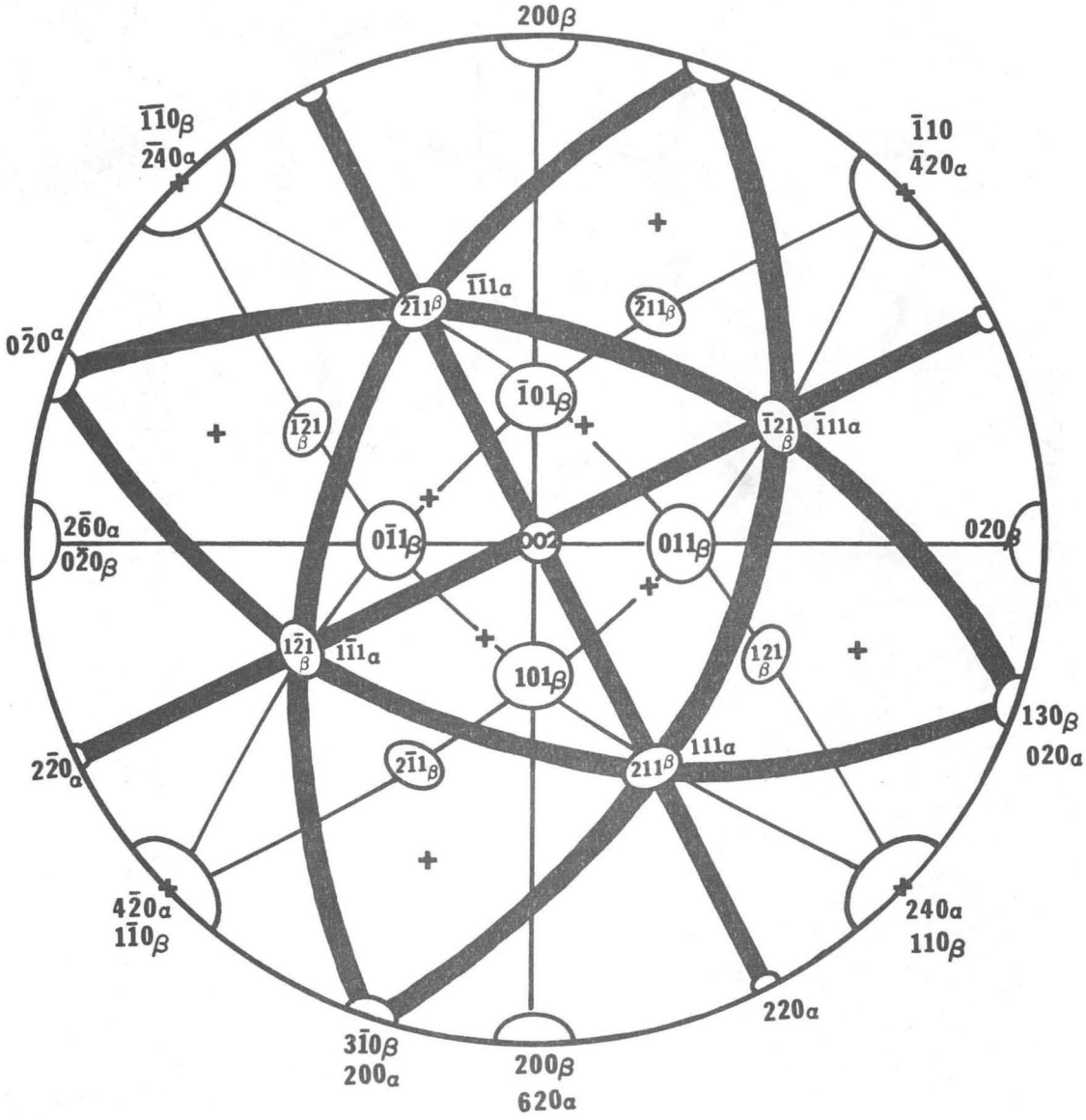

XBL 6911-6601

Figure 15

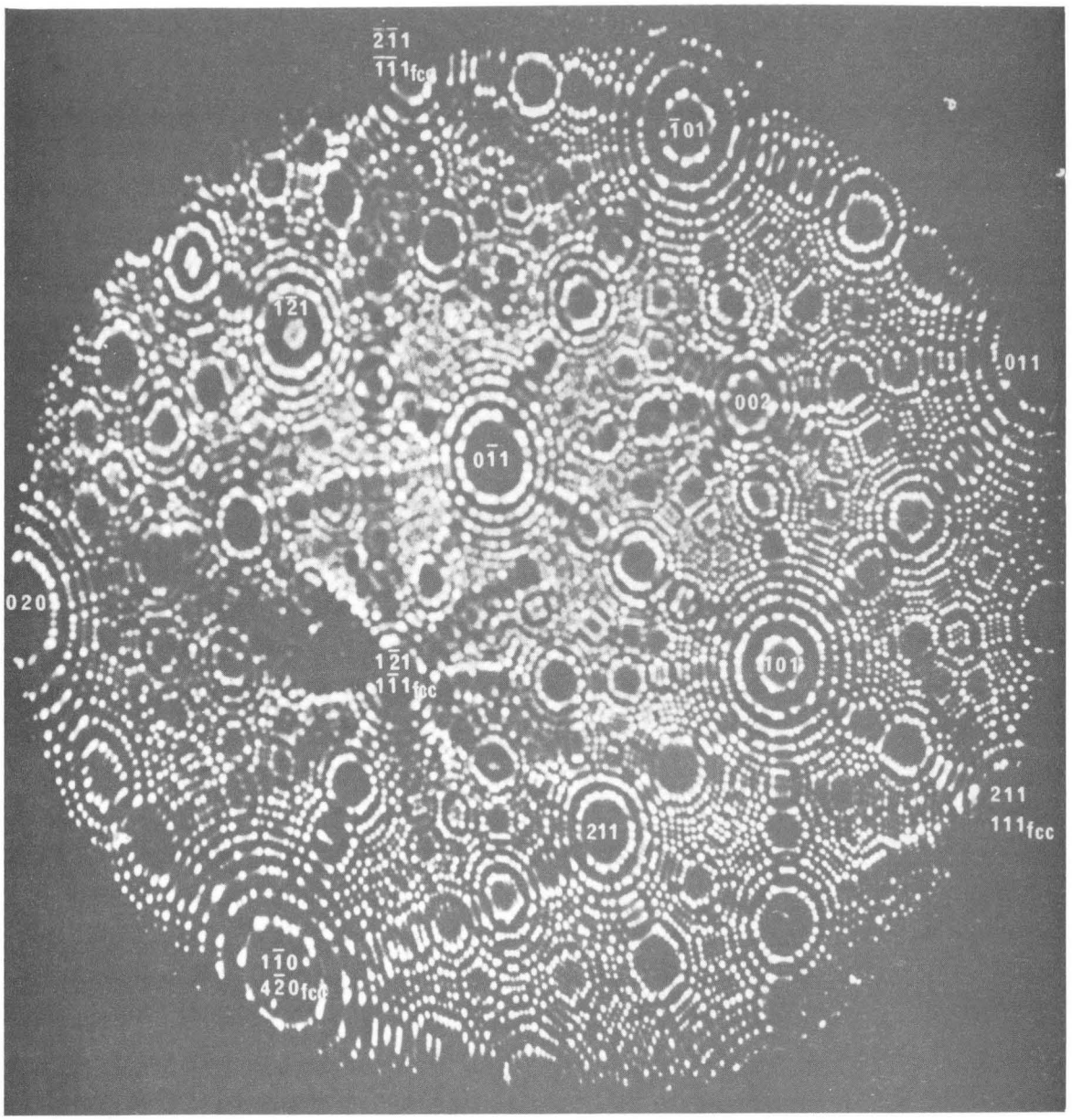

XBB 6911-7498

Figure 16

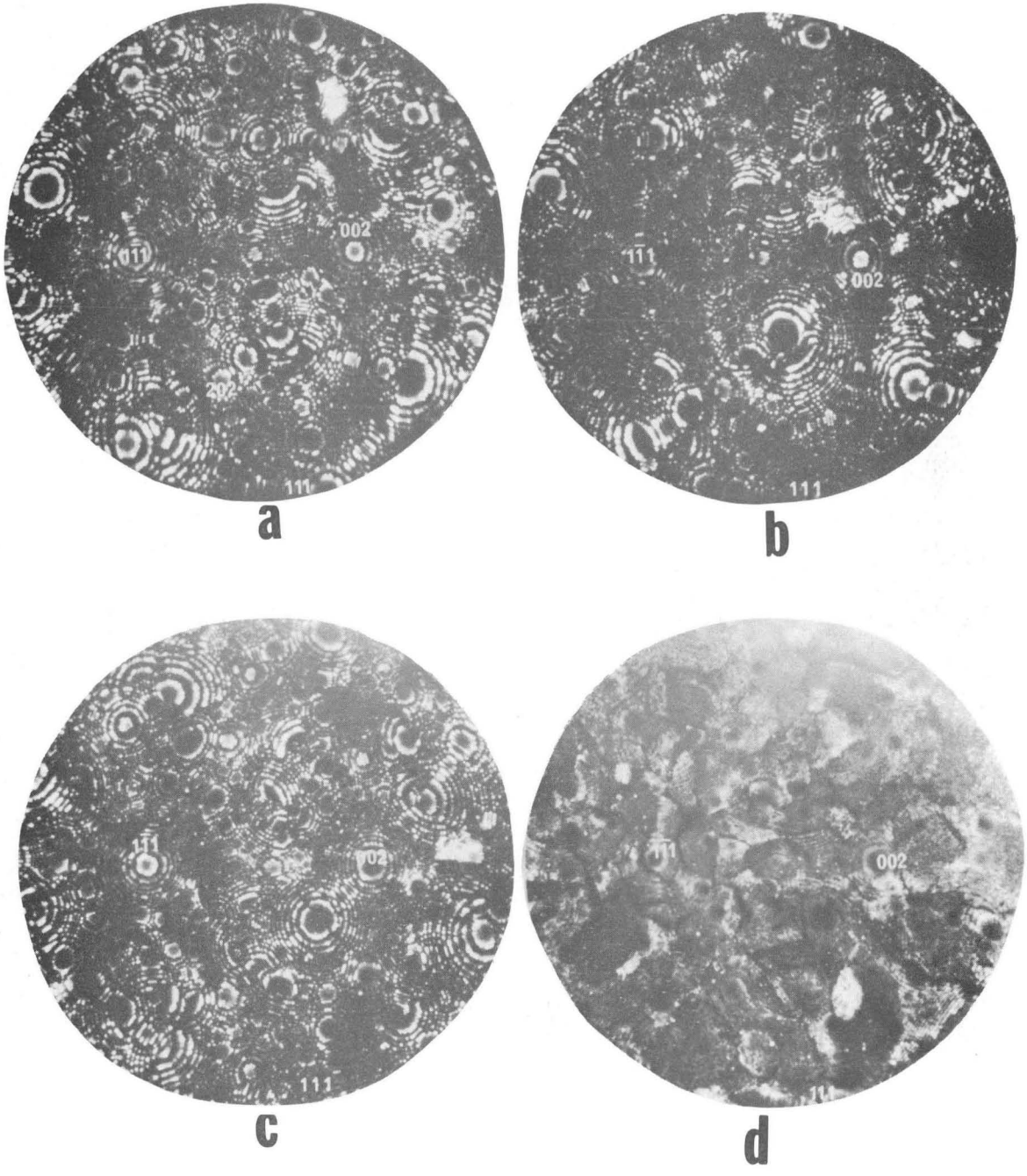

XBB 6911-7497

Figure 17

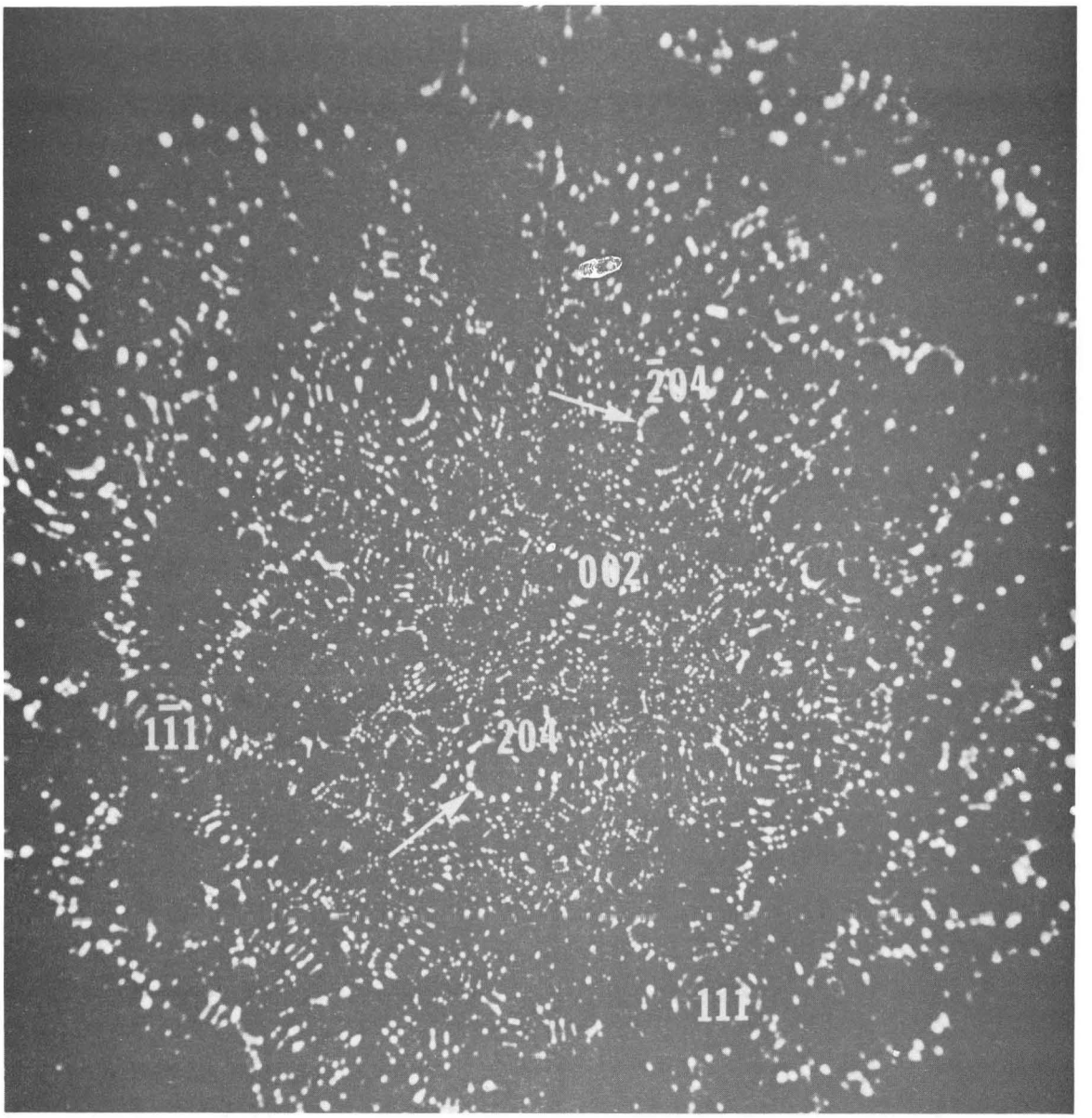

XBB 6911-7500

Figure 18

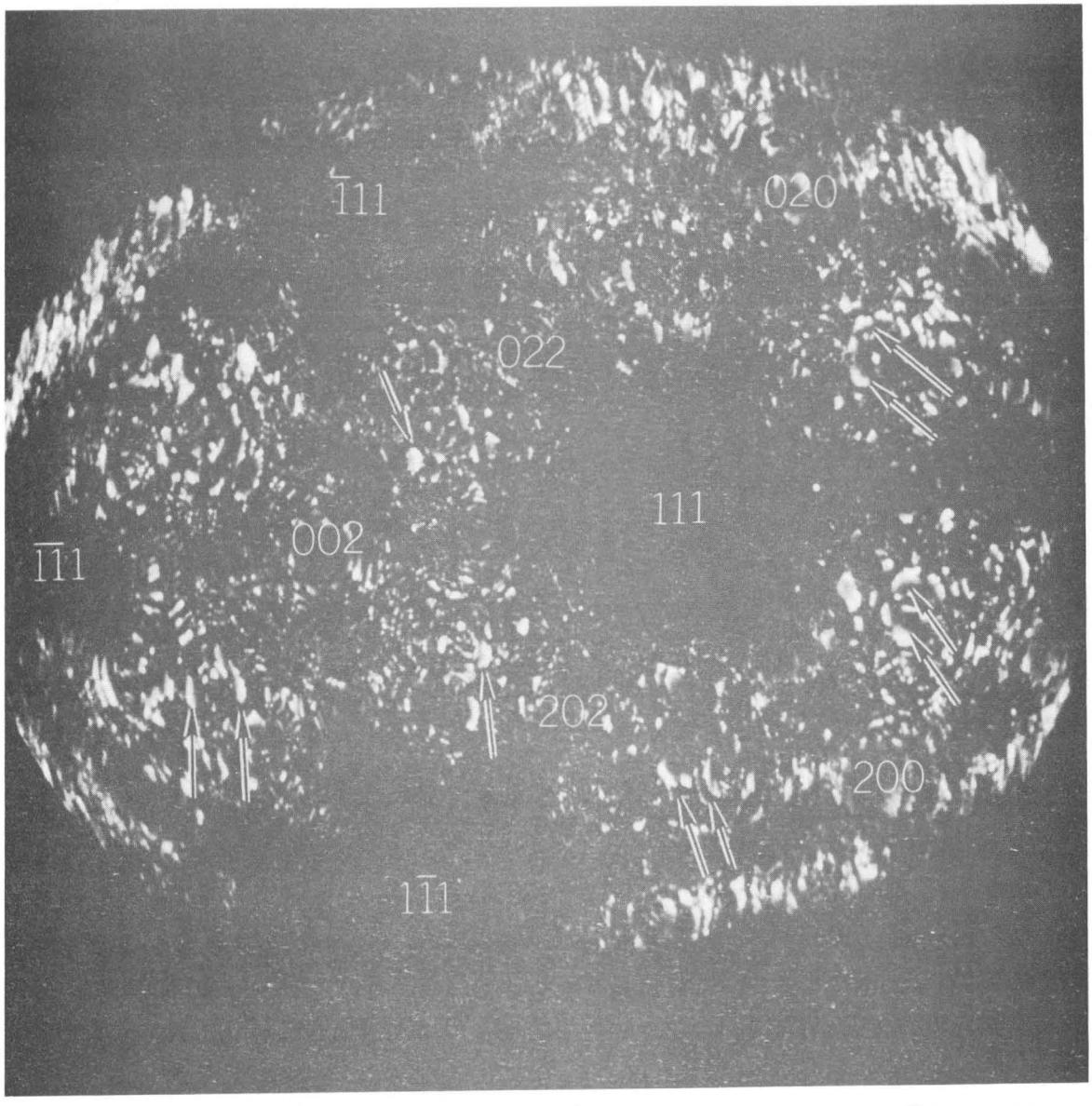

XBB 6911-7505

Figure 19a

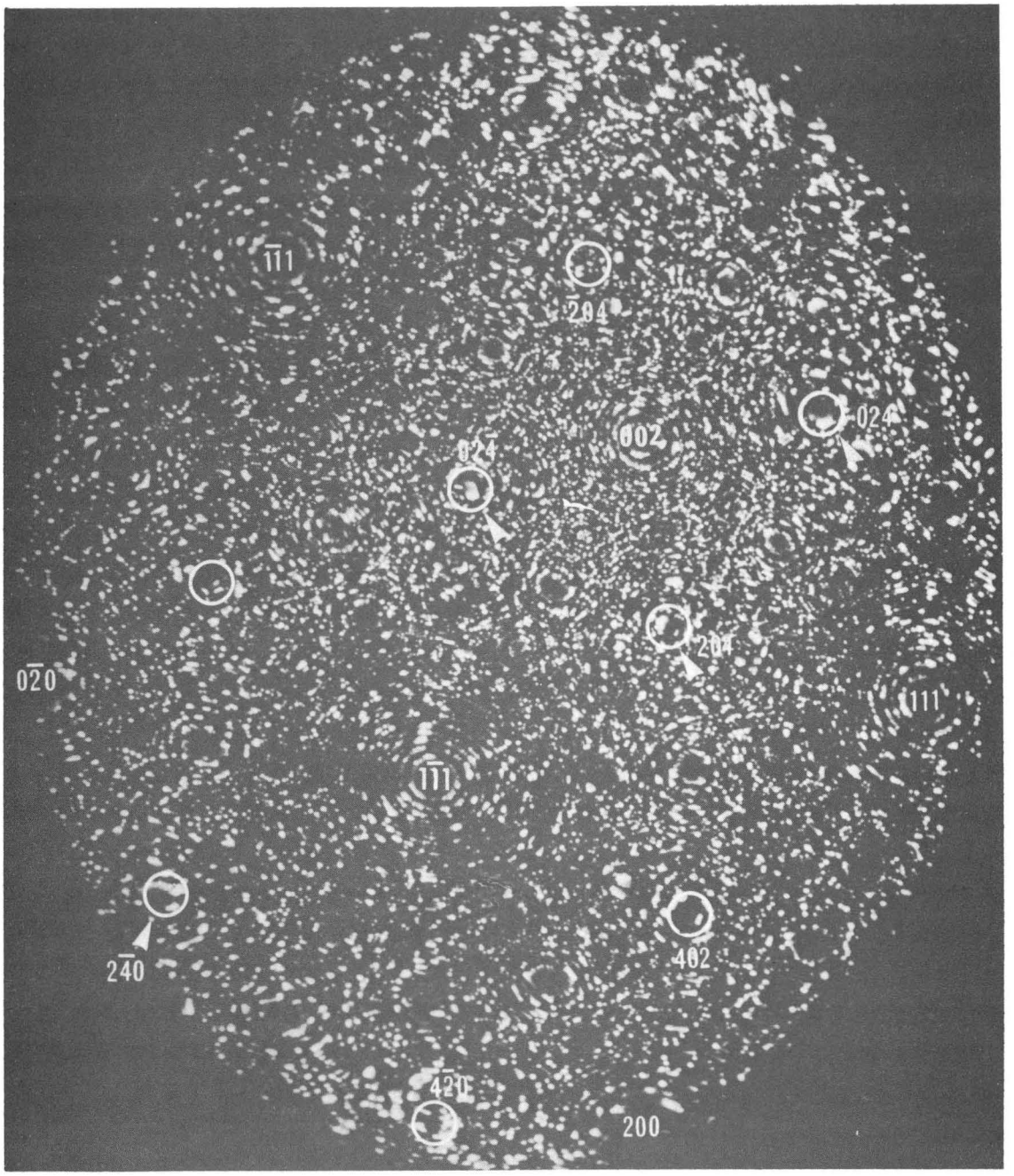

XBB 6911-7504

Figure 19b

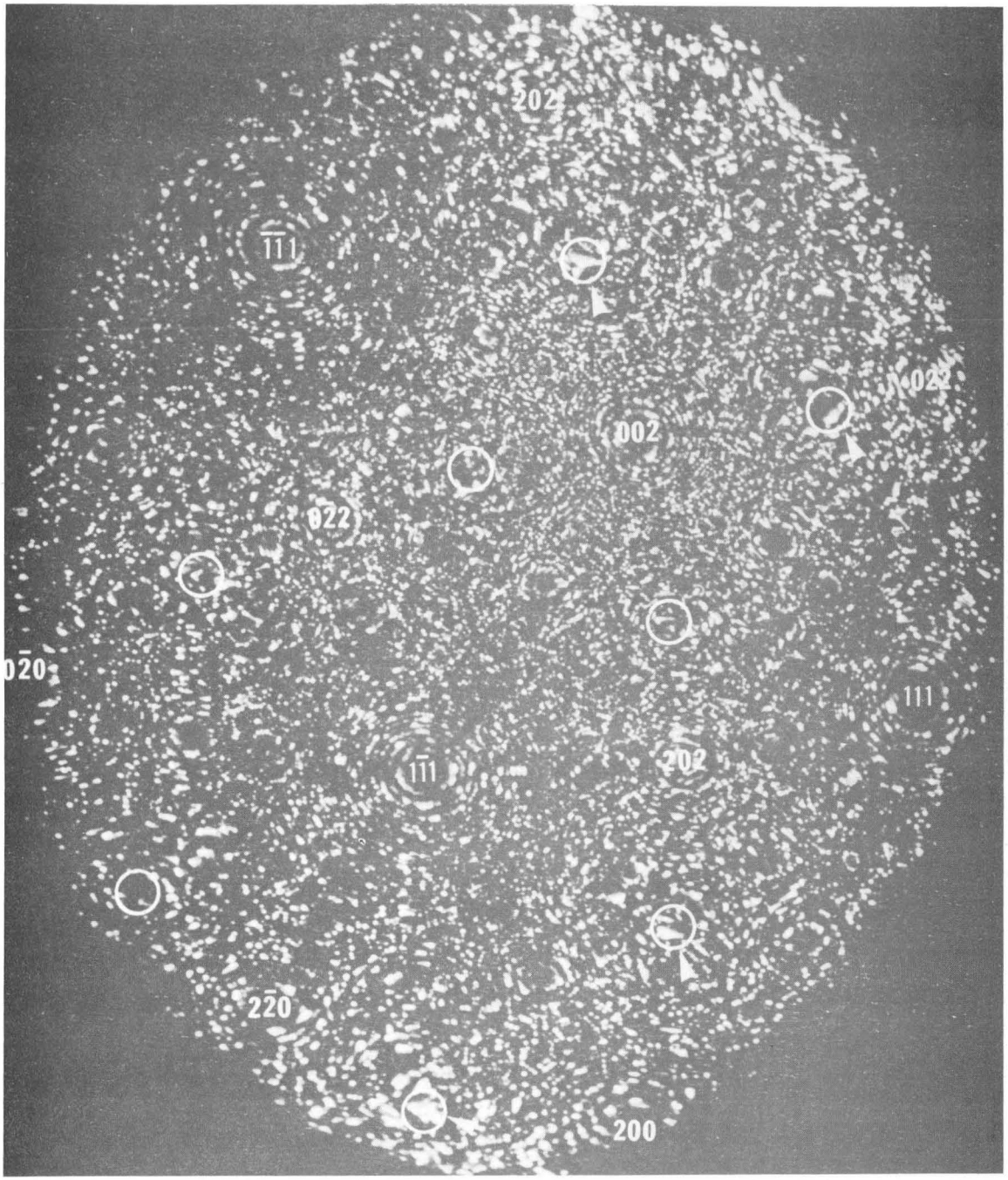

XBB 6911-7502

Figure 19c

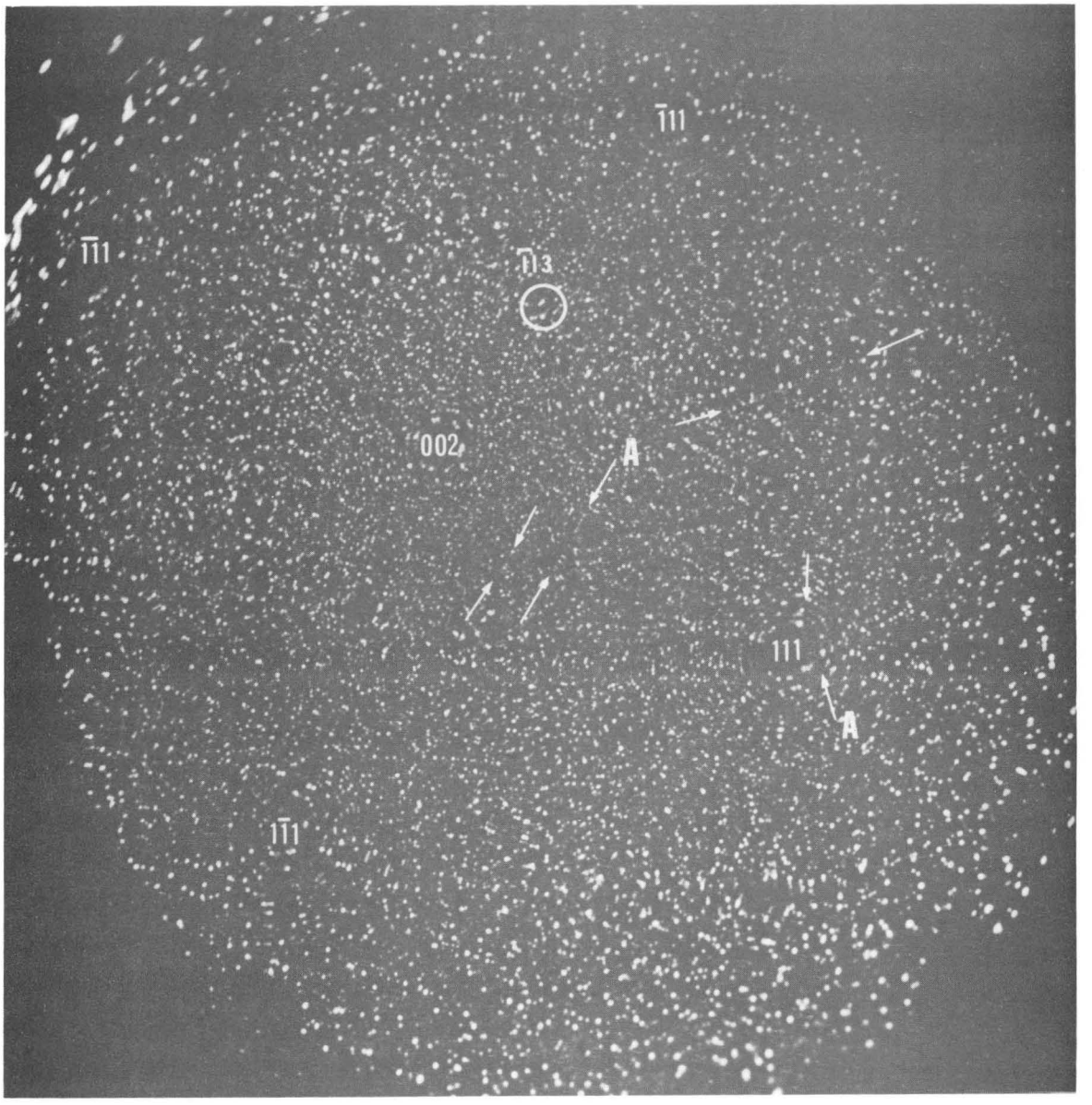

XBB 6911-7503

Figure 20a

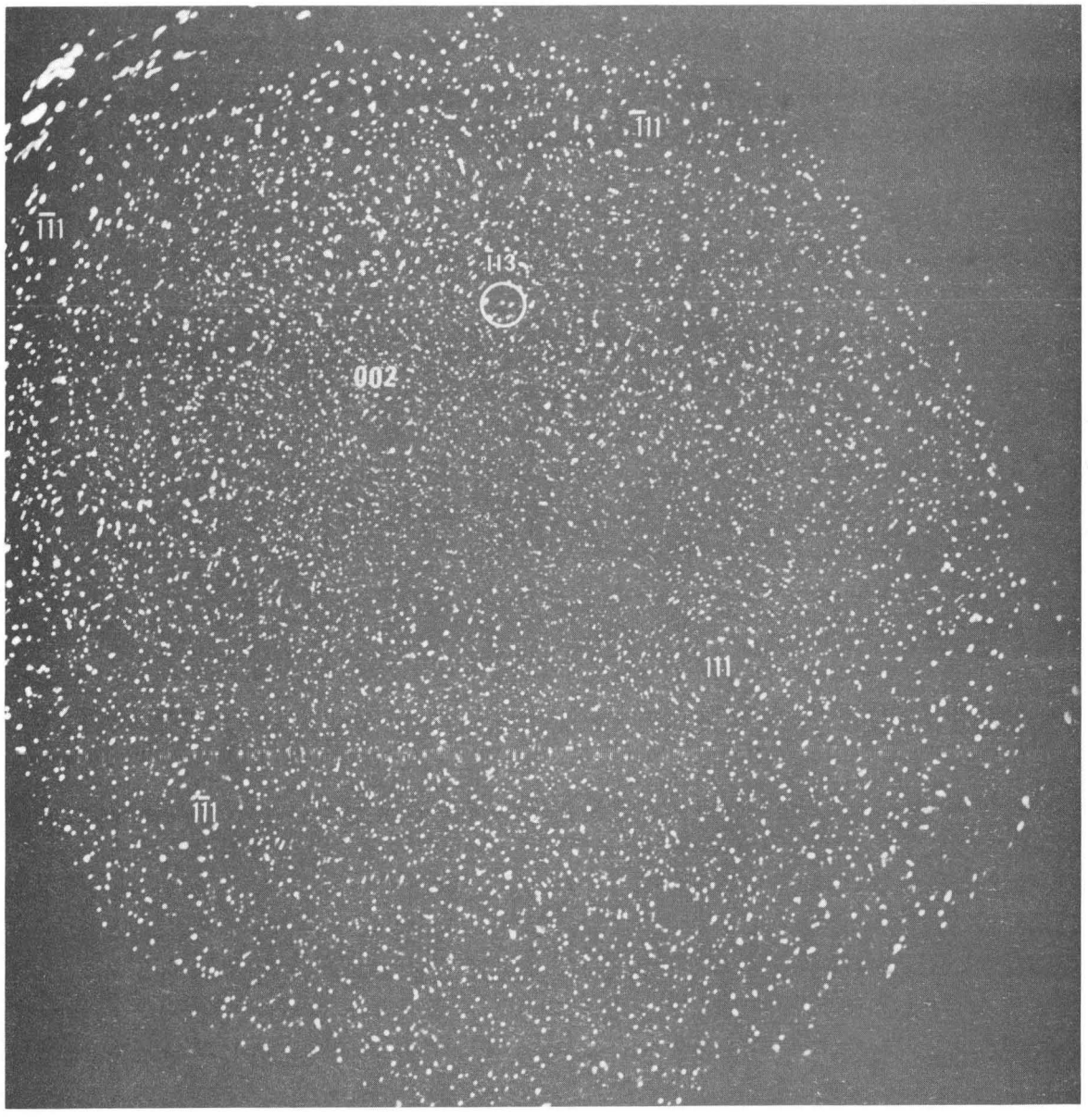

XBB 6911-7501

Figure 20b

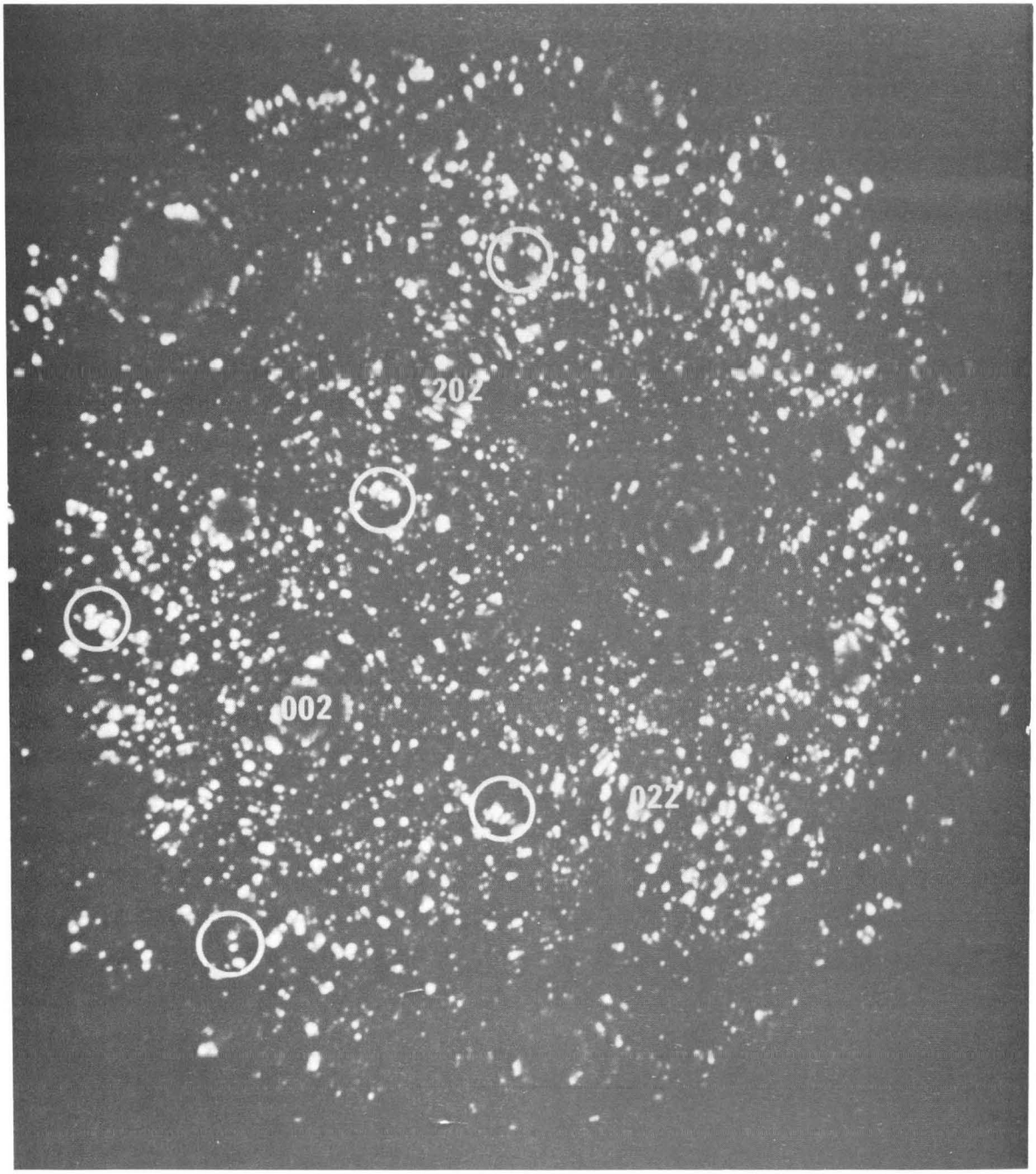

XBB 6911-7499

Figure 20c

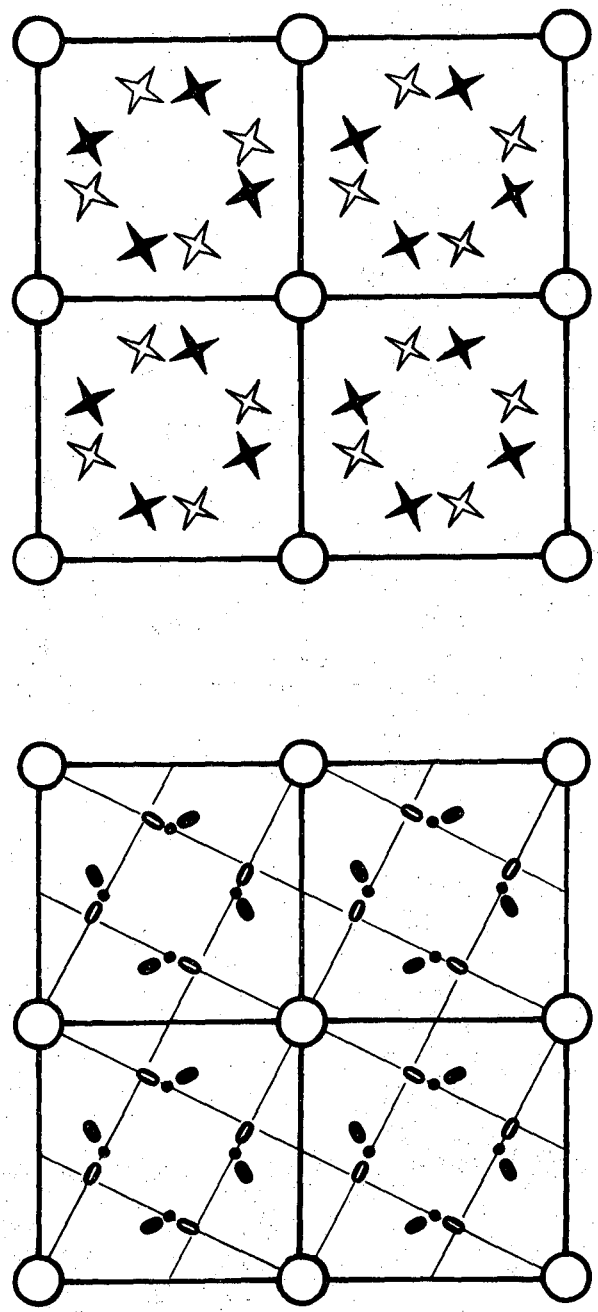

XBL 6911-6600

Figure 21a and b

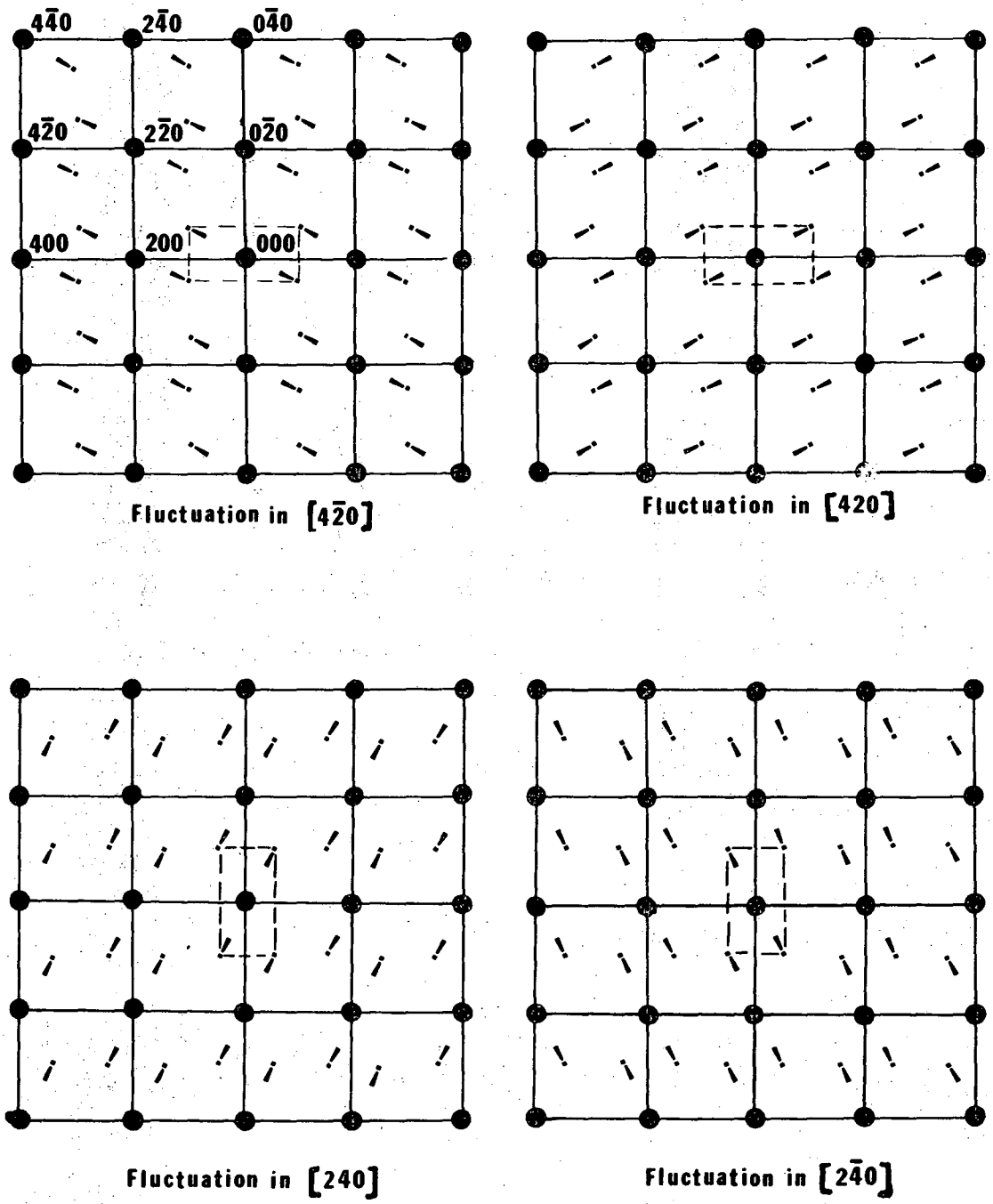

XBL 6911-6599

Figure 21c

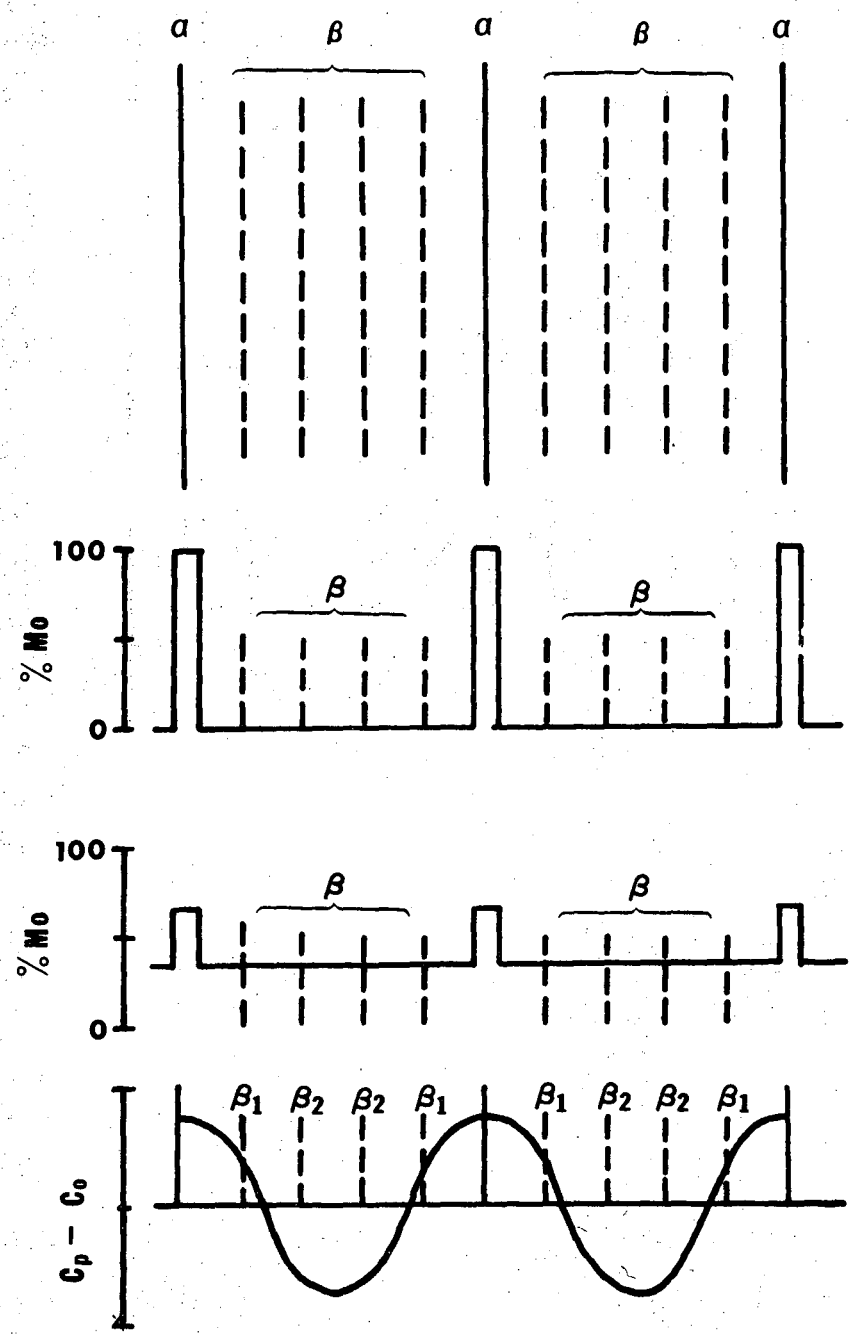

XBL 6911-6597

Figure 22a and 22b

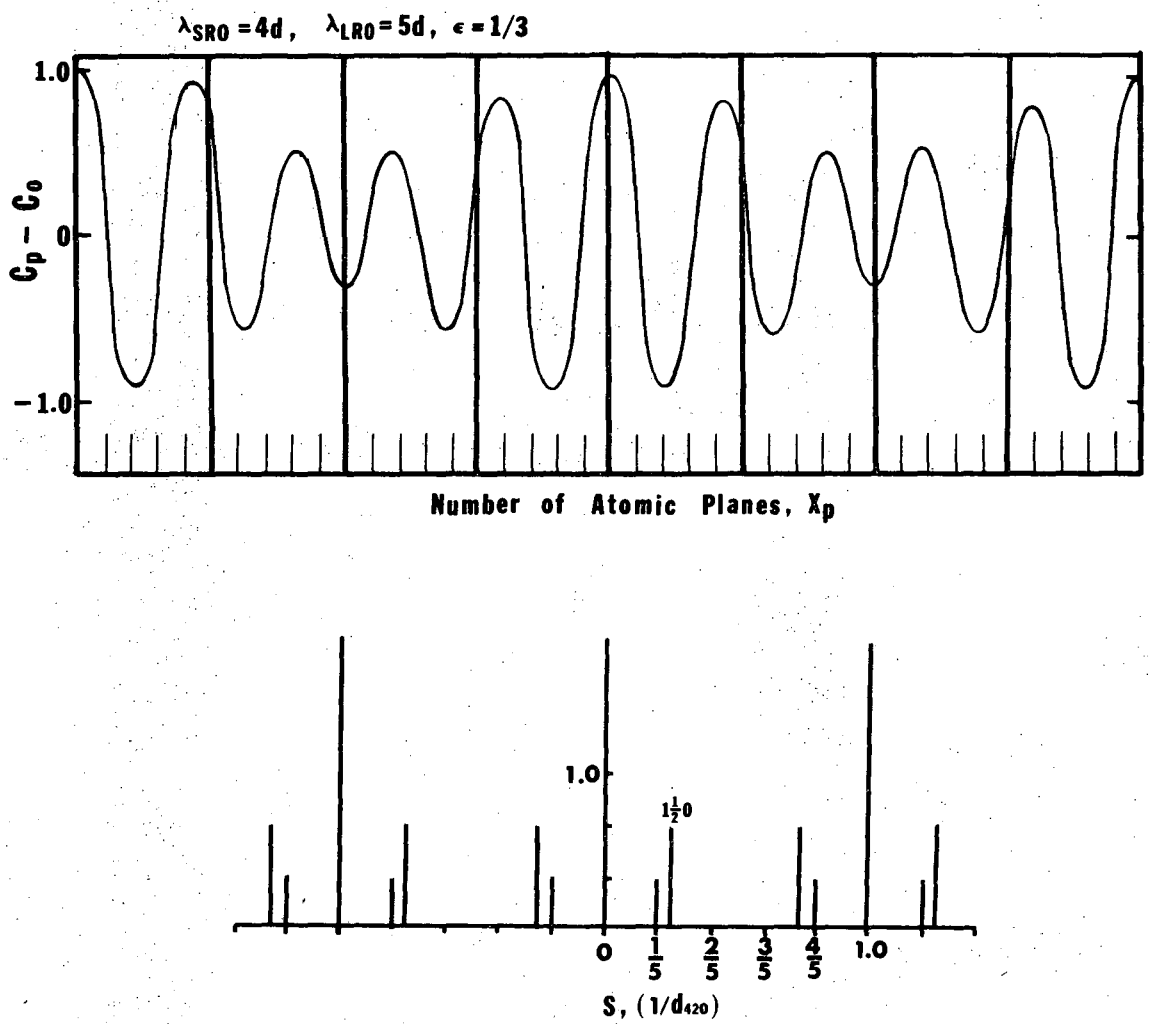

XBL 6911-6596

Figure 24a

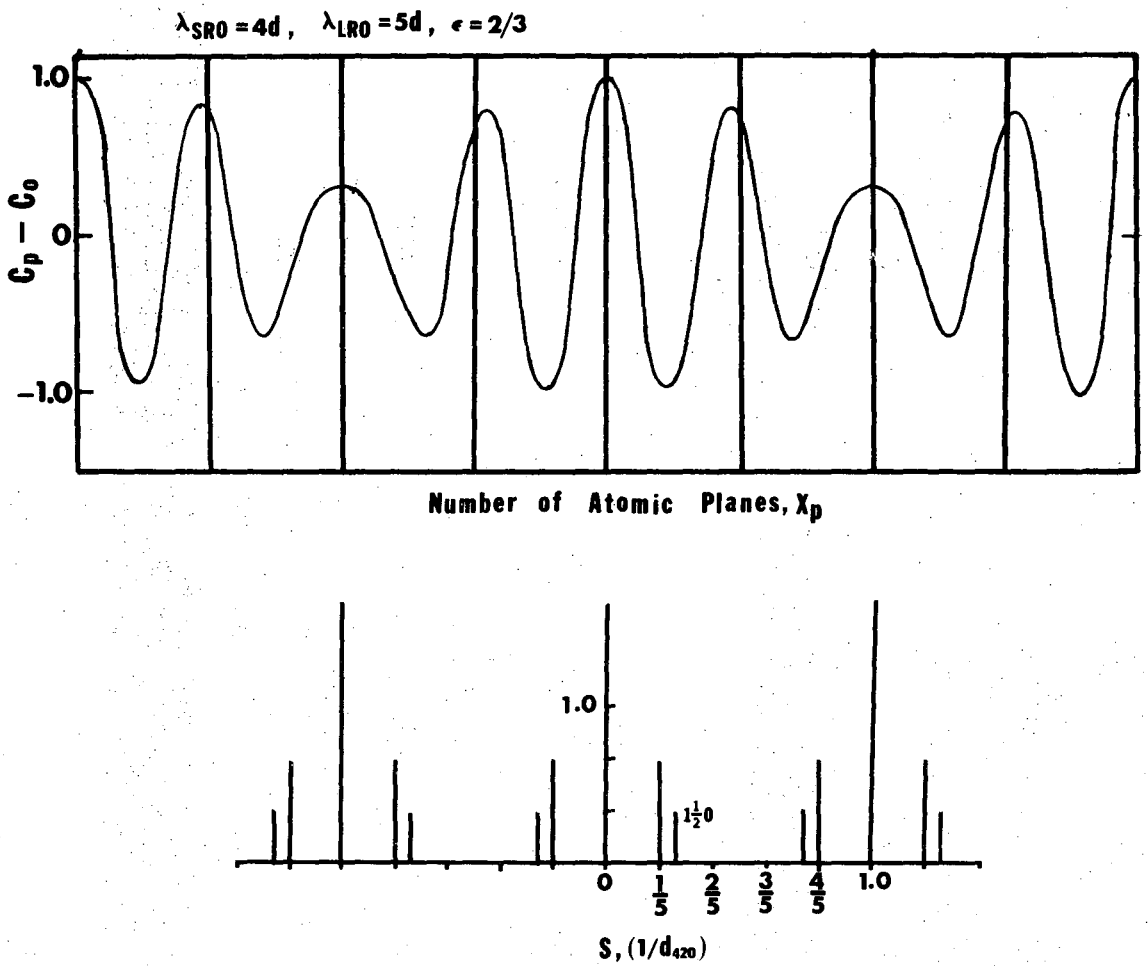

XBL 6911-6595

Figure 24b

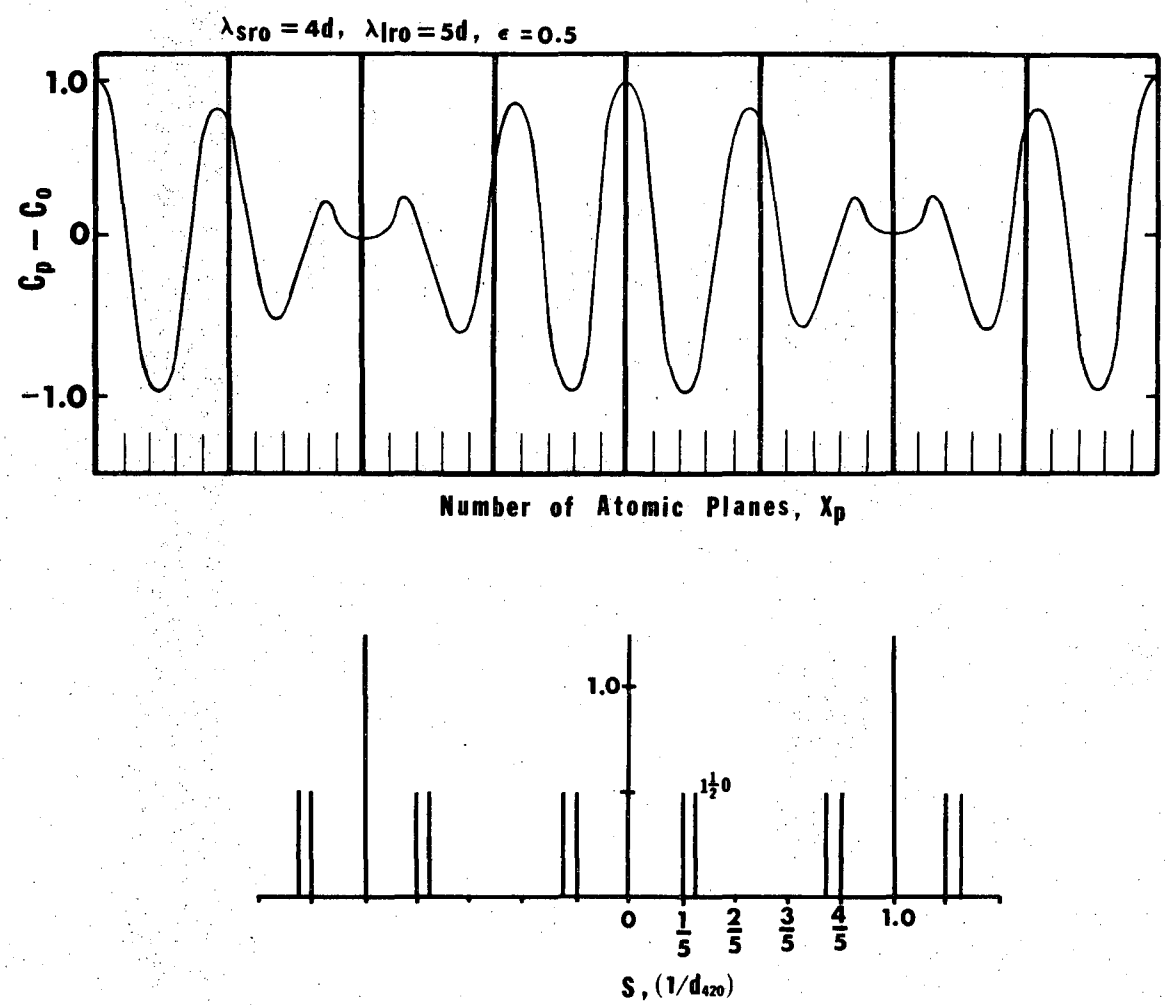

XBL 6911-6593

Figure 24c

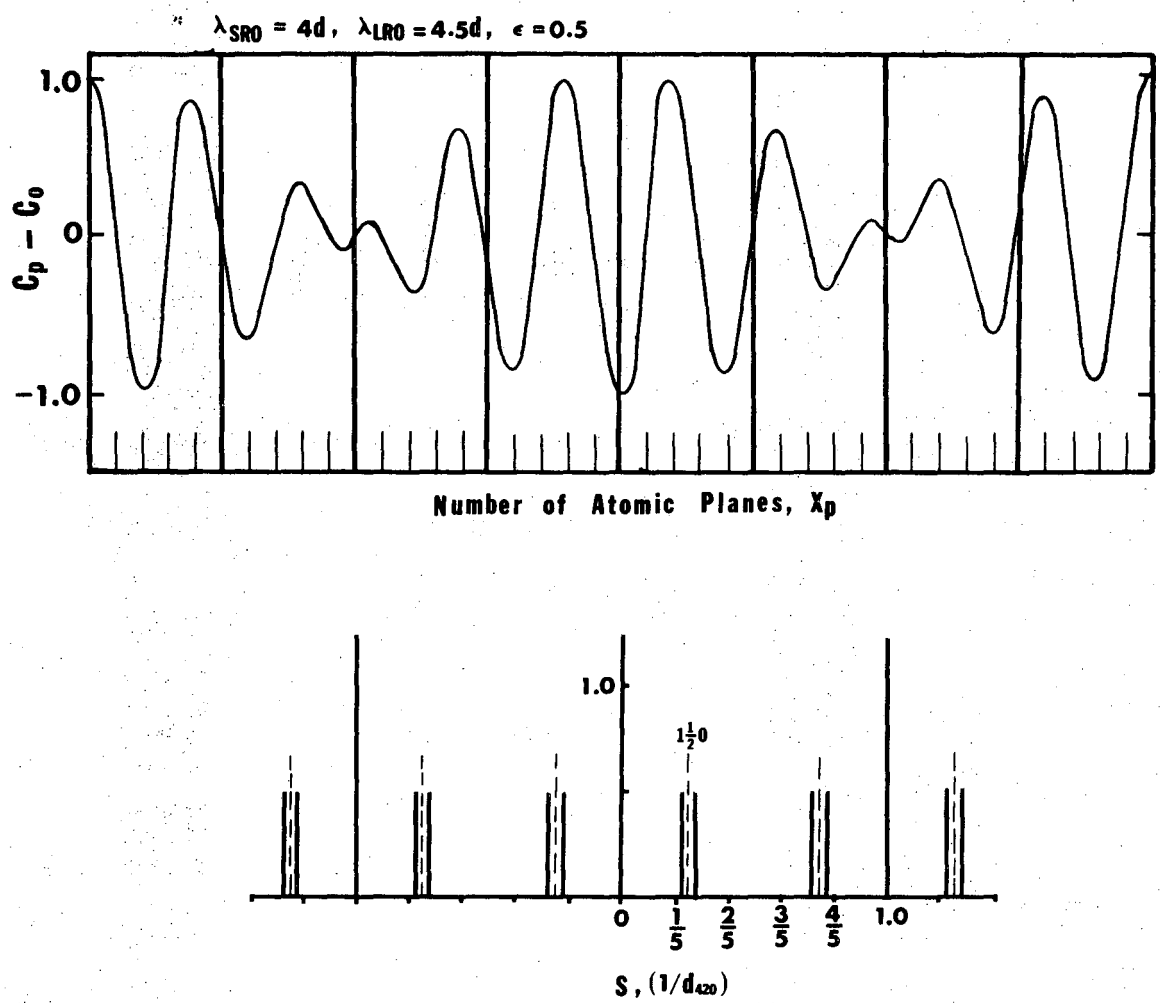

XBL 6911-6594

Figure 25a

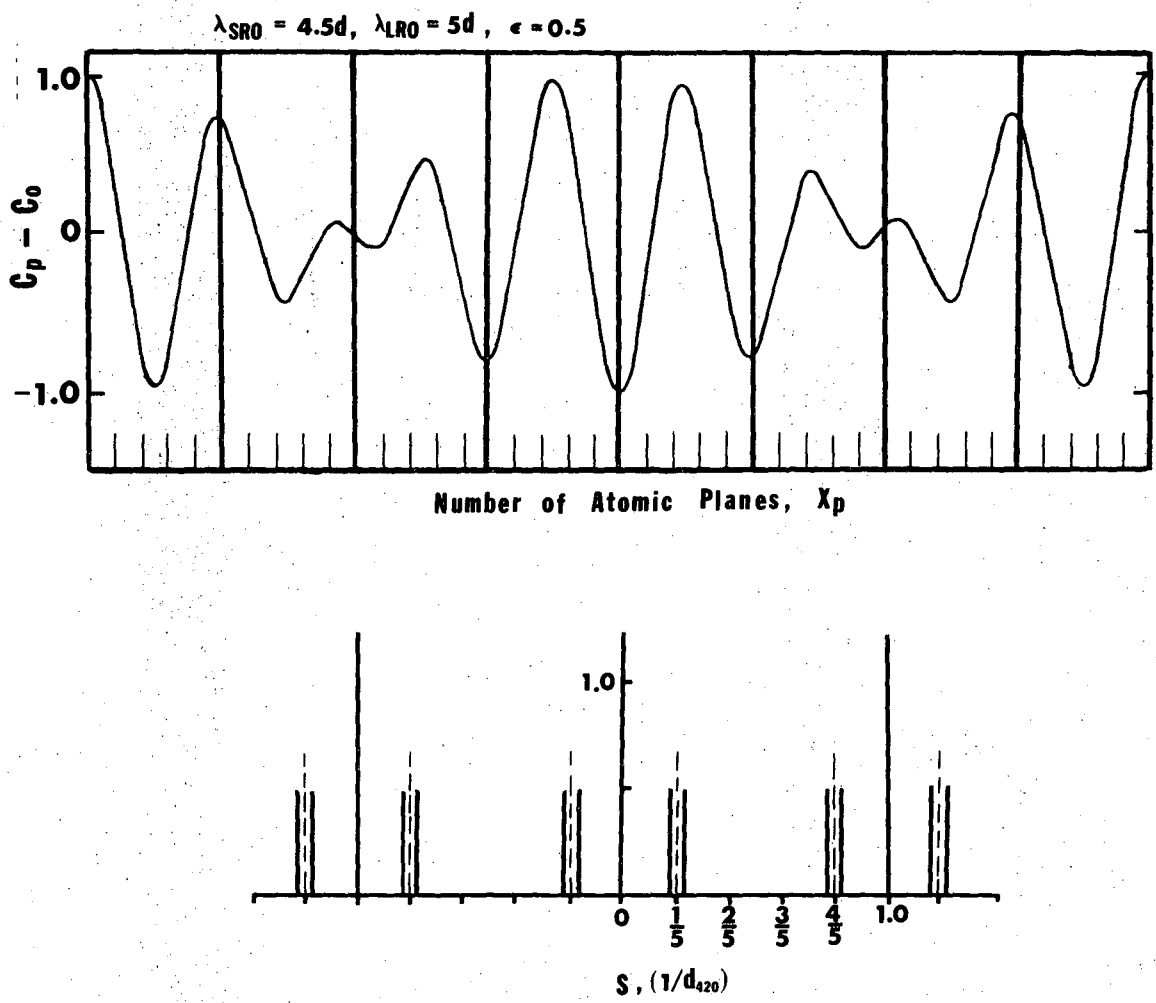

XBL 6911-6598

Figure 25b

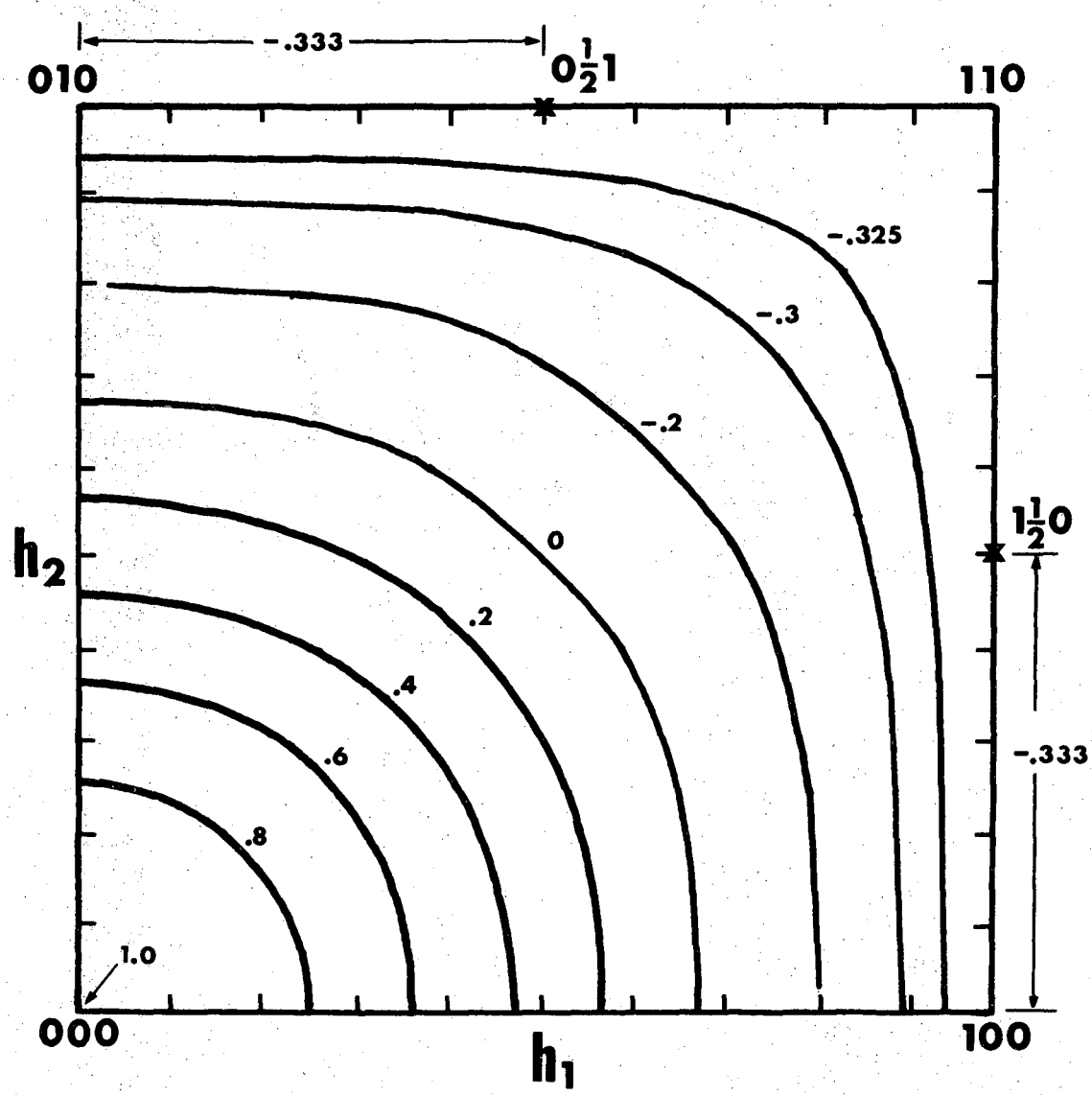

XBL 6911-6592

Figure 26

LEGAL NOTICE

This report was prepared as an account of Government sponsored work. Neither the United States, nor the Commission, nor any person acting on behalf of the Commission:

A. Makes any warranty or representation, expressed or implied, with respect to the accuracy, completeness, or usefulness of the information contained in this report, or that the use of any information, apparatus, method, or process disclosed in this report may not infringe privately owned rights; or

B. Assumes any liabilities with respect to the use of, or for damages resulting from the use of any information, apparatus, method, or process disclosed in this report.

As used in the above, "person acting on behalf of the Commission" includes any employee or contractor of the Commission, or employee of such contractor, to the extent that such employee or contractor of the Commission, or employee of such contractor prepares, disseminates, or provides access to, any information pursuant to his employment or contract with the Commission, or his employment with such contractor.

TECHNICAL INFORMATION DIVISION
LAWRENCE RADIATION LABORATORY
UNIVERSITY OF CALIFORNIA
BERKELEY, CALIFORNIA 94720